POSSIBLE GLOBAL SURFACE WARMING "HIATUS"

AND REGIONAL CLIMATE RESPONSE:

FROM A PERSPECTIVE OF OCEAN HEAT CONTENT

by

Xiangbai Wu

A dissertation submitted to the Faculty of the University of Delaware in partial fulfillment of the requirements for the degree of Doctor of Philosophy in Oceanography

Fall 2015

ProQuest Number: 10014770

ProQuest 10014770
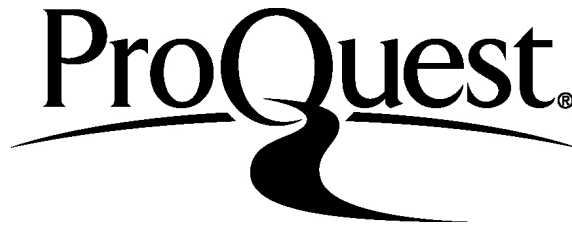
POSSIBLE GLOBAL SURFACE WARMING "HIATUS"

AND REGIONAL CLIMATE RESPONSE:

FROM A PERSPECTIVE OF OCEAN HEAT CONTENT

by

Xiangbai Wu

Approved: _____
Mark Moline, Ph.D.
Director of the School of Marine Science and Policy

Approved: _____
Mohsen Badiey, Ph.D.
Acting Dean of the College of Earth, Ocean and Environment

Approved: _____
Ann L. Ardis, Ph.D.
Interim Vice Provost for Graduate and Professional Education

I certify that I have read this dissertation and that in my opinion it meets the academic and professional standard required by the University as a dissertation for the degree of Doctor of Philosophy.

Signed: _____

Xiao-Hai Yan, Ph.D.
Professor in charge of dissertation

I certify that I have read this dissertation and that in my opinion it meets the academic and professional standard required by the University as a dissertation for the degree of Doctor of Philosophy.

Signed: _____

Yan Li, B.Sc.
Member of dissertation committee

I certify that I have read this dissertation and that in my opinion it meets the academic and professional standard required by the University as a dissertation for the degree of Doctor of Philosophy.

Signed: _____

Yuwu Jiang, Ph.D.
Member of dissertation committee

I certify that I have read this dissertation and that in my opinion it meets the academic and professional standard required by the University as a dissertation for the degree of Doctor of Philosophy.

Signed: _____

Young-Heon Jo, Ph.D.
Member of dissertation committee

ACKNOWLEDGMENTS

I dedicate my dissertation work to my family and friends, who have supported me throughout the process. I will always appreciate all they have done for me.

TABLE OF CONTENTS

LIST OF TABLES

LIST OF FIGURES

ABSTRACT

The emission of greenhouse gases (GHGs) from human economy and social activity, such as burning of fossil fuel, cement industry, deforestation and so on, contribute to continuously increasing of GHGs, CO_2 for example. The increased GHGs concentration leads to the energy imbalance at the top of atmosphere and heat cumulating within the earth climate system. Understanding the ocean's role in Earth's energy budget is fundamental to evaluate climate variability and change, including the rate of global warming and the recent 18-years' so-called Global Surface Warming Hiatus (GSWH). Progress has been made continuously on this topic: studies show that the GSWH is related to external forcing changes, internal variability induced by trade wind and wind-driven circulation adjustment with the resulting heat redistribution within the climate system, and the warming up in subsurface and deeper ocean. There are a wide range of opinions among climate scientists and no unanimous conclusion has been drawn about the mechanism of the global warming hiatus. In this dissertation, the spatio-temporal variations of the Ocean Heat Content (OHC) were investigated to reveal the physical mechanisms of the global warming hiatus and the regional climate response in East Asia.

Firstly, methods were developed to estimate temperature anomaly for subsurface and deeper layer from sea surface parameters provided by remote sensing, to generate new data sets for decadal climate variability research. A Self-Organizing Map Neural Network (SOM) was developed from Argo gridded data sets in order to estimate subsurface temperature anomaly (STA) from remote sensing data. The SOM

maps were trained using anomalies of sea surface temperature (SST), height (SSH) and salinity(SSS) data from Argo gridded monthly anomaly data sets, labeled with Argo STA data for 2005~2010 and then used to estimate the STAs at different depths in the North Atlantic from the sea surface data. The estimated STA maps and time series were compared with Argo STAs including independent data sets for validation. In the Gulf Stream Path areas, the STA estimations from the SOM algorithm show good agreement with in situ measurements taken from the surface down to 700m depth, with a correlation coefficient lager than 0.8. Sensitivity of the SOM, when including salinity shows that with SSS anomaly data in the SOM training process, reveal the importance of SSS information, which can improve the estimation of STA in the subtropical ocean by up to 30%. In subpolar basins, the monthly climatology SST and SSH can also help to improve the estimation by as much as 40%. STA time series for 1993~2004 in the mid-latitude North Atlantic were estimated from remote sensing SST and altimetry time series using the SOM algorithm. Limitations for the SOM algorithm and possible error sources in the estimation are briefly discussed.

Secondly, OHC spatio-temporal variations were analyzed using the empirical orthogonal function analysis. A meridional dipole has dominated the variation of the ocean heat content in the upper layer, and the warming in the upper layer of the Indian Ocean has been in "hiatus" since early 1980s. Further, a very new and sophisticated causal analysis method revealed that the warming in the southern subtropical Indian Ocean contributed to the pre-conditioning and warming in the southern and tropical Atlantic since 1980s and to the heat sequestration at the deeper layer in the Southern Ocean during the global surface warming hiatus period. In addition, zonal ocean heat content anomaly were found to shift westwards in a way that resembles Rossby wave,

with a period of about 30 years, and phase speed of 1.8-2.5 cm/s. It takes about 60 years for the anomaly signal to travel from east Pacific to the Western Atlantic via the Indian Ocean. The redistribution of OHC in upper layer follows the surface branch of the Global Ocean Conveyor belt to travel westward from Pacific to the Atlantic via Indian Ocean. With an embedded atmospheric bridge linking the Atlantic SST with the Pacific trade winds, the global ocean and atmosphere forms a closed loop. This finding explains not only the occurrence of global warming hiatus, but also sheds light on the multi-decadal climate variability.

Thirdly, the decadal variation of vertical OHC distribution and its impact on air-sea interaction in Western North Pacific were studied to reveal regional climate respond to global warming hiatus. The decadal variation of rapid intensification of Tropical Cyclones (TCs) in Western Northern Pacific were studied using TC best track datasets. The intensity and frequencies of intense TC peaked in 1960s, and have not increased in a global warming climate. Compared to previous tropical cyclone (TC) studies that focus on the frequency of rapid intensification (RI), a new index (RITC) is proposed to measure the RI-level for category 4-5 TCs (Saffir–Simpson scale) in the western North Pacific. RITC is the maximum increase in the sustained-wind-speed per 24-hour during the lifetime of a TC. The results show that the PDO modulation of the interannual ENSO-RI relationship is better represented with the new RITC than with the RI number. The interannual relationship between ENSO and RITC is strong and statistical significant in warm PDO while not significant in cold PDO, mainly attributed to the variation of zonal wind speed. On decadal time scales, the PDO's modulations of ENSO's effects on RITC are mainly attributed to the variations of

upper ocean heat content and vertical wind shear. Our results have significant implications for the prediction of RI and long-term projections of major TC activity.

In summary, OHC was used as tracer to study the decadal heat redistribution, horizontal and vertical, in Indian Ocean, Atlantic and Southern Ocean. Indian Ocean was found to be the accelerator for the global surface warming hiatus through supplying heat to the southern Atlantic Ocean. The redistribution of OHC in upper layer explains not only the global warming hiatus, but also the multi-decadal climate variability. The decadal variation in rapid intensification of intense TCs provides a better understanding of the decadal variation of the TC in Western North Pacific and a new perspective for the regional climate responding to the decadal variability of OHC under the changing climate.

Chapter 1

INTRODUCTION

1.1 Background and Motivation

The human economy and social activity, such as burning of fossil fuel, cement industry, deforestation and so on, contribute to continuously increasing of greenhouse gases (GHGs), CO2 for example. The annual mean atmospheric concentration of CO2 at Mauna Loa, Hawaii, increased from about 315ppm in 1960's to 396ppm in 2013 (Fig 1.1, Keeling et al., 2001; IPCC, 2013). The greenhouse effect from these gases trapped more energy in the climate system, leading to global warming. Greenhouse gases contributed a global mean surface warming likely to be in the range of 0.5°C to 1.3°C over the period 1951 to 2010. The global surface warming hiatus since 1998 raises global societal interests and challenged the climate science community and the international policies regarding climate change. Ocean warming dominates the increase in energy stored in the climate system, accounting for more than 90% of the energy accumulated between 1971 and 2010 (Table 1; IPCC, 2013). Study of spatio-temporal variability of the Ocean Heat Content (OHC, see section 1.2 for detailed definition and dynamic frameworks) will improve our understanding of the processes and mechanisms ocean response to the changing climate and the role ocean played in the climate system. In this study, OHC was used as a tracer to study the decadal heat redistribution, horizontal and vertical in global oceans, to reveal the physical mechanisms of the global warming hiatus and the regional climate response in East Asia.
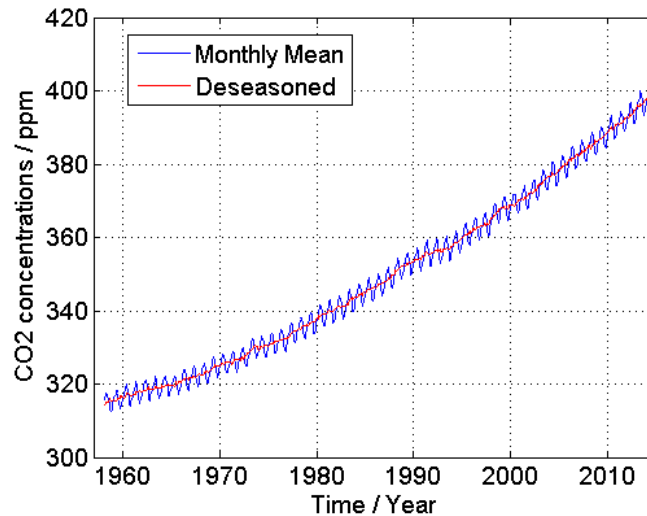
Fig. 1.1 Atmospheric CO2 concentrations (ppm) derived from in situ air measurements monthly Mauna Loa CO2 concentrations in micro-mol CO2 per at Mauna Loa, Observatory, Hawaii: Latitude 19.5° N Longitude 155.6° W Elevation 3397m, since 1958 (Keeling et al., 2001).

1.1.1 Global warming hiatus and the internal decadal variability of climate system

The warming rate of global surface temperature has stalled 0.05 degree/decade since 1998, compared to 0.12 degree/decade, since 1951 (Meehl et al., 2011; Kosaka and Xie, 2013). This is so called global warming hiatus (Fig 1.2). Why the global warming rate has been reduced for nearly 15 years when there is increasing GHGs? The mechanisms for this hiatus are not well understood yet. From the external forcing of earth climate system, solar activity decreases, volcano activity increases, water vapor increases in stratosphere (Solomon et al., 2010) and rapidly increase of aerosols concentration in stratosphere and troposphere (Solomon et al., 2010; Kaufmann, et al., 2011) are possible reasons for generating hiatus. On the other hand, the internal variability of the climate system is believed to play an important role in the climate

hiatus (Meehl et al., 2011; Kosaka and Xie, 2013；Trenberth and Fasullo, 2013; Balmaseda2013; England et al., 2014).

For the internal variability, Wu et al. (2007) showed that the rapidity of the warming in the late twentieth century was a result of concurrence of a secular warming trend and the warming phase of a multidecadal (~65-year period) oscillatory variation (Fig 1.2). Up to one third of the late twentieth century warming could have been a consequence of natural variability, which is possibly linked to low frequency variations in the strength of the thermohaline circulation (Wu et al., 2011). In the recent decade, the variation of the surface temperature in the Pacific was in a cooling Pacific Decadal Oscillation (PDO) phase. In the 20th century, another hiatus for global warming occurred in cooling phase PDO (Trenberth & Fasullo, 2013).

The recent warming trend in the Atlantic Ocean sea surface temperature since the early 1990s and corresponding trans-basin displacement of the main atmosphere pressure centers were proposed to be the key drivers of the observed Walker circulation intensification (McGregor et al., 2014). The strengthening of the Pacific trade winds since the late 1990s caused the development of the cold tongue in the eastern Tropical Pacific, the sea level rise in western Pacific, and the subsurface warming by intensified shallow wind-driven circulation (England et al., 2014). The decadal cooling in Eastern Pacific has been identified as one of the contributors to the current hiatus in global surface warming (Kosaka & Xie, 2013). The enhanced tropical Indian Ocean warming in recent decades is reported to favor stronger trade wind in the western Pacific via the atmosphere and have contributed to the eastern Pacific cooling (with enhanced east-west Walker circulation) through the Pacific ocean-atmosphere interaction (Luo et al., 2012). These findings suggest that the global surface warming

has been partly offset by the Pacific climate response to enhanced warming in the Atlantic (McGregor et al., 2014) and Indian Oceans (Luo et al., 2012).
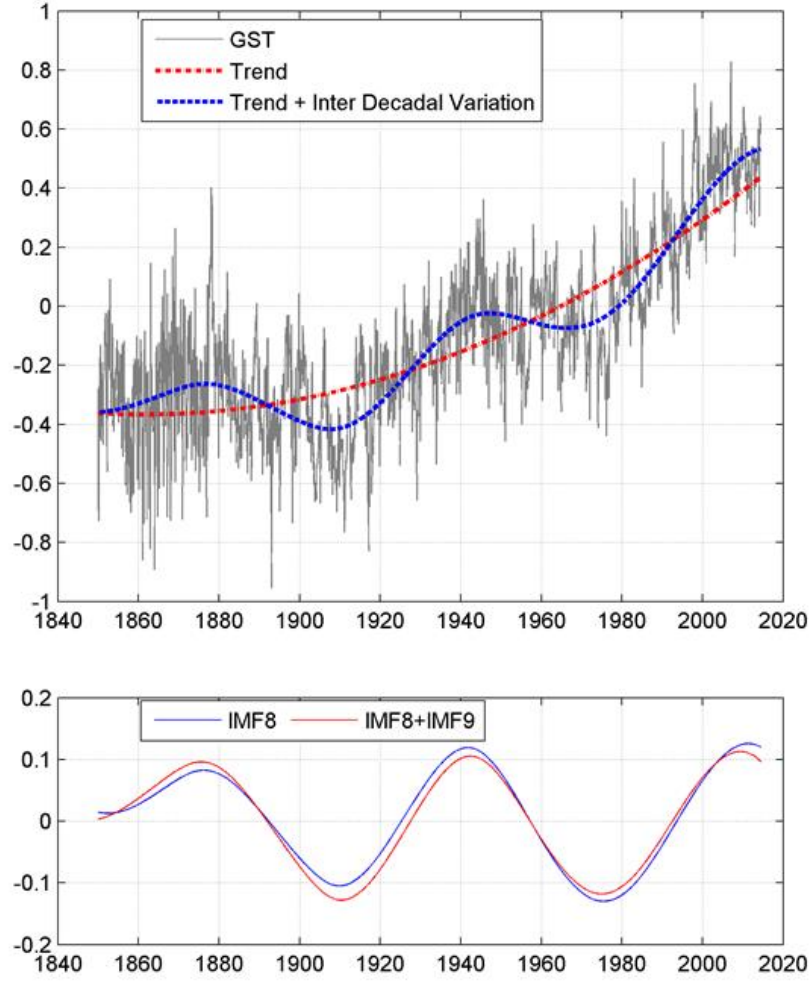
Fig. 1.2 Time series of HadCRUT4 global surface temperature (GST) and decadal variation. (a) GST time series (gray), EEMD decomposed residual trend (red) and residual trend plus multi-decadal variation (blue). (b) Intrinsic mode functions No.8 and No.9 from EEMD analysis (After Wu et al, 2007, 2011).

1.1.2 Upper and deep ocean warming during global warming hiatus period

During the global warming period, over 90% of the trapped heat by GHGs was absorbed by the ocean (Table 1.1; Bindoff et al., 2007; Church et al., 2011; IPCC, 2013), which make the temperature of water column of upper ocean increase and thermal expansion (Domingues et al., 2008; Ishii and Kimoto, 2009; Lyman et al., 2010; Levitus et al., 2009, 2012; Sloyan et al., 2013), hence lead to the uprising of the global sea level(Antonov et al., 2005; Domingues et al., 2008; Church et al., 2011; Hanna et al., 2013; Held, 2013). During the hiatus period, the deeper ocean is found to have more heat than non-hiatus period, about 30-35% of the heat absorbed by the ocean goes to the deep ocean (Palmer et al., 2011; Meehl et al., 2011; Trenberth & Fasullo, 2011; Katsman & van Oldenborgh, 2011；von Schuckmann & LeTraon, 2011; Levitus et al., 2012；Balmaseda et al., 2013；Abraham et al., 2013; Bala, 2013; Guemas et al., 2013; Watanabe, 2013; Wake, 2013; Schultz, 2013; IPCC, 2013), and although there are many other approaches to explain the hiatus, the deep ocean is generally believed to play a very important role. The contribution to the sea level rising from the deep ocean is about 1/3 of the total rise trend (Song and Colberg, 2011). Model based analysis reveals that the warming trend in mid- to deep-ocean (>700 meter) is much more significant than the upper ocean (Meehl et al., 2011) during hiatus period, these indicate that there are vertically redistribution of heat variation. The warming up of deep-ocean brings a big challenge to investigate for the science community since the in-situ data is very limited with poor resolution.

The inter-annual to decadal variation of ocean included ENSO, PDO, NAO and AMO, etc. (Chylek et al., 2013) as internal variations supported to the global warming trend which are dominantly affect to the global ocean mass and heat storage redistribution, and those may have contributed to the global warming hiatus

(Trenberth and Fasullo, 2013). In the horizontal direction, the redistribution of water mass between continents and oceans in the 2011 La Nina event induced a decrease of 5mm in the global mean sea level (Boening et al., 2012). On the vertical direction Argo system documented a redistribution of ocean heat content from surface layer (0-100m) to subsurface layer (100-500m) 2 years before 2009 El Nino, the ocean loses heat during positive anomaly SST and gains heat from atmosphere during negative SST anomaly (Roemmich and Gilson, 2011).

It is still not clear that whether there is any vertical heat distribution related to PDO and other internal variability or not, and how it is related to the hiatus? This issue will be addressed by analysis of the ocean heat content, isothermal surface and isopycnal surface variations in the West Tropical Pacific and Northwest Pacific.

Table 1.1 Distribution of global energy change inventory due to greenhouse gases between 1971 and 2010 (IPCC, 2013)

Distribution	Percentage (%)
Warming of ocean	93
Upper layer (0-700m)	64
Deep layer (700-2000m)	about 30
Ice melting	3
Continent warming	3
Atmosphere warming	1

1.1.3 Regional climate response to global warming hiatus

The Pacific plays an important role in global warming hiatus (Kosaka & Xie, 2013, England et al, 2014), the frequent occurrence of the La Nina and intensified east trade wind helps the development of the cold tongue in the east Tropical Pacific. The hiatus is found to be related to the negative phase of PDO (Trenberth & Fasullo, 2013). On the other hand, the warming of the deep ocean is believed to be one of the mechanisms for the decadal internal variation. During the hiatus period, the heat up-take of the subsurface and deep ocean is much more significant than other decades (Meehl et al, 2011). The wind driven meridional overturning circulation between the tropical and subtropical oceans slowed down from 1970's to 1990's, causing a decrease of 25% of the upwelling the equatorial ocean and hence a rise in the equatorial sea surface temperature (McPhaden and Zhang, 2002). However from 1990's to the beginning of 2010's, the increased subsurface ocean heat uptake, which was induced by the increased subduction of the shallow overturning cell, slowdowns the warming of the surface layer in tropical Pacific (England et al, 2014).

The redistribution of the heat in the ocean between the surface and subsurface layers has an ENSO like temporal pattern, the changes in the east-west tilting of the equatorial Pacific thermocline is the major reason (Roemmich and Gilson, 2011). In 1990's the surface warming of tropical Indian ocean and Pacific accompanied a strong cooling in the upper thermocline, while during the hiatus period, the surface cooling of east equatorial pacific ocean accompanied by the increased subsurface ocean heat uptake (Han et al, 2006; Trenary and Han, 2008; England et al, 2014).

1.1.4 Decadal climate variation and deep ocean research need more data from observation

The research of decadal and inter-decadal ocean variability and climate change is a comprehensive scientific topic (Le Treut et al., 2007; Liu, 1999, Solomon et al., 2011), which involve mutlti-temporal and spatial scales, from sub-mesoscale to planetary scale, from seasonal to inter-decadal, through observation and other research tools from many physical parameters. However, due to the limitation of technology and other objective reasons like funding, the data sets obtained from observation have a large percentage of sparsely area and discontinuity of the time series, especially for studying of mid to deep ocean phenomena and processes.

The internal variability from subsurface to deeper ocean have been confirmed as a source of predictability in climate models, such as AMOC variation (Delworth and Mann, 2000; Knight et al., 2005; Zhang and Delworth, 2006; Yang et al., 2013). The initial condition of subsurface to deeper ocean state is the key for strengthen the predictability of the coupled ocean and climate models (Smith et al., 2007; Keenlyside et al., 2008).

Since the 1970s, remote sensing has provided a huge amount of high spatial and temporal resolution, large overall coverage, and long time series of sea surface data, which explored unprecedented progress and notable discoveries in atmosphere, ocean and climate sciences. While remote sensing is the most cost-efficient tool, the observations are confined to the sea surface phenomena. Therefore, our knowledge of the sea surface greatly exceeds what we know at below surface. However, subsurface data is critical to understand about their mechanisms and processes in the ocean as a whole, as well as for entirely earth climate system (e.g. Meehl et al., 2011). Large subsurface in-situ measurement projects has been implemented recently such as

Integrated Ocean Observing System (IOOS) and Global Ocean Observing System (GOOS) with over 8000 platforms including drift buoys, moored buoys, Argo floats, gliders and Expendable Bathythermographs (XBTs), the subsurface observations available are still too scarce in most parts of the ocean.

Argo is a global array of more than 3,000 free-drifting profiling floats that measures the temperature and salinity of the upper 2000 m of the ocean (Fig 1.3). This allows, for the first time, continuous monitoring of the temperature, salinity, and velocity of the upper ocean, with all data being relayed and made publicly available within hours after collection. This system got started in1999 and has achieved 3000 floats since November 2007. In November 2012, a float in the Argo array gathered the one-millionth profile (twice the number collected by research vessels during all of the 20th century). The Argo data became very important in large scale analysis in the ocean. However, the time scale of available Argo data is 15 years, still inadequate for decadal climate and ocean variation study. Argo profiles provide subsurface information that is necessary to establish the link between surface and subsurface, making the extension of remote subsurface data back to pre-Argo era possible and available for decadal analysis.
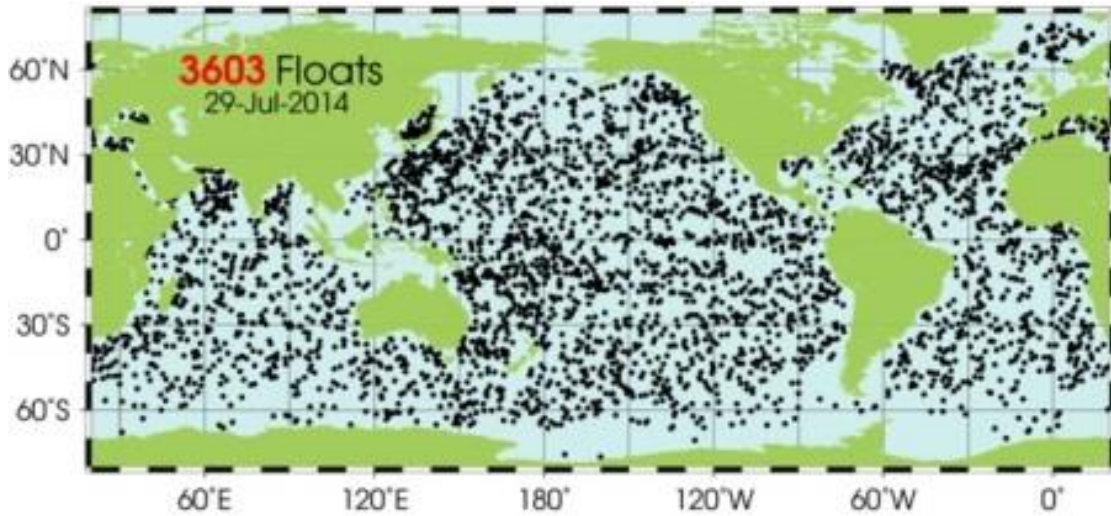
Fig. 1.3 Positions of the floats that have delivered data within 30 days, July 2014 (download from: http://www.argo.ucsd.edu/index.html)

1.2   Ocean Heat Content Dynamics in the Upper Ocean

The ocean heat content (OHC) is also known as ocean heat content anomaly, as defined by Yan et al. (1995), Chamber et al. (1997) and Levitus et al. (2000, 2012), computed with a reference mean subtracted out from each temperature observation. Long term monthly climatology is often used as reference mean temperature in the calculation of OHC, to study the variation of the time scale of inter-annual to multi-decadal. For per unit area in the ocean, we have

$$T' = T - \bar{T} \tag{1.1}$$

$$H = \int_{h1}^{h2} C_v \rho \left(T - \bar{T} \right) dz \tag{1.2}$$

where H is ocean heat content, T' is temperature anomaly, C_v is the heat capacity, T is temperature, $\bar{T}$ is the monthly climatology of temperature, h_1 and h_2.is the upper and lower limits of the layer for OHC calculation.

A brief review of physical mechanism that controls the variation of temperature and temperature anomaly will help us understand the variation of ocean heat content. The equation governing temperature is derived from conservation of energy. The first law of thermodynamics, also known as the principle of energy conservation, states that the internal energy gained by a parcel of sea water is equal to the heat Q it receives minus the mechanical work W it performs. For unit mass, we have

$$\frac{de}{dt} = Q - W \tag{1.3}$$

Where $\frac{d}{dt}$ is the material derivative; e is the internal energy, defined as $e = C_v T$; Q the rate of heat gain, defined as $Q = \frac{k_T}{\rho} \nabla^2 T$, k_T is the thermal conductivity of the fluid, ρ is the density; and W the rate of work done to the surrounding fluid, defined as $W = p \frac{d\sigma}{dt}$, p is pressure and σ is the volume per unit mass, defined as $\sigma = \frac{1}{\rho}$.

$$C_v \frac{dT}{dt} = \frac{k_T}{\rho} \nabla^2 T - p \frac{d\sigma}{dt} = \frac{k_T}{\rho} \nabla^2 T + \frac{p}{\rho^2} \frac{d\rho}{dt} \tag{1.4}$$

According to the continuity equation,

$$\frac{\partial \rho}{\partial t} + \frac{\partial}{\partial x}(\rho u) + \frac{\partial}{\partial y}(\rho v) + \frac{\partial}{\partial z}(\rho w) = 0 \tag{1.5}$$

and the material derivative of density and temperature,

$$\frac{d\rho}{dt} = \frac{\partial \rho}{\partial t} + u\frac{\partial \rho}{\partial x} + v\frac{\partial \rho}{\partial y} + w\frac{\partial \rho}{\partial z} \tag{1.6}$$

$$\frac{dT}{dt} = \frac{\partial T}{\partial t} + u\frac{\partial T}{\partial x} + v\frac{\partial T}{\partial y} + w\frac{\partial T}{\partial z} \tag{1.7}$$

and with Bossinesq approximation, Equation (1.4) becomes the advection-diffusion equation for temperature of sea water:

$$\frac{\partial T}{\partial t} + \frac{\partial}{\partial x}(uT) + \frac{\partial}{\partial y}(vT) + \frac{\partial}{\partial z}(wT) = \kappa_T \nabla^2 T \tag{1.8}$$

where $\kappa_T = \dfrac{k_T}{\rho C_v}$ is the heat kinematic diffusivity. The local time rate of temperature change is the result from local heating and advection transport.

At the sea surface, z=0，we have T= SST, and

$$\left(\kappa_T \frac{\partial T}{\partial z}\right)_{z=0} = \frac{1}{\rho C_v} Q_\downarrow \tag{1.9}$$

where $Q_\downarrow$ is the heat flux across the ocean-atmosphere interface (positive for downward flux),

$$Q_\downarrow = Q_{SW} + Q_{LW} + Q_L + Q_S \tag{1.10}$$

where Q_{SW} is the incoming solar shortwave irradiance, Q_{LW} is the net longwave radiation, Q_L is the latent heat flux and Q_S is the sensible heat flux.

1.2.1 Heat budget model for a fixed depth layer

Vertical movements of layer interfaces played an important role in the upper-ocean heat budget (Emery, 1976), for a layer of fixed depth of *D*，*neglecting diffusion and flux at the lower boundary,* the heat content budget equation becomes

$$\frac{\partial}{\partial t}\int_{-D}^{0} Tdz + \int_{-D}^{0} \nabla \cdot \vec{V}Tdz = \frac{Q_\downarrow}{\rho C_p} \tag{1.11}$$

where $\vec{V}$ is the three dimensional velocity.

$$\frac{\partial}{\partial t}\int_{-D}^{0}Tdz+\int_{-D}^{0}\nabla\cdot\vec{v}Tdz+\int_{-D}^{0}\frac{\partial}{\partial z}wTdz=\frac{Q_{\downarrow}}{\rho C_{p}}$$

(1.12)

where $\vec{v}$ is the horizontal velocity, w is the vertical velocity.

Together with continuity equation, Eq. (1.11) becomes the divergent heat budget equation (Emery, 1976):

$$\frac{\partial T_{a}}{\partial t}-w_{D}\left(T_{a}-T_{D}\right)+\vec{v}_{a}\cdot\nabla T_{a}=\frac{Q_{\downarrow}}{\rho C_{p}D}$$

(1.13)

where T_a, $\vec{v}_a$ are the vertically averaged temperature and horizontal velocity terms, w_D is a upwelling velocity at the depth of D, T_D is the temperature at that depth.

1.2.2 Heat budget model for the upper layer ocean

For the upper-ocean heat budget, the heat stored was calculated down to an isotherm from the surface, following the logic of Emery (1976), Stevenson and Niiler (1983) and Yan et al. (1995), Moisan and Niiler (1998) integrated Eq. (1.7) from the surface down to a chosen isotherm $h = f(x,y,t)$, yields

$$h\frac{\partial T_{a}}{\partial t}+h\vec{v}_{a}\cdot\nabla T_{a}+\nabla\cdot\left(\int_{-h}^{0}\vec{\hat{v}}\hat{T}dz\right)+\left(T_{a}-T_{-h}\right)\left(\frac{\partial h}{\partial t}+\vec{v}_{-h}\cdot\nabla h+w_{-h}\right)=\frac{Q_{0}-Q_{-h}}{\rho C_{p}}$$

(1.14)

where T_a, $\vec{v}_a$ are the vertically averaged temperature and horizontal velocity terms, $\hat{v}$ is the deviation from the vertically averaged horizontal velocity, and $\hat{T}$ is the deviation from the vertically averaged temperature.

After neglecting the horizontal eddy heat transport term (the third term on the left hand side) and entrainment cross lower surface (the fourth term on the left hand

13

side), the final equation for heat content rate becomes the balance of a horizontal heat advection term and net heat flux term (Moisan and Niiler, 1998)):

$$h\frac{\partial T_a}{\partial t} + h\vec{v}_a \cdot \nabla T_a = \frac{Q_\downarrow}{\rho C_p}$$

(1.15)

1.2.3 Ocean heat content dynamic equation for the upper ocean

Frankignoul (1985) developed the dynamics equation for temperature anomaly in the sea surface mixed layer from the heat conservation equation:

$$h\frac{\partial T}{\partial t} + h\vec{v} \cdot \nabla T + \left(T - T_+\right)w_+ - kh\nabla^2 T = \frac{Q - Q_+}{\rho C_p}$$

(1.16)

where subscript plus denotes the values at the bottom of the mixed layer.

If each variable is decomposed into a seasonal varying mean (long term climatology, denoted by an over bar) and an anomaly (denoted by a prime). Eq. (1.16) can be written as (Frankignoul, 1985):

$$\frac{dT'}{dt} = \frac{Q'}{\rho C_p \bar{h}} - \frac{(hv)' \cdot \nabla(\bar{T}+T')}{\bar{h}} - \frac{h'}{\bar{h}}\frac{\partial \bar{T}}{\partial t} - \frac{(T'-T_+')(\bar{w}_e+w_e')}{\bar{h}} - \frac{(\bar{T}-\bar{T}_+)}{\bar{h}}w_e' + \kappa\nabla^2 T'$$

(1.17)

where the 6 terms of the right-hand side describe the effect of the following processes respectively: anomalies in the net surface heat flux, heat advection by anomalous current, anomalies in the mixed-layer depth, the anomalies in the temperature jump in the entrainment zone, anomalies in the entrainment velocity, and horizontal mixing. The terms fall into 3 categories: the atmospheric forcing, the variability in the ocean interior that distort the upper layer by horizontal advection and vertical motion near the mixed-layer base, and the damping terms for temperature anomalies.

14

Combine Eq. (1.2) and Eq. (1.17), we have the equation for the upper ocean OHC dynamics:

$$\frac{dH}{dt} = Q' - \rho C_p \left[(hv)' \cdot \nabla(\bar{T} + T') + h'\frac{\partial \bar{T}}{\partial t} + (T' - T_+')(\bar{w}_e + w_e') + (\bar{T} - \bar{T}_+)w_e' \right] + \bar{h}\kappa\nabla^2 T'$$

(1.18)

The terms on the right-hand side of Eq. (1.18) have the same physical meaning as that of Eq. (1.17), but for the upper ocean OHC. For the upper ocean which includes whole layer, a similar decomposition on Eq. (1.11) and Eq. (1.12) would be more appropriate (detailed information in Section 3.3).

1.3   Brief Review of Methodology

1.3.1   Ocean remote sensing oriented to subsurface and deeper ocean application

The ocean surface is dynamically influenced at the sea surface by waves, wind shear, heat exchange, and from the interior ocean by thermal expansion, ocean circulation, and turbulent mixing. Many important ocean processes and features are located well below the surface and at considerable depths. Variation in the subsurface layer will very likely leave traces on the sea surface through sea surface height changes, which make possible estimation for subsurface parameters from sea surface information. The relation between sea surface parameters and subsurface parameters has been studied since the wide application of ocean remote sensing technology (Khedouri et al., 1983; Yan et al., 1990; Chu et al., 2000; Ali et al., 2004), this is ocean remote sensing oriented to subsurface and deeper ocean application, or so called subsurface and deeper ocean remote sensing (Klemas and Yan, 2014). On one hand, sensors that could measure subsurface parameters directly are still developing

(Leonard et al. 1977). On the other hand, studies have been carried out to estimate subsurface parameters from sea surface information based on either the combination of dynamical models (Yan et al., 1990, 1991a, 1992), statistical and empirical methods of historical in-situ observations (Chu et al., 2000) and model-based data assimilation (Robinson and Lermusiaux, 2000).

1.3.1.1   Dynamic approaches

Relationship between sea surface and subsurface parameters can be established through dynamic analysis through some simplifications or approximations. The subsurface parameters then can be inferred from sea surface observation with the established relationship, and then their processes and mechanisms can be monitored and studied from remote sensing. Based on a mixed layer thermal inertia model, one dimensional (Yan et al., 1990, 1991a, 1991b) and three dimensional (Yan et al., 1992) models were developed to determine oceanic mixed layer depth (MLD), which is much simpler than the Kraus and Turner (1967) mixed layer model and can be conducted directly from satellite observations. With the support of in-situ measurements data, phenomena that occur at even deeper than MLD can be revealed from the signal at sea surface. Enhanced TOPEX/POSEIDON、ERS-1 and ERS-2 altimetry were used to monitor cascade of the outflow deep water from the polar basin through Denmark Strait (Høyer et al., 2002), since the stretch induced by the outflow was so strong to penetrate the several hundred meters overlying water and it generated eddies on the sea surface (Krauss and Kase, 1998). A unique method has been developed by Yan et al. (2006) using satellite altimetry, wind scatterometer, infrared satellite imagery and XBT data sets that successfully detected the Mediterranean outflow and 'Meddies' at a depth of about 1000m in the Atlantic Ocean.

1.3.1.2 Model-based data assimilation

Numerical model based data assimilation become a powerful methodology to estimate parameters in the ocean (Ghil and Malanotte-Rizzoli, 1991) by developing some computational technologies. By combining the numerical model with in-situ measurements data and governing the ocean dynamic principles, these give more efficient, accurate and realistic estimations for interested parameters eventhough in several aspects may introduce uncertainties (Robinson and Lermusiaux, 2000, Fischar, 2000; Thacker et al., 2004; Oke et al., 2008). There are many operational ocean reanalysis systems around the world, such as SODA, ECCO, GODAS, GODAE and HYCOM, which provide online data sets available for open use , that contribute to the recent progress in ocean dynamic, biological, chemical and global climate change studies.

The reanalysis output from data-assimilation numerical models have been one of the most popular and effective alternative options for such conditions lack of in-situ measurements. Data assimilation can improve numerical model on two aspects: firstly, the initial condition and boundary conditions for regional models, that reduces the error induced by the unrealistic initial state; secondly, to make corrections from from the irrational component bias in the ensemble numerical simulations. The decadal and inter-decadal ocean variability and climate change research aimed to study a geographic dynamic system including physical, chemical, biological and biogeochemical processes and their interactions. To understand such a synthetical nonlinear system, and the ultimate aim predict it, 4D data assimilation (Bouttier & Courtier, 2002) is an indispensible approach to combine multi-sources of observation results that it is still discontinuous in spatial and temporal dimension on a generally cross-related framework. This framework will lead to a better understanding of the

comprehensive scientific questions. However, the numerical models is just an ensemble of part of the known physical relations between parameters in ocean and climate system, the results from such models is not necessary completely true even if the physical processes and mechanisms are already known, but it is not able to reproduce the realistic state of the ocean and climate system. The physical processes and mechanisms that were assembled in diverse models are different from each other. Limited by the understanding of the ocean and climate system, the results from ocean models can only reflect partially of the realistic world. For example, none of the 115 models of the first stage in CMIP5 of WCRP reproduced the global warming hiatus since 2000, the major reason of this is the mechanisms and processes of this hiatus might have not been known yet.

1.3.1.3 Statistical and empirical approaches

The vertical extension of the remote sensing data to the subsurface, based on statistical and empirical relations between sea surface and subsurface that were built form historical in-situ measurement data, contains the unknown or still lack of study to understand these processes and mechanisms. This approach can avoid the shortcoming of data assimilation mentioned above, and provide valuable data for subsurface and deeper ocean data assimilation.

The altimetry data was firstly introduced to estimate subsurface thermal structure in the Gulf Stream area based on a statistical relation between SSHA and STA (Khedouri et al., 1983). Chu et al. (2000) developed a parametric model for determining the subsurface thermal structure of the ocean from satellite sea surface temperature (SST) observations in the South China Sea. Willis et al. (2003) combined altimetry height and SST with in situ data by using a linear regression technique and

have improved estimation of 0/800 m steric height, heat content, and temperature variability. Ali et al. (2004) used a neural network to determine subsurface thermal structure from SST, sea surface height (SSH), wind stress, net radiation, and net heat flux obtained from a mooring system deployed in the Arabian Sea. Guinehut et al. (2004) derived large scale, monthly mean temperature at 200-m depths from altimetry and SST data through a multiple linear regression method, to combine high spatial resolution satellite altimetry data with sparse high accuracy Argo temperature. Takano et al. (2009) developed an empirical method to estimate mesoscale three-dimensional thermal structure from near-real-time satellite altimetry data based on a two-layer model hypothesis.

The statistical approach for estimating parameters, which has been used for some decades is not constrained by the dynamical equations, and the predicted parameter may be limited to the range of the available data. However, this approach is relatively easy to establish and has reasonable accuracy. In the subsurface ocean where the in-situ data is limited, statistical estimation is a necessary and useful supplement to the model-based parameter estimation.

SST and SSH have been monitored by remote sensing since the late 1970's and 1992 respectively. Two salinity sensors, Soil Moisture and Ocean Salinity (SMOS) satellite by the European Space Agency and Aquarius by NASA and Argentina, have been launched in 2009 and 2011. Cross validation for the sensors will make the global sea surface salinity (SSS) data more reliable than before. Since SSTA, SSHA and SSS anomaly (SSSA) recently can be obtained through remote sensing platforms; in this paper a self-organize-mapping neural network is adopted to estimate the subsurface temperature structure from these datasets with the help of Argo in-situ data.

In this dissertation, we focus on ocean remote sensing oriented to subsurface and deeper ocean application. Based on the physical or dynamical relation or statistical and empirical characteristic relations between historical remote sensing sea surface parameter and in-situ measurements of subsurface parameters, new approaches for extending remote sensing to subsurface and deeper ocean were developed. The generated method and data sets may shed light on the understanding of related physical processes.

1.3.2　Empirical Orthogonal Function

The EOF (Empirical Orthogonal Function) analysis is a principal component analysis (PCA) applied to a group of time series data. The EOF analysis is the time domain analysis that is basically the computation of eigenvector and eigenvalue of a covariance or a correlation matrix computed from a group of original time series data. Coherent variations among a group of original time series data can be extracted to create a new group of time series data by using original time series data and eigenvectors. One of the important things about these new time series data is that they are statistically non-correlated with each other. In other words, EOF separates coherent variations mixed in the group of original time series data into several components and these components themselves are not correlated with each other. So the causes of individual variations component might be identified separately. The magnitude of eigenvalues shows how important these new time series data are. The eigenvectors shows similar information but for each individual original time series.

1.3.3 EEMD

Ensemble Empirical Mode Decomposition (EEMD) is an advanced version of Empirical Mode Decomposition (EMD). The purpose of the EMD is to reduce a complicated data set into a finite and generally small number of intrinsic mode functions (IMFs, Huang et al., 1998). EMD can empirically identify different oscillatory modes in the data based upon their time scales and separates the data into IMFs, using the time lapse between successive extrema as the basis for sifting the data into modes. However, the EMD has major drawbacks of frequent appearance of mode mixing. To overcome this shortcoming, a new noise-assisted EMD analysis, EEMD, is proposed by Huang and Wu (2008). EEMD is an algorithm that works as follows: (1) add a white noise series to the data, (2) decompose the data plus noise into IMFs, (3) repeat the first two steps with different white noise, and (4) obtain the ensemble mean of the IMFs for the results (Huang and Wu, 2008).

1.3.4 Causality analysis

Causal analysis between OHC in Atlantic Ocean and OHC in the Southern Subtropical Indian Ocean is carried out following the method proposed by Liang (2014). The causality is measured by information flow between two time series, e.g. X_1 and X_2. The rate of information flow (units: nats per unit time) from the latter to the former (Liang, 2014) is

$$T_{2 \to 1} = \frac{C_{11}C_{12}C_{2,d1} - C_{12}^2 C_{1,d1}}{C_{11}^2 C_{22} - C_{11}C_{12}^2} \tag{1.19}$$

where C_{ij} is the sample covariance between X_i and X_j, $C_{i,dj}$ is the covariance between X_i and the time differential approximation of X_j, which is defined as $\frac{X_{j,n+k} - X_{j,n}}{k\Delta t}$. This method has been applied to investigating the complex relation between El Niño and

IOD, results indicating that El Niño tends to stabilize IOD, while IOD functions to make El Niño more uncertain (Liang, 2014).

1.4 Dissertation Outline

From a perspective of ocean heat content, the mechanisms and processes of global warming and hiatus and regional oceanic and atmospheric responses to global climate change were investigated in this dissertation. The framework for this dissertation is shown in Fig 1.4.
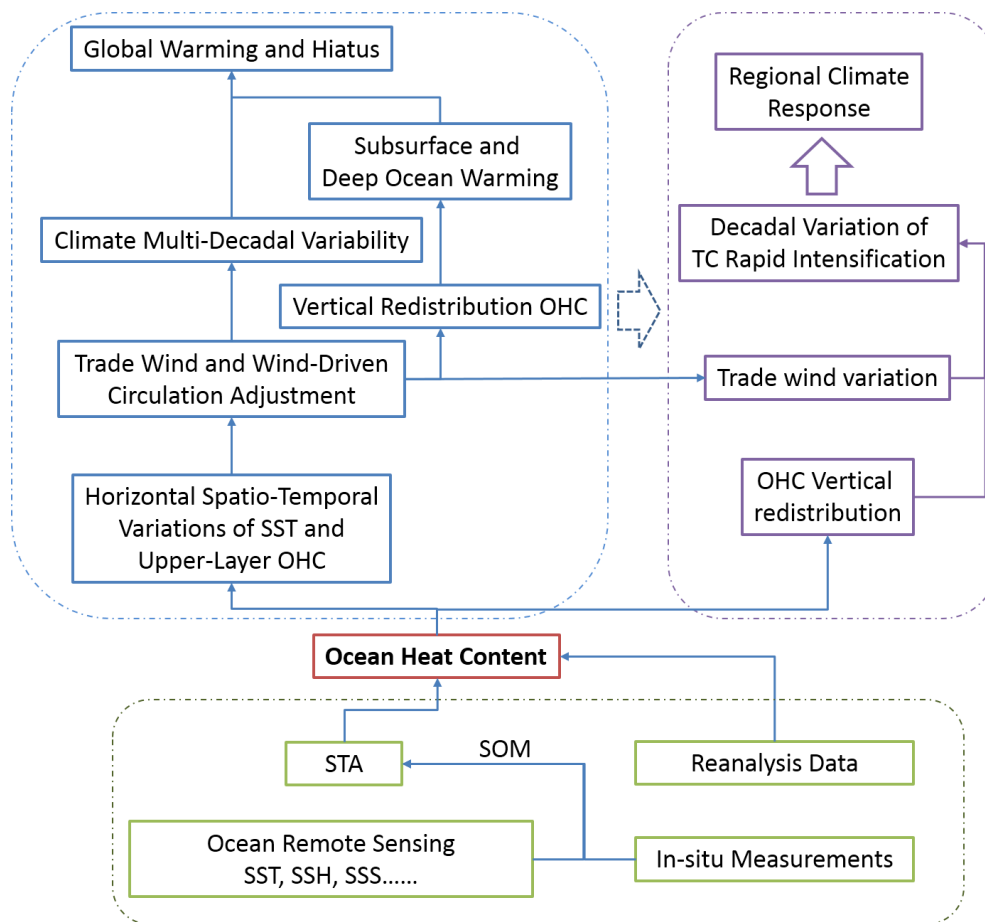
Fig. 1.4 Framework of the research of global warming hiatus and regional climate response.

In Chapter 2, to provide more subsurface temperature for decadal ocean heat content study, methods were developed to estimate temperature anomaly for subsurface and deeper layer from sea surface parameters provided by remote sensing and in-situ measurement for Argo. A Self-Organizing Map Neural Network (SOM) was developed from Argo gridded data sets in order to estimate subsurface temperature anomaly (STA) from remote sensing data. The SOM maps were trained using anomalies of sea surface temperature (SST), height (SSH) and salinity(SSS) data from Argo gridded monthly anomaly data sets, labeled with Argo STA data for 2005~2010 and then used to estimate the STAs at different depths in the North Atlantic from the sea surface data. The estimated STA maps and time series were compared with Argo STAs including independent data sets for validation. STA time series for 1993~2004 in the mid-latitude North Atlantic were estimated from remote sensing SST and altimetry time series using the SOM algorithm.

In Chapter 3, OHC spatio-temporal variations were analyzed using the empirical orthogonal function analysis for global scale and for southern Atlantic and Indian Ocean to find out the mechanisms for global warming and hiatus, and the important role Indian Ocean played in global climate change. A meridional dipole has dominated the variation of the ocean heat content in the upper layer, and the warming in the upper layer of the Indian Ocean has been in "hiatus" since early 1980s, Further, a very new and sophisticated causal analysis method revealed that the warming in the southern subtropical Indian Ocean contributed to the pre-conditioning and warming in

the southern and tropical Atlantic since 1980s and to the heat sequestration at the deeper layer in the Southern Ocean during the global surface warming hiatus period.

In Chapter 4, the decadal variation of vertical OHC distribution and its impact on air-sea interaction in Western North Pacific were studied to reveal regional climate respond to global warming hiatus. The decadal variation of rapid intensification of Tropical Cyclones (TCs) in Western Northern Pacific were studied using TC best track datasets. A new index for Rapid Intensification of Intense TCs (RITC), defined as the maximum wind speed increase and central pressure drop within 24 hour during TC lifetime, was proposed to study the variations of the TC intensity. Based on a qualitative model for RITC, the decadal variations of RITC during GAW and Global Warming Hiatus (GWH) periods were discussed. During GAW period with weakened eastern trade wind, the RITC was controlled by OHC of upper ocean, and during GWH periods with strengthened eastern trade wind and warming subsurface, the RITC is higher than that did during GAW period, indicating higher intensity and frequency of intense TC activity.

Chapter 2

SUBSURFACE THERMAL STRUCTURE ESTIMATION

2.1 Introduction

Since the 1970s, remote sensing has provided huge amounts of high spatial and temporal resolution, large overall coverage, and long time series of sea surface data, allowing for unprecedented progress and notable discoveries in atmosphere, ocean and climate sciences. While remote sensing is the most cost-efficient tool, its observations are confined to the sea surface phenomena. Therefore, our knowledge of the sea surface greatly exceeds what is known below the surface. Subsurface data, however, is critical to understand the mechanisms and processes in the ocean as a whole, as well as for the entire earth climate system (e.g. Meehl et al., 2011). Despite the large subsurface in-situ measurement projects such as Integrated Ocean Observing System (IOOS) and Global Ocean Observing System (GOOS) with over 8000 platforms including drift buoys, moored buoys, Argo floats, gliders and Expendable Bathythermographs (XBTs), the subsurface observations available are still too scarce in most parts of the ocean.

The ocean surface is dynamically influenced at the sea surface by waves, wind shear, heat exchange, and from the interior ocean by thermal expansion, ocean circulation, and turbulent mixing. Variation in the subsurface layer will very likely leave traces on the sea surface through sea surface height changes, which make the estimation of parameters from the subsurface form the sea surface possible. The relation between sea surface parameters and subsurface parameters has been studied

(Khedouri et al., 1983; Yan et al., 1990; Chu et al., 2000; Ali et al., 2004). On one hand, sensors that could measure subsurface parameters directly are under development (Leonard et al. 1977). On the other hand, studies have been carried out to estimate subsurface parameters from sea surface information based on either the combination of dynamical models (Yan et al., 1990, 1991a, 1992) , in-situ observations (Chu et al., 2000) and model-based data assimilation (Robinson and Lermusiaux, 2000). Numerical model based data assimilation become a powerful methodology for parameter estimation in the ocean (Ghil and Malanotte-Rizzoli, 1991) with the development of computational technology. It combines the in-situ measurements and the dynamic principles that govern the ocean, gives most efficient, accurate and realistic estimation for parameter interested, though it has several aspects may introduce uncertainty (Robinson and Lermusiaux, 2000). The statistical approach for parameter estimate, which has been used for decades, is not constrained by the dynamical equations and the predicted parameter may be limited to the range of the available data. However, this approach is relatively easy to establish and has reasonable accuracy. In the subsurface ocean where the in-situ data is limited, statistical estimation is a necessary and useful supplement to the model-based parameter estimation.

Based on a mixed layer thermal inertia model, one dimensional (Yan et al., 1990, 1991a, 1991b) and three dimensional (Yan et al., 1992) models were developed to determine oceanic mixed layer depth (MLD), which is much simpler than the Kraus and Turner (1967) mixed layer model and can be conducted directly from satellite observations. With the help of in-situ measurements, phenomena occurring at even deeper than MLD can be revealed from the signal at sea surface. A unique method has

been developed by Yan et al. (2006) using satellite altimetry, wind scatterometer, infrared satellite imagery and XBT data sets that successfully detected the Mediterranean outflow and 'Meddies' at a depth of about 1000m in the Atlantic Ocean. Chu et al. (2000) developed a parametric model for determining the subsurface thermal structure of the ocean from satellite sea surface temperature (SST) observations in the South China Sea. Willis et al. (2003) combined altimetric height and SST with in situ data with a linear regression technique and improved estimates of 0/800 m steric height, heat content, and temperature variability. Ali et al. (2004) used a neural network to determine subsurface thermal structure from SST, sea surface height (SSH), wind stress, net radiation, and net heat flux obtained from a mooring system deployed in the Arabian Sea. Guinehut et al. (2004) derived large scale, monthly mean temperature at 200-m depths from altimetry and SST data through a multiple linear regression method, combining high spatial resolution satellite altimetry data with sparse high accuracy Argo temperature. Takano et al. (2009) developed an empirical method to estimate mesoscale three-dimensional thermal structure from near-real-time satellite altimetry data based on a two-layer model hypothesis.

SST and SSH have been monitored by remote sensing since the late 1970's and 1992 respectively. Two salinity sensors, Soil Moisture and Ocean Salinity (SMOS) satellite by the European Space Agency and Aquarius by NASA and Argentina, have been launched in 2009 and 2011. Cross validation for the sensors will make the global sea surface salinity (SSS) data more reliable than before. Since SSTA, SSHA and SSS anomaly (SSSA) can now be obtained through remote sensing platforms; in this paper a self-organize-mapping neural network is adopted to estimate the subsurface temperature structure from these datasets with the help of Argo in-situ data. A SOM

27

neural network is trained and labeled from Argo gridded data. Validations are carried out by comparing the horizontal maps, vertical profiles and time series of SOM estimated STA with Argo STA data. The method is applied in the mid-latitude North Atlantic to estimate the subsurface thermal structure from remote sensing SST and altimetry. Sensitivity of this method to input parameters are discussed, followed by conclusions on the capability of the method in estimating sub surface thermo-structure in the North Atlantic.

2.2   Data and Method

2.2.1   Data summary

Datasets used in this study are monthly global gridded Argo data provided by International Pacific Research Center (IPRC, http://iprc.soest.hawaii.edu) at the School of Ocean and Earth Science and Technology, University of Hawai'i at Mānoa. The temperature, salinity and Absolute Dynamic Topography datasets have 1×1 degree horizontal spatial resolution and global coverage, and were interpolated to 27 standard depth levels in the upper 2000m from January of 2005 to December of 2010. The absolute dynamic height (ADH) in the IPRC gridded Argo data is defined as SSH minus Dynamic height (DH), where the SSH is obtained from altimeter products. At the sea surface, ADH is equal to SSH. ADH data is calculated using Aviso altimetry referred to MDT_CNES-CLS09 (MDT_CNES-CLS09 was produced by CLS Space Oceanography Division and distributed by AVISO, with support from CNES, http://www.aviso.oceanobs.com/).

In the section for application of SOM algorithm, NOAA Optimum Interpolation   Sea   Surface   (NOAA_OI_SST_V2:

http://www.emc.ncep.noaa.gov/research/cmb/sst_analysis/) Temperature anomaly monthly data and monthly Maps of Sea Level Anomalies (MSLA) from altimetry distributed from AVISO (http://www.aviso.oceanobs.com/es/data/products/sea-surface-height-products/global/msla/index.html) were used as input data to estimate the STA. The MLD extends from about a few tens of meters to 200m depth in most of the tropical and mid-latitude ocean (de Boyer Montégut et al., 2004). Considering the MLD for high latitudes, 300m is chosen reasonably to represent the subsurface layer depth. The data sets have a 1°x1°(Mercator grid) spatial resolution, which is the same as that of Argo data sets which were used in training and labeling processes. The SST data is a combination of in situ and satellite SSTs.

2.2.2 Ocean heat content and sea surface parameters

Based on the thermal expansion of seawater, the ocean heat content can be calculated from sea surface height anomalies observed by a satellite altimeter (Chambers et al., 1997; Yan et al., 2004):

$$H_{Alt} = \frac{\rho C_p}{\alpha_T} \eta'_{Alt}$$

(2.1)

where H_{Alt} is the OHC estimated from altimeter data, α_T is the thermal expansion coefficient, η'_{Alt} is the sea surface height anomaly (SSHA) from satellite altimetry. The results from Eq. (2.1) showed large discrepancies from the OHC from XBT data. The reason is the SSHA contains not only the thermal steric height, but also nonthermal steric height such as salinity, wind stress forcing and wave etc (Yan et al., 2004):

$$\eta'_{Alt} = \eta'_{thermal} + \eta'_{salinity} + \eta'_{wind} + \eta'_{wave}$$

(2.2)

where the subscriptions denote different mechanisms for sea level change.

Based on Eq. (1.14), Eq. (1.17), Eq. (2.1) and Eq. (2.2), we have:

$$T' = f(\eta', T_S', \cdots)$$ (2.3)

where T_S' is the SST anomaly, η' is SSHA. The sub surface temperature anomaly T' is a function of sea surface anomaly data and other related dynamic parameters.

Self-Organize Mapping Neural Network Self-Organize Mapping Neural Network is a computational method for the visualization and analysis of high-dimensional data. It was first introduced by Kohonen (1982, 2001) as an unsupervised neural network to study empirical relationships between variables of which the physical relationships are not clear and has turned out to be very useful tool in feature extraction and classification. It has been widely applied in meteorology and ocean science (Liu et al., 2006; Telszewski et al., 2009; Liu and Weisberg, 2011).

The subsurface temperature estimation was carried out using a SOM Toolbox for Matlab, which is developed by the Laboratory of Information and Computer Science at the Helsinki University of Technology and available online at http://www.cis.hut.fi/projects/somtoolbox. General SOM procedures contain unsupervised training of available data sets to a 2-D network, labeling the trained network and estimation (Fig 2.1). For detailed descriptions, consult Liu et al. (2006) and Telszewski et al. (2009).

The SOM map adopted in this study consists of 1600 (40×40) neurons with rectangular grids on a flat sheet map and a 'Gaussian' neighborhood function with a radius of 2. This network is to be trained using sea surface information and labeled with STA data before it can be used to estimate the subsurface temperature anomaly.

Telszewski et al. (2009) suggested reducing the data sets into a moderate sized map, not only for consideration of calculation efficiency, but also to provide sufficient representation of patterns to extract all characteristic patterns. To find out the most suitable map size, several tests were carried out: map sizes of 100×100, 80×80, 64×64, 40×40, and 30×30 were tested. The best one was the 40×40 with high calculating efficiency, good estimation, and low RMS level.

For the SOM training process, the data inputs are SSTA, SSSA and SSHA in the North Atlantic Ocean ($25 \sim 63 \,^\circ$North, $80 \sim 0 \,^\circ$West). In this paper, the SSTA, SSSA and SSHA were calculated from the monthly climatology field, so as to avoid the climatology seasonal variation signal, this would improve the sensitivity of the SOM method to temperature anomaly.

Variation of each parameter was normalized to one by the standard deviation, and the mean value was set to zero before training: $x' = (x - x_m)/\sigma_x$, where x is the parameter to be normalized, x' is the normalized parameter, σ_x is the standard deviation of x, and x_m is the mean value of x (Vesanto et al., 2000). The SOM map was trained every year, and 48000 data triplets were used to train one map. In the trained map, each neuron has three components representing all the combinations of input variables (SSTA, SSHA and SSSA). The relationship between these three training parameters, with similar patterns mapped to neighboring regions and dissimilar patterns mapped to separate locations then became the foundation for the labeling and estimation processes.

For each layer, Argo subsurface temperature anomaly data at that depth was used to label the trained neural network, 70% for labeling and 30% for testing. According the sea surface SSTA, SSHA and SSSA, the STA values were labeled onto

31

the nearest neurons by a definition of Euclidean distance (Telszewski et al., 2009). For the neurons that have more than one STA value labeled, the averaged STA value was the final labeling value. Estimation of STA was carried out using the labeled SOM map and sea surface information. Input vectors of arbitrary position and time had one neuron in the labeled SOM map according the Euclidean distance; the STA of that neuron became the estimation of the input vectors. The estimations were implemented every month from the surface down to 2000m depth from January of 2005 to December of 2010 with Argo sea surface data as input and from January of 1993 to December of 2009 with remote sensing data as input.
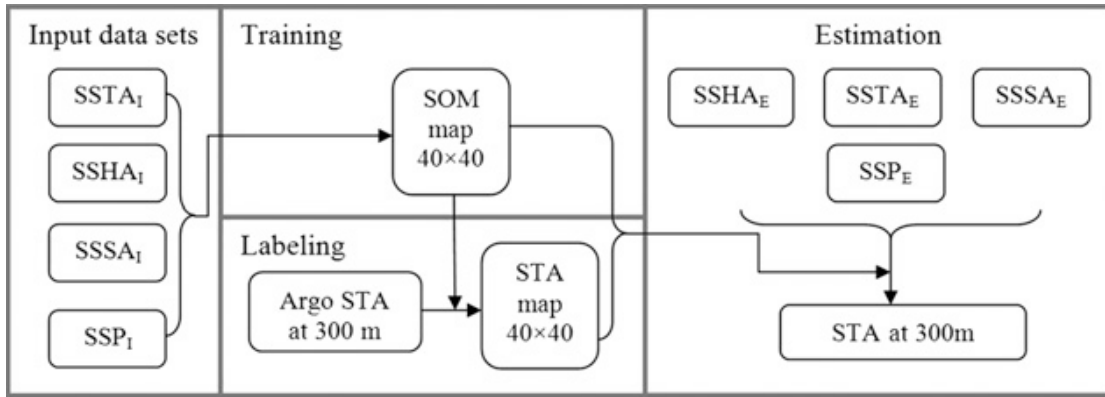
Fig. 2.1 Flow chart for Subsurface Temperature Anomaly (STA, take 300m depth for example) estimation using Self-Organize Mapping neural network: $SSTA_I$, $SSSA_I$, $SSHA_I$ are data sets for training, large data sets from long time series and large coverage of space. $SSTA_E$, $SSSA_E$, $SSHA_E$ are the data sets for estimation, it can be single spot, cruse transaction or horizontal 2-d dimensional maps. SSP is other possible sea surface parameters.

2.3 STA Estimation Using Argo and Remote Sensing Sea Surface Data

2.3.1 Horizontal maps of STA

A total of 72 monthly-averaged STA datasets at all depth levels in the North Atlantic were estimated using a SOM neural network, which is trained using Argo sea surface data and is labeled using Argo STA data. Comparison between the estimated STA and Argo gridded data shows that the basic patterns of STA have been retained by the SOM method (Fig 2.2). The STA variation at 300m depth near the Western Boundary is from -3 to 3 ℃, from the Gulf Stream Separation area to the Irminger Sea, 5 to 6 times larger than other areas, where the STA range varies from -0.5 to 0.5 ℃. The in-situ and estimated STA maps show a similar spatial structure as the SSTA and SSHA: large anomaly values located along the Gulf Stream Path, with the negative anomalies having considerably larger magnitude than the smaller positive anomalies (Fig 2.3). The sensitivity tests also indicate that SSTA and SSHA are the two major driving forces for the STA in the western boundary area (Fig 2.11, will be discussed in details in section 3.5).

2.3.2 Time series

For each pixel and subsurface layer (23 layers, from 30m to 2000m), the relationship between the time series of SOM estimated STA and Argo STA were investigated using correlation coefficient (γ) , root mean squared error (RMSE) and regression coefficients. The highest correlation through the water column from 30m to 2000m depth, the depth of the layer that has highest correlation (Figure 4) and the RMSE between the two data sets at that depth was calculated. In most of the areas between 25 ˚N to 55 ˚N, the correlation is over 0.8 with only two exceptions where correlation is low: the center of North Atlantic Gyre, and the western part of central

Labrador Sea. The depths determined by maximum γ are larger in the western part of the basin (Fig 2.5), extending as far as about 700m to 800m depth, while in the eastern part and the northern part the depth is much smaller and is comparable to the MLD (less than 100m, de Boyer Montégut et al., 2004; Chu and Fan, 2010).

The thermal and dynamic mechanisms of the Eastern/Western of the North Atlantic are completely different. In the western part, the major driving force is the Gulf Stream through strong advection and mixing. The seasonal thermocline can reach up to 1000m depth (Fig 2.6a, Fig 2.7a, 7c), inducing large variations of STA along the Gulf Stream, where the magnitude is about 4℃ (-2.4~1.9℃). However, in the eastern part of the ocean, especially east of the mid-Atlantic Ridge (Fig 2.6c), there are two depths where the temperature variation is relatively large: the mixed layer, extending within less than 100m from the surface, and an 'under current' of warm, high salinity water out-flowing from the Mediterranean Sea (Bozec et al., 2011), located at about 800~1200m depth. The temperature anomaly ranges between -0.6 and 0.6℃, and its variation is about 1/3~1/4 of that in the western basin.

The correlation coefficients at 300m depth were chosen to show the quality of the method. The estimation based on the SOM neural network has a relatively better performance in the Gulf Stream and in the North Atlantic Current path, with the correlation coefficient being about between 0.8 and 1.0. Low correlation coefficient values were found near the center of the Atlantic subtropical Gyre, Bay of Biscay and N. Atlantic Ocean off the coast of Portugal and in the Labrador Sea. The latter two areas have unique thermal dynamic processes which contribute to the change in thermal structure: the Mediterranean outflow (Rahmstorf, 1998; Bozec et al., 2011), and deep convection, which is the source of Labrador Sea Water (Marshall et al.,

1998). The ratio of RMSE between Argo STA and SOM estimated STA to the total variation of Argo were obtained. The areas of relatively smaller ratio (<0.4) almost overlap the areas of high correlation coefficients (>0.8). The areas defined by these two parameters are those where the SOM algorithm has highest confidence level for the STA estimation at 300m or deeper.
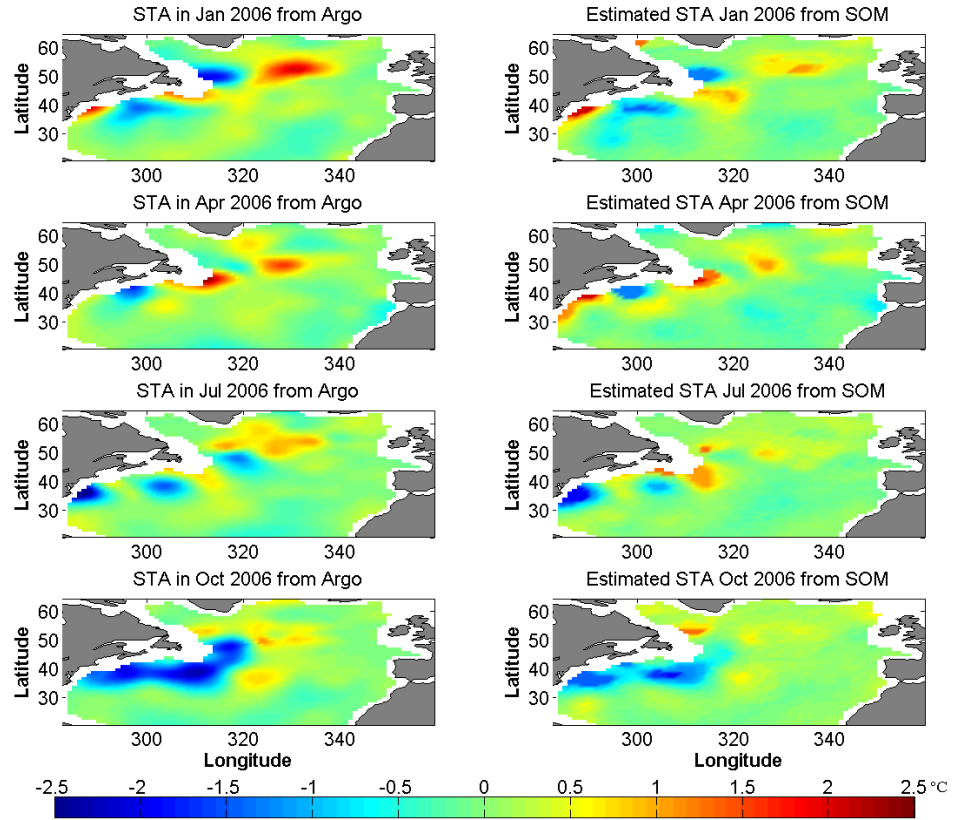
Fig. 2.2 Comparison of Subsurface Temperature Anomaly (STA) at 300m depth, from Argo (left panel) and Self-Organize Map neural network (SOM) estimation (right panel), in Jan, Apr, Jul and Oct of 2006.
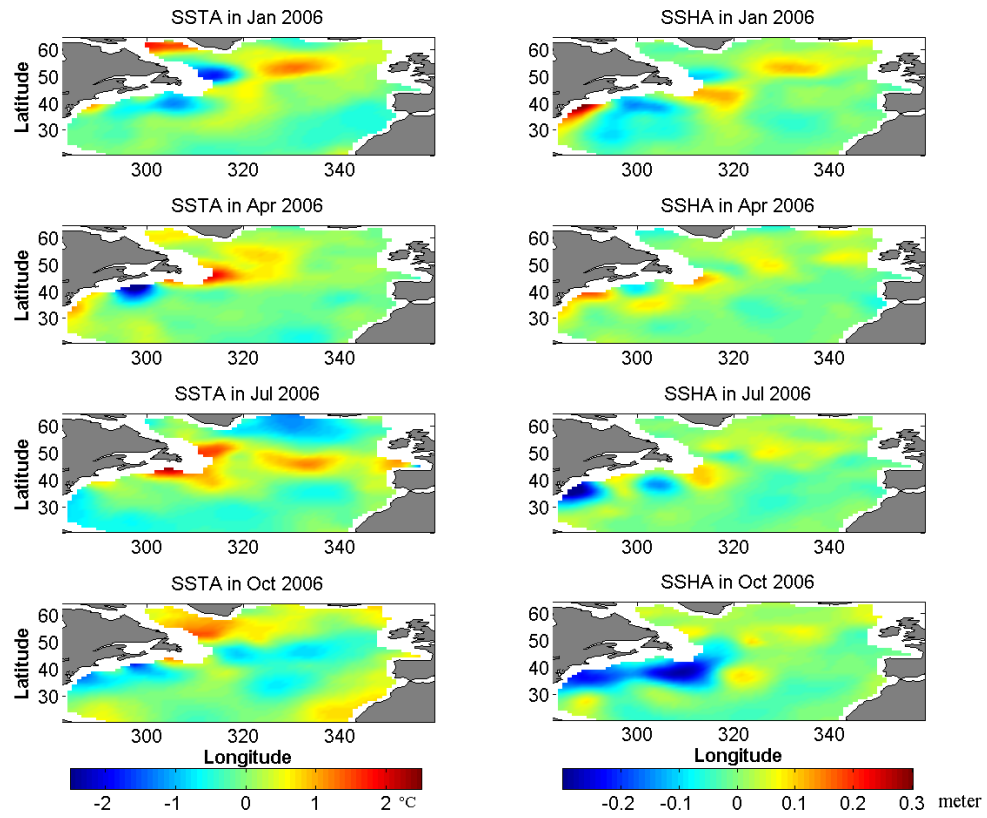
Fig. 2.3 Sea Surface Temperature Anomaly (SSTA, left panel), Sea Surface Height Anomaly (SSHA, right panel) from Argo, in the North Atlantic for Jan, Apr, Jul and Oct of 2006.
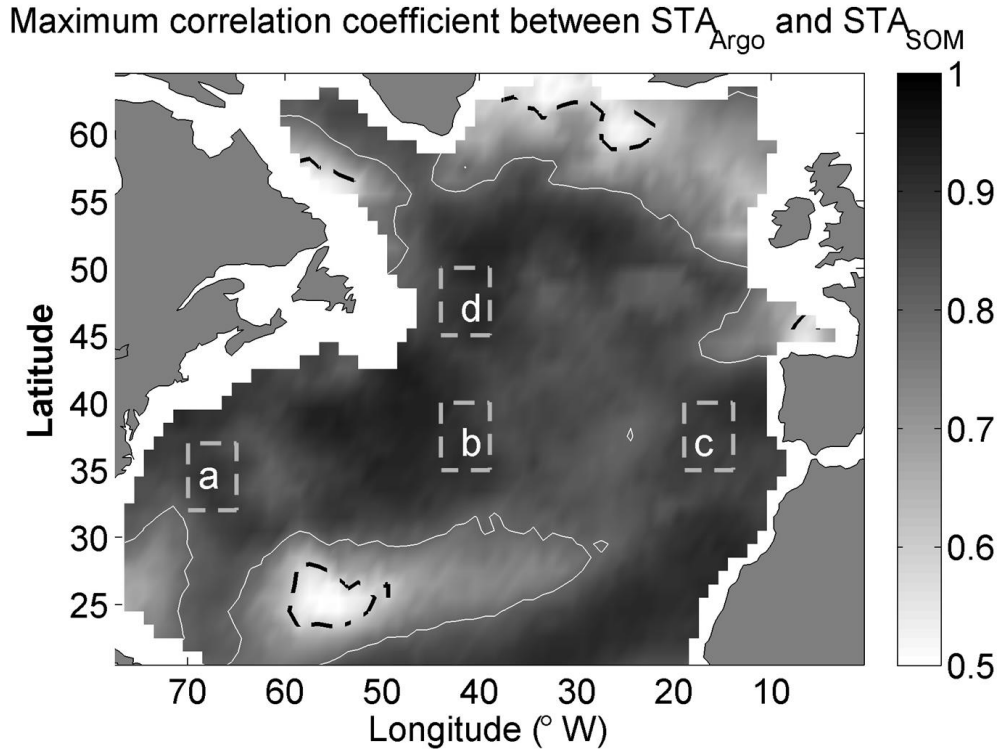
Fig. 2.4 Maximum correlation coefficient (γ) between estimated Subsurface Temperature Anomaly (STA$_{SOM}$) by Self-Organize Map neural network (SOM) and Subsurface Temperature Anomaly from Argo (STA$_{Argo}$) from 30m~2000m depth in the North Atlantic. The solid contour line is for γ = 0.8; the dashed contour line is for γ = 0.6. Areas noted as a, b, c, d are for the labeling and testing in Section 3.4: Area a, western part of the North Atlantic Subtropical Gyre, 65 °~70 °W, 32 °~37 °N; Area b, central part of the mid-latitude North Atlantic, 40 °W~45 °W and 35 °N ~40 °N; Area c, eastern part of the mid-latitude North Atlantic, 15~20 °W, 35 °N ~40 °N; Area d, the Sub-Polar Gyre of the North Atlantic, 40~45 °W and 45~50 °N.

2.3.3 Vertical profiles

The depth at which the SOM STAs have the largest correlation with the Argo STA measurements varies tremendously by location. For example, in the western mid-latitude North Atlantic, the depth of largest correlation can be as high as 500-700m depth, while in most other areas, it is only about 100 m deep (Fig 2.5). To aid in understanding the physical meaning of this depth, Fig 2.6 illustrates the Argo monthly

STA and temperature profiles in selected areas with different dynamic characteristic. The depths of the maximum STA variation and maximum correlation coefficient show a general agreement, especially in the western basin of the North Atlantic, where this depth is near the bottom of the thermocline. Although the depth at the maximum correlation coefficient in area d (Fig 2.6d) is very close to the sea surface, the STA variance is about 4 ℃ and the SOM algorithm has good STA estimation at 500m depth. Fig 2.7 shows the typical temperature profiles in east and west basins of mid-latitude North Atlantic (35 ℃N). In the western basin, the SOM algorithm has good agreement from the surface to about 1000m, while in the eastern part, the SOM algorithm tends to underestimate the STA which means that the temperature profile has less variation and more closely resembles the climatology (Fig 2.8). Along the Gulf Stream path, the STA profiles have large variance near the surface, through the mixed layer, and in the middle of the thermocline (about 800m depth).Variance is instead rather small at a depth of 350m. The STAs are in opposite phase at those two depths. The contribution from these two depths may compensate each other. In this situation, it would be more difficult to predict STA from sea surface signal. The maximum STA is between -0.7 and 0.7 ℃, and this relatively small variation is due to the sustained strength of the Gulf Stream. Moreover, in those areas where the Gulf Stream meanders considerably and produces many eddies the magnitude of STA variance can be as high as 4 ℃ (Area a, b, d shown in Fig 2.4, Fig 2.6a) and 2-3 times larger than in the Gulf Stream before the separation.
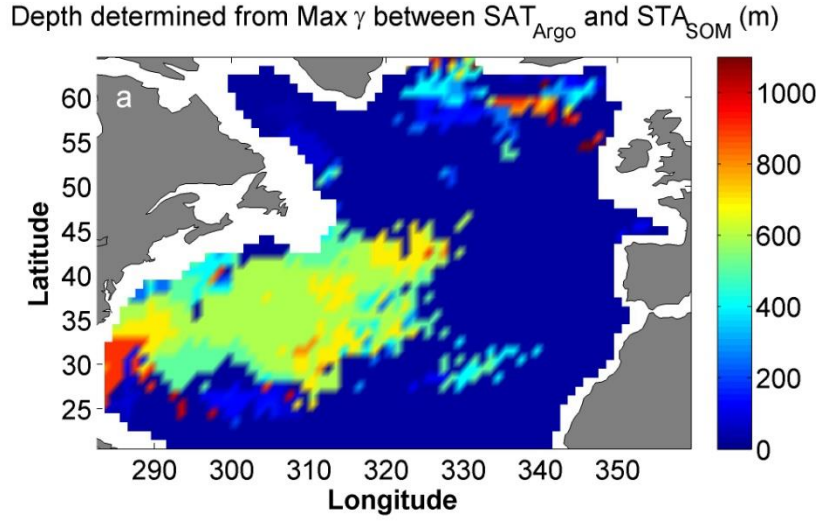
Fig. 2.5 Depth determined from the maximum correlation coefficient (γ) between estimated Subsurface Temperature Anomaly (STA$_{SOM}$) using Self-Organize Map neural network (SOM) and Subsurface Temperature Anomaly from Argo (STA$_{Argo}$) through the water column from 30m~2000m in the North Atlantic.

2.3.4 Validation: comparing labeling and independent data

The gridded Argo STA data sets were randomly divided into 2 parts during the labeling process of the SOM estimation. About 70% of the data was used for labeling the SOM map and the remaining 30% was used as independent data to test the SOM estimation. Four regions were selected for the comparisons (shown in Fig 2.4): The comparisons of SOM estimated STA, labeling Argo STA data, and independent Argo STA data (data that is not used for labeling) were carried out and the results are shown in Fig 2.9 (for 300 m depth). The coefficients of the results for comparison between the time series of SOM STAs and Argo STAs are listed in Table 1 (also at 100m, 500m and 700m depths).

There is good consistency as expected between the labeling data sets and the testing data sets, which were randomly sampled from the same data collection. The

relationship between SOM STA and Argo STA varies with time and location. Generally speaking, the SOM based STA is tending to underestimate the STA. The RMSE between them is about 20% of the total variance of Argo STA. The correlation coefficient at 100 m depth is at the level of between 0.7 and 0.9 (Table 1) with the coefficient for linear regression is between 0.7 and 0.9. On the eastern side of the North Atlantic (area c in Fig 2.4, Fig 2.8), which is not included in the high confidence area, the SOM estimations have some difficulties reproducing the in-situ STA variations. The RMSE level is comparable to the in-situ STA variation, as well as to the accuracy of the SOM estimation method. Along the Gulf Stream Path (area a, b, and d), where many eddies are generated and thermal structure variation is high, the SOM estimation has good performance between the depths of 100 m and 700 m; the γ remains around 0.8 to 0.91 (especially in area d, where γ lies between 0.88 to 0.9) due to the large variation of STA.

The significance of correlation between STA estimated by SOM and Argo gridded STA at 100m and 300m depth in the regions of the Labrador Sea, Bay of Biscay and off the Portugal coast, highlights that the STA derived by the SOM method is not significantly correlated to the measured Argo STA at 300m depth, indicating primarily that the SOM method does not work well for that depth in that area. It consistent with the results from the time series comparison of area c (position shown in Fig 2.4 and Fig 2.6f), the correlation coefficient reduces to 0.5 at the depth of 300m and 0.28 at a depth of 700 m (Fig 2.8, and Fig 2.9c).

Table 2.1 Comparisons of the SOM STA and Argo STA at different locations and depths

* Locations a, b, c, d were shown in Figure 4

Depth(m)	Location*	Correlation coefficient	RMSE	Linear regression ratio
100	a	0.81	0.36	0.65
	b	0.85	0.24	0.75
	c	0.73	0.27	0.41
	d	0.91	0.51	0.69
300	a	0.87	0.29	0.78
	b	0.88	0.20	0.90
	c	0.50	0.13	0.44
	d	0.88	0.5	0.67
500	a	0.86	0.43	0.71
	b	0.91	0.27	0.82
	c	0.72	0.1	1.53
	d	0.89	0.31	0.79
700	a	0.83	0.38	0.64
	b	0.89	0.23	0.77
	c	0.28	0.14	0.24
	d	0.89	0.17	0.96
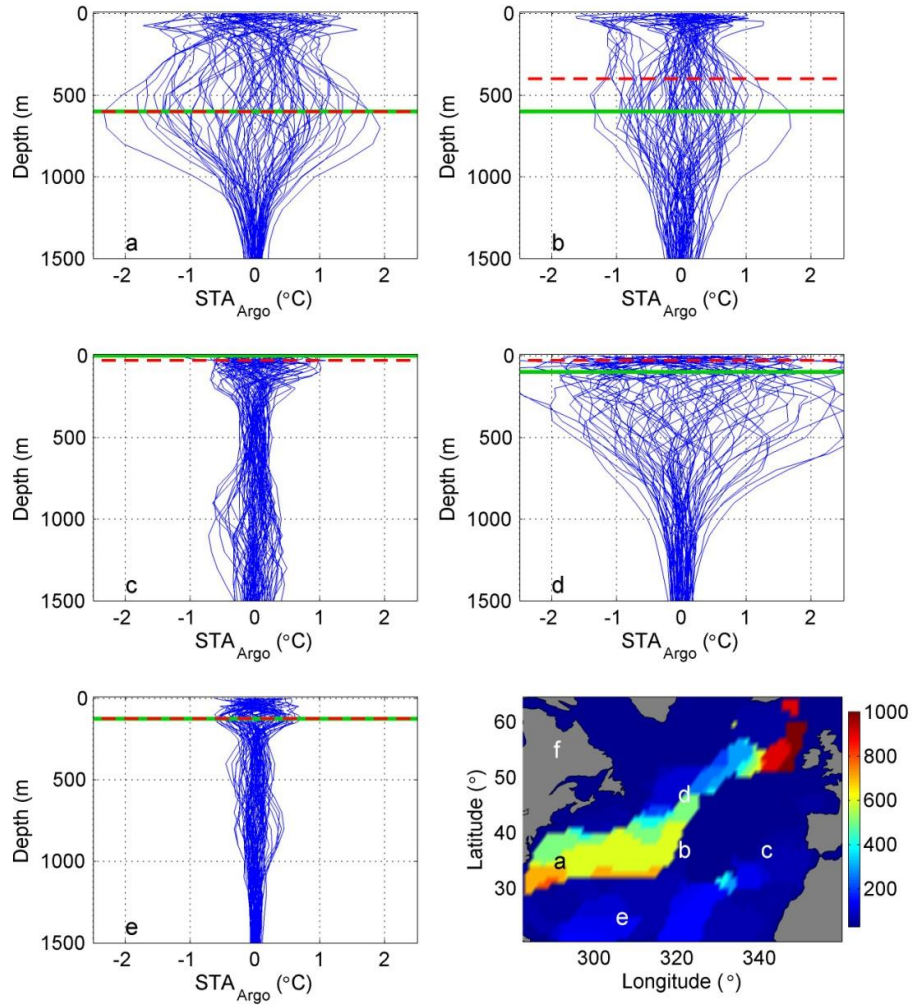
Fig. 2.6 Argo STA profiles from Jan 2005 to Dec 2010 (Fig 2.6a ~ Fig 2.6e in Areas a, b, c, d, and e, geo-locations indicated in Fig 2.6f. The bold green line shows the depth determined from maximum STA variance, while the red dash line is the depth determined from the maximum correlation coefficient (γ) between STA_{SOM} and STA_{Argo}.) And depth determined from maximum STA variance from 30m~2000m in the North Atlantic (Fig 2.6f).
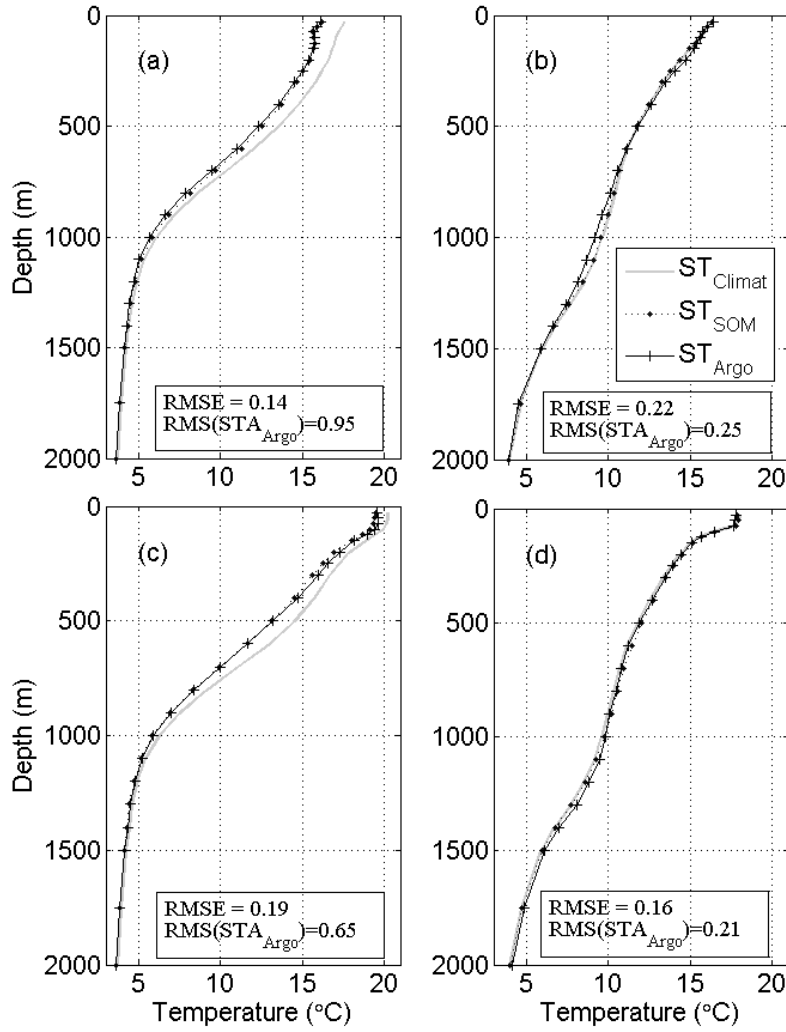
Fig. 2.7 Typical subsurface temperature profiles in Western (Fig 2.7a, &7c, at 35 °N, 60 °W) and Eastern (Fig 2.7b, & 7d, at 38 °N, 20 °W) basins in the mid-latitude North Atlantic during the months of April 2005 (a, b) and December 2005(c, d). The variables plotted are: monthly climatology temperature (ST_{Climat}), temperature from Argo (ST_{Argo}) and temperature estimated by Self-Organize-Mapping neural network (ST_{SOM}). RMSE is between ST_{SOM} and ST_{Argo} and RMS is the root mean square of STA_{Argo} through the water column.
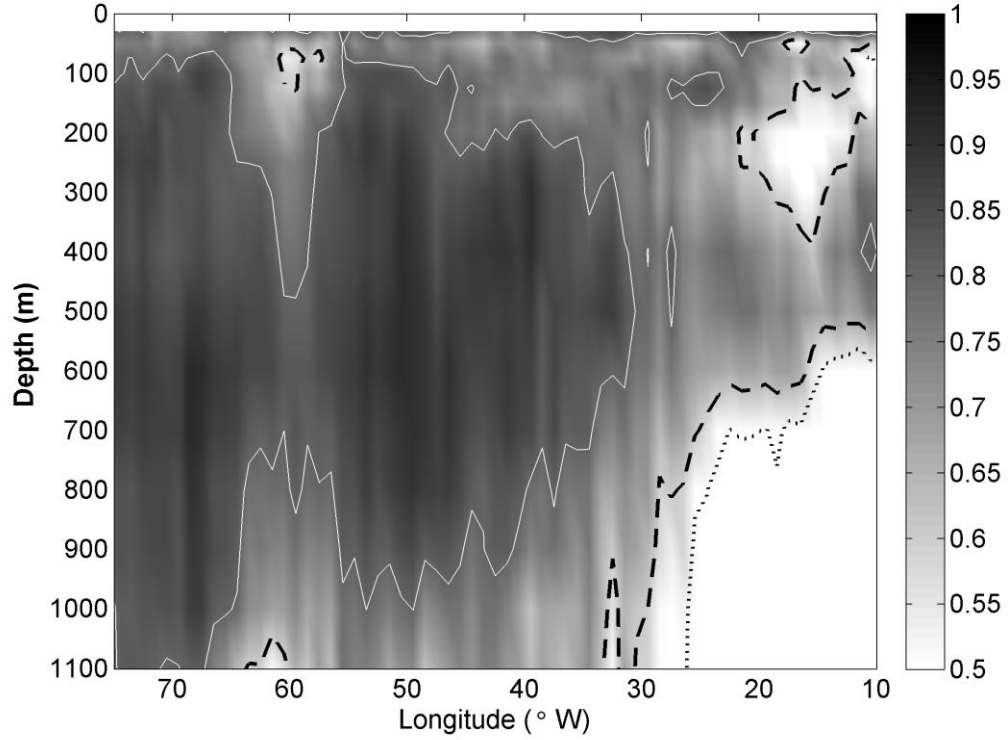
Fig. 2.8 Cross section of correlation coefficient (γ) between Subsurface Temperature Anomaly (STA) estimated from Self-Organize-Mapping neural network (SOM) and STA from Argo from surface (30m) to 1100m at $35\,^\circ$ N in the North Atlantic. The solid contour line is for γ = 0.8, the dashed line for γ = 0.6 and the dotted line for γ = 0.4.

2.4   Sensitivity of Salinity and Climatology in SOM Estimation

Dhomps et al. (2011) used Argo salinity profiles instead of salinity climatology in calculating Sea Level Anomaliesand DHA and obtained an improvement of 35% in the comparison of these two data sets. Comparisons of the SOM estimations were carried out with different training inputs to test the sensitivity of the SOM network to salinity (Fig 2.11). The four input groups are: (1), SSTA and SSHA; (2), SSTA, SSHA and SSSA; (3), SSTA, SSHA and SST Climatology (SSTC), and SSH Climatology

44

(SSHC); (4), SSTA, SSHA,SSSA, SSTC, and SSHC. With the SST and SSH Climatology, the estimation was improved up to 30% in the Labrador Sea. In the Irminger Sea, however, the improvement of SSS was reduced.

By comparing the results with SSSA as one of the inputs in training SOM network, the estimations in the (subtropical) eastern basin of North Atlantic and in the Labrador Sea are improved significantly (up to 30%, in the subtropical North Atlantic, where strongest evaporation takes place) while it is less 10% elsewhere. With the SST and SSH Climatology, the estimation was improved up to 30% in the Labrador Sea and Irminger Sea. Along the Gulf Stream path, the improvement is quite limited (less than 5% improvement) when using the SSSA, SST and SSH climatology. Furthermore, as previous results already show, even the STA estimations with only SSTA and SSHA are has very low RMSE with high correlations (about 0.8~1.0 and p-value is 0.01).

The sensitivity of the salinity in the subtropical ocean (eastern basin) is increased by about 20% when the SST and SSH monthly climatology is included in the training process, indicating that the seasonal variation of SST and SSH plays an important role in the development of subsurface thermal structures. The depths at which the SOM method is sensitive to climatology inputs are about from 1600 to 2000m at high latitudes, and from 1000 to 1500m in the subtropical North Atlantic. The highest sensitivities of salinity are found near the surface, while with SST and SSH climatology, the depth of highest sensitivity in the subpolar ocean reaches down to 1200m depth.
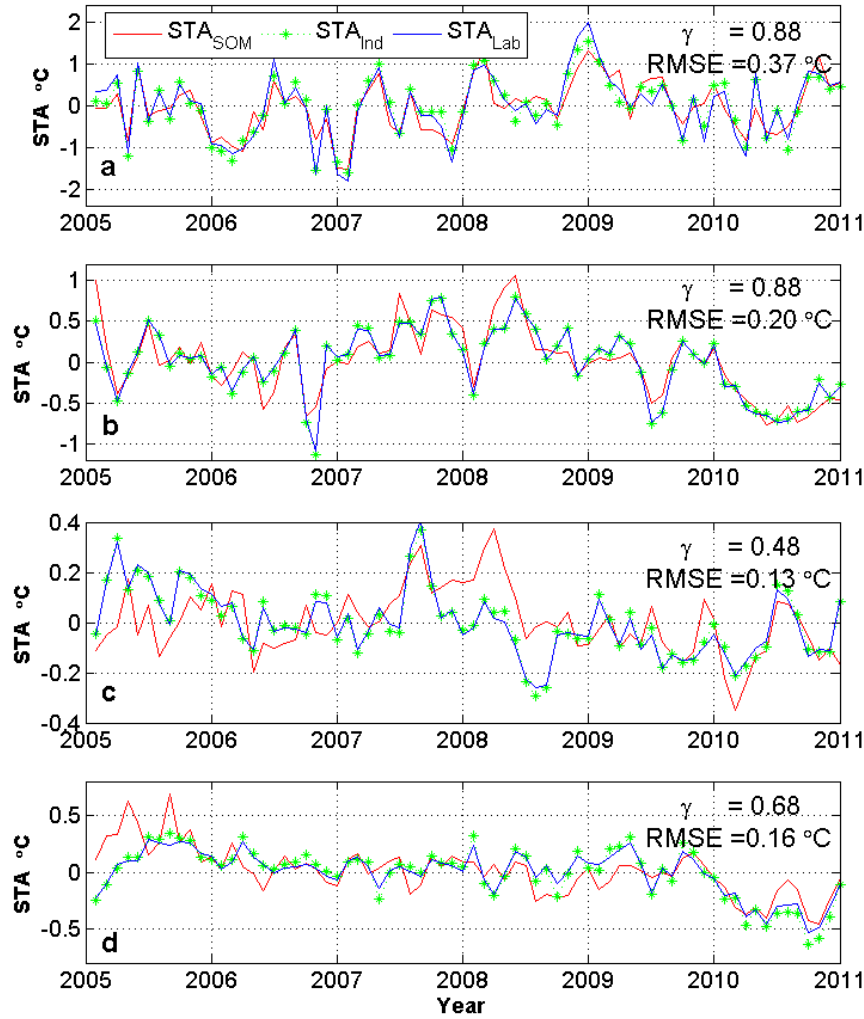
Fig. 2.9 Time series of monthly STA from 2005 to 2010 at 300m depth in the North Atlantic (Fig 2.a, b, c, d for areas a, b, c, d in Fig 2.4 respectively). Colored lines: Red solid line, STA estimated from SOM, STA_{SOM}; Blue solid line, STA from labeling data, STA_{Lab}; Green starred line, STA for independent Argo data, STA_{Ind}. γ is correlation coefficient between STA_{SOM} and STA_{Ind}, RMSE is the root mean squared error between STA_{SOM} and STA_{Ind}.

2.5   STA Estimation from Remote Sensing Data for the Pre-Argo Era

Since the SSS data in the 1990's is not available from remote sensing, in this application, the data sets used for neural network training contains Argo SSTA and SSHA only (from 2005 to 2009). With NOAA Optimum Interpolation SST V2 data (derived from remote sensing and in-situ measurements) and altimetry MSLA data since 1993, the STA at 300m depth was extrapolated backwards to Jan 1993. The STA's at 300m in Jan of 1994 in the mid latitude North Atlantic as an example show reasonable agreement with the SSTA and SSHA measurements (Fig 2.10), including the basic horizontal extension, locations of extreme values of SSTA.

2.6   Discussion and Conclusion

SOM neural network approach is good for visualization and analysis of multi-dimensional data (Liu and Weisberg, 2011). However, there is the possibility that the information of the training data is overly compacted so as to introduce errors during the estimation. The training data sets with certain temporal and spatial resolution (1x1 degree and monthly data in this study) contain information about physical processes of equal or lower resolutions and frequencies. It is not reasonable to expect the SOM method to have high accuracy in the estimation of processes occurring at higher temporal and spatial resolutions and frequencies when compared to that of training data sets. However, by using gridded monthly Argo float data as training datasets, this study can correctly interpret phenomena that vary at seasonal-to-annual timescales.

The results from SOM algorithm are not constrained by the dynamical equations which may lead to various instabilities. We checked the static stability of the reconstructed ocean. Stability defined as (McDougall, 1987), $-(1/\rho)(d\rho/dz)$. The time series of stability for Gulf Stream area at 100m 300m and 500m (Fig 2.12) is

47

greater than 0 (which means the reconstructed ocean is stable) all the time and changed smoothly.
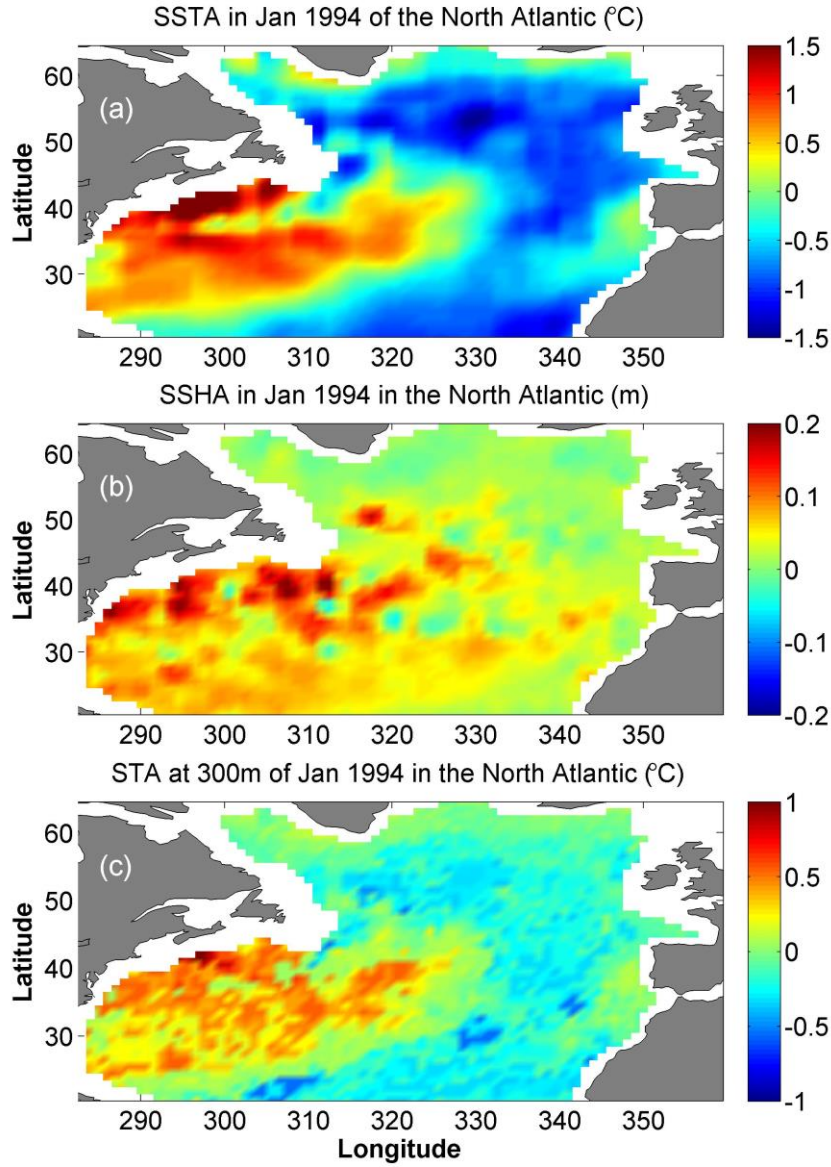
Fig. 2.10 Subsurface Temperature Anomanly (STA) at 300m of Jan 1994 (c) from SOM estimation with remote sensing data (a, SSTA; b, SSHA) as inputs in the North Atlantic.
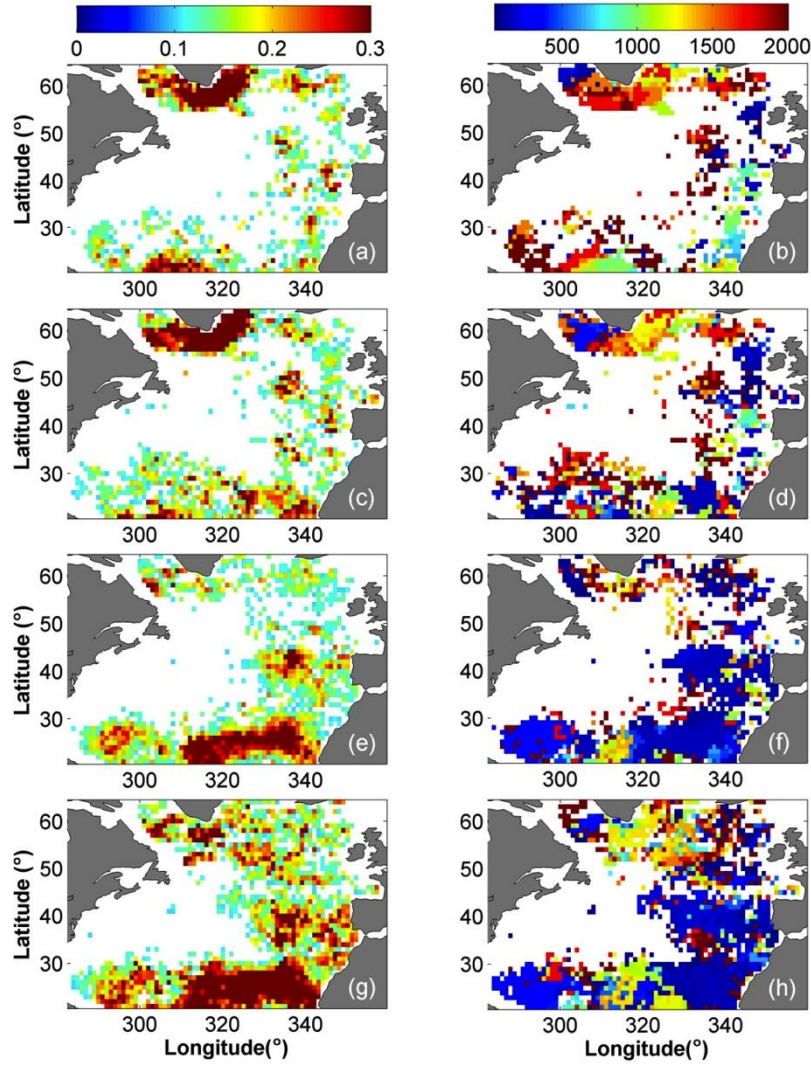
Fig. 2.11 Sensitivity of correlation coefficient (γ) between Subsurface Temperature Anomaly (STA) estimated from Self-Organize-Mapping neural network (SOM) and STA from Argo to the different input for SOM: left panel, changes in γ; right panel, the depth for the changes (m). From top to bottom, the training inputs are: (a, b) γ(SSTA, SSHA, Climatology) - γ(SSTA, SSHA); (c, d) γ(SSTA, SSHA, SSSA, Climatology) - γ(SSTA, SSHA, SSSA); (e, f) γ(SSTA, SSHA, SSSA, Climatology) - γ(SSTA, SSHA, Climatology); (g, h) γ(SSTA, SSHA, SSSA) – (SSTA, SSHA). Grids where Δγ<0.1 were masked.
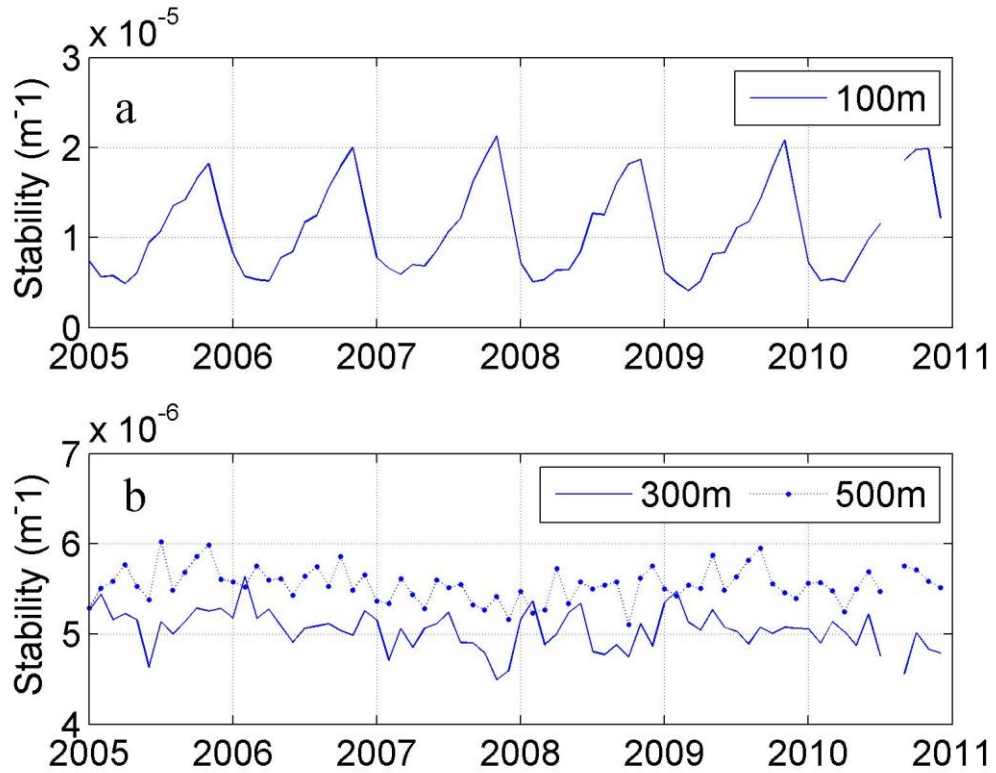
Fig. 2.12 Time series of stability of SOM reconstructed Ocean in Area a (65 °W, 32 ° N) at depth of 100m (a), 300m and 500m (b).

The relationship between sea surface signal and the subsurface temperature could vary widely due to different dynamic processes. In this paper, the data from whole North Atlantic Ocean were used to train and label the SOM, the empirical relationship of all these area were extracted. However, the Gulf Stream and North Atlantic current is by far the most dominant phenomena in this area with their horizontal extend and SSTA, SSHA magnitude. In the center of subtropical gyre in North Atlantic Ocean, warm waters build-up at the top layer and down-welling due to the convergence of surface flow (McClain et al., 2004). In the sub-polar gyre, the situation is slightly the opposite. In the Labrador Sea, warm water from the Gulf

50

Stream cools down and became denser leading to deep ocean convection (Lazier et al., 2002). In order to predict the STA in the Gulf Stream area, the input should include data from that area. At the presence of large anomaly values, the capability of SOM map to resolve the small temperature variation was weakened. This may be responsible for the week correlation coefficient in the center of subtropical gyre and the Labrador Sea (Fig 2.4). Fig 2.8 shows cross section of correlation coefficient (γ) between STA_{SOM} and STA_{Argo} at $35\,^{\circ}N$ in the North Atlantic. The low correlation around 900m depth between $30\,^{\circ}W$ to $10\,^{\circ}W$ may related to the high salinity and temperature Mediterranean Outflow which spread at the depth of about 800m to 1400m (Reid, 1979; Prince et al., 1986; Arhan, 1987). This is an outstanding feature in the North Atlantic, but the overlaid water will damping the salinity and temperature variation, which leads to the difficulty of reconstruction of the STA at the 700m-1100m from the SSTA and SSHA. With a SOM map trained within the east basin of the mid-latitude North Atlantic instead of the whole North Atlantic, the estimation would be improved.

SOM, as a statistical approach for parameter estimate, enables us to predict STA within the" ranges" of inputs data; this may underestimate and miss the signal of some large anomaly events. In the SOM map obtained in the labeling process, the STAs of the neurons are in the range of input data for labeling. For any inputs of sea surface parameter combination, one neuron will be find out as the winning neuron, and the STA value of that neuron will be the output STA for the input data. So SOM algorithm can only predict the STA that lies in the range of labeling data. For those large anomaly events with STA outside of the range of labeling data sets, SOM will underestimate the anomaly.

51

de Boyer Montégut et al. (2004) showed that, for a 0.2 ℃ criterion, the MLD estimated from spatially averaged profiles was 25% shallower than the MLD estimated from individual profiles. The gridded Argo data were generated from the irregularly sampled profiles with the interpolated two/three-dimensionally with variational analysis method. (IPRC Argo gridded Documentation: http://apdrc.soest.hawaii.edu/projects/Argo/data/Documentation/gridded-var.pdf). This may be partially responsible for the errors of the SOM estimation, especially where the Argo profiler density is low.

Using the SOM map trained from anomalies defined from 2005-2010 climatology to estimate the STA in 1990's, may introduce errors. In this study, the anomaly is defined relative to the monthly mean climatology from 2005 to 2010 Argo data rather than the annual or longer-term mean climatology (Ivchenko et al., 2011). This makes the SOM algorithm unaffected by the seasonal variations. In this study, we assumed the climatology did not change over the decades. However, there is long term variation in the North Atlantic with multi-decadal period, such as the Atlantic multi-decadal oscillation (Andronova and Schlesinger, 2000; Enfield et al, 2001; Dima and Lohmann, 2007), which would change the seasonal climatology and as well as the spatial patterns of the physical parameters.

This paper presented an approach for estimating the subsurface thermal structures of the ocean from remote sensing data recorded at the sea surface, with the help of Argo in-situ data sets. The method was validated by the Argo STA data, and applied to the western mid-latitude North Atlantic with remote sensing SST and Altimetry data. A SOM Neural Network was trained using SSTA, SSHA and SSSA data from IPRC Argo gridded monthly sea surface data sets, and was then labeled with

52

Argo STA data. The labeled SOM maps, together with the SSTA, SSHA and SSSA, were then used to estimate the STA at different depths in the North Atlantic. The estimated STA maps and time series were then compared with Argo STAs, including independent data sets that were not used in the labeling processes.

Results showed that along the Gulf Stream Path, the SOM STA estimation has good performance from 30m to 700m depth, with a correlation coefficient lager than 0.8. The depths of and maximum correlation coefficient show a general agreement with the maximum STA variation in this area. The labeled SOM maps were used to estimate the STA with remote sensing SST and altimetry SSH data from January 1992 to December 2004. Sensitivity tests revealed the importance of SSS information, which can significantly improve the estimation in the subtropical ocean as much as 30%. In areas where the seasonal variation of SST and SSH is relatively large (such as high latitude subpolar basins, the Irminger Sea and the Labrador Sea), the monthly climatology SST and SSH can also help to improve the estimation by as much as 40%.

Chapter 3

GLOBAL SURFACE WARMING HIATUS: DECADAL VARIABILITY OF UPPER LAYER OHC IN THE INDIAN OCEAN

3.1   Introduction

Understanding the ocean's role in Earth's energy budget is fundamental to evaluate climate variability and change, including the rate of global warming and the recent 18-years' so-called Global Surface Warming Hiatus (GSWH) [Easterling and Wehner, 2009; Meehl et al., 2011; Kosaka & Xie, 2013]. This "hiatus" has caused confusion and debate within the scientific and policy spheres. However, it also offers an opportunity to study and improve our understanding of climate change dynamics. Previous studies show that the hiatus is related to external forcing changes [Solomon et al., 2010; Kaufmann et al., 2011], internal variability [England et al., 2014; Song and Colberg, 2011; Steinman et al., 2015] and heat redistribution within the climate system [Meehl et al., 2011; Song and Colberg, 2011; Levitus et al., 2012; Balmaseda et al., 2013a; Chen and Tung, 2014; Drijfhout et al., 2014]. Although an updated global surface temperature analysis by NOAA's scientists [Karl et al., 2015] suggests that the global trends are higher than reported by the IPCC [2013] and the decrease in the upward trend of global surface temperature since 1998 might have been amplified due to the possible artifacts of data biases, it is important we continue research to fully understand all the processes at work on this complex subject in a changing climate.

Ocean warming dominates the increase in energy stored in the climate system, accounting for about 93% of the energy accumulated between 1971 and 2010 and the

upper 700m layer contributing about 64% [IPCC, 2013]. Study of the spatio-temporal variability of the Ocean Heat Content (OHC) reveals the horizontal and vertical redistribution of heat in the global ocean and will improve our understanding of the processes and mechanisms how the ocean would respond to the changing climate and the role the ocean would play in the climate system. Tracking the missing heat during the GSWH, a recent work from Lee et al. [2015] revealed that while the Pacific Ocean absorbed extra heat during the global warming hiatus, more heat was transported to the Indian Ocean by the Indonesia throughflow (ITF), resulting in a decreasing trend of the Pacific Ocean heat content. They also found that the heat content increased abruptly in the Indian Ocean, accounting for more than 70% of the global ocean heat gain in the upper 700m during the past decade. This new finding sheds light on the GSWH research, and will exert a profound influence on the topic. Nieves et al. [2015] also found that the cooling in the top 100-meter layer of the Pacific Ocean was mainly compensated by warming in the 100- to 300-meter layer of the Indian and Pacific Oceans in the past decade since 2003, suggesting a decadal shift in Indo-pacific heating.

Such recent findings [Lee et al., 2015; Nieves et al., 2015] bring the Indian Ocean back to the platform of the GSWH study. Previous studies that focused on upper layer warming mainly concentrated on the role of the Pacific Ocean surface cooling [Kosaka & Xie, 2013; England et al., 2014] and the Atlantic Ocean surface warming [McGregor et al., 2014], while those studies that focused on the deep layer warming concentrated on the Atlantic Ocean and Southern Ocean [Meehl et al, 2011; Chen & Tung, 2014]. The GSWH is a global event by definition. The parable of the blind men and an elephant shall remind us that when dealing with a phenomenon on a

55

global scale, demarcating the global ocean or focusing only on certain regional variability will render merely a partial understanding of the subject. While Lee et al. [2015] and Nieves et al. [2015] focused on the recently two decades, what role the Indian Ocean have played in the global OHC redistribution in longer time scales? This question motivated us to analyze the OHC trend and spatial pattern in the Indian Ocean and global oceans.

3.2 Data and Method

Long time series data is needed to analyze the decadal variation of the OHC in the global Ocean and to cover both the global warming and hiatus period. We use the Ocean Reanalysis System (ORAS4) model/*in situ* reanalysis data from European Centre for Medium-Range Weather Forecasts (ECMWF) covering 1958-2009 [Balmaseda et al., 2013b], Simple Ocean Data Assimilation (SODA) reanalysis data V2.1.6 [Carton et al., 2000; Carton and Giese, 2008] covering 1958-2008, and the *in situ* WOD2013 data from National oceanographic data center (NODC), NOAA, covering 1955-2012 to analyze the OHC variation [Levitus *et al.*, 2012]. The ORAS4 reanalysis datasets show a clear and robust nonlinear trend in the 0–700m OHC, consistent with other observational estimates [Balmaseda et al., 2013b].

Causal analysis between OHC in Atlantic Ocean and OHC in the Southern Subtropical Indian Ocean is carried out following the method proposed by Liang [2014]. The causality is measured by information flow between two time series, e.g. X_1 and X_2. The rate of information flow [Liang, 2014] (units: nats per unit time) from the latter to the former is

$$T_{2 \to 1} = \frac{C_{11} C_{12} C_{2,d1} - C_{12}^2 C_{1,d1}}{C_{11}^2 C_{22} - C_{11} C_{12}^2} \tag{3.1}$$

where C_{ij} is the sample covariance between X_i and X_j, $C_{i,dj}$ is the covariance between X_i and the time differential approximation of X_j.

3.3 Ocean Heat Content Dynamic Equation

The dynamic equation governs OHC for a fixed depth layer in upper ocean can obtained from the divergent heat budget equation developed by Emery (1976). The terms in Eq. (1.11) were decomposed into climatology (denoted by an overbar) and anomaly (denoted by a prime) value, we assume the climatology terms cancel each other, then we have:

$$\frac{dT_a{}'}{dt} = \frac{Q'}{\rho C_p D} - \bar{v}_a{}' \cdot \nabla\left(\bar{T}_a + T_a{}'\right) + \left(\bar{w}_D + \bar{w}_D{}'\right)\left(T_a{}' - T_D{}'\right) + \left(\bar{T}_a - \bar{T}_D\right)w'_D \tag{3.2}$$

where the terms on right-hand side are similar as the terms of Eq. (1.17). The 4 terms of the right-hand side describe the effect of the following processes sequentially: anomalies in the net surface heat flux, heat advection by anomalous current, the anomalies in the temperature jump in the entrainment zone, and anomalies in the entrainment velocity.

3.4 Results

3.4.1 Decadal westward shift of the upper ocean OHC

The transport of warming water via ITF is from the Pacific Ocean to the Indian Ocean [Feng et al., 2011] while the Agulhas leakage transports warm and salty Indian Ocean water into the South Atlantic Ocean [Biastoch et al., 2009; Durgadoo et al.,2013; Le Bars et al., 2014], and both of the transport have large multi-decadal variation. According to the recent findings [Lee et al., 2011, 2015; Nieves et al., 2015],

we would expect a westward shifting of the OHC in the global ocean, especially in the southern hemisphere.

Zonal evolution of upper layer (0-300m) OHC was analyzed on southern hemisphere to see the whole image (Fig 3.1). We removed the inter-annual signal using a 10-year Hanning low-pass filter, so that the decadal and inter-decadal component of the OHC variations remained. We calculated the zonal anomaly of OHC by removing the zonal mean OHC so as to detrend the global warming. To include the Agulhas Return Current, the Agulhas retroflection area [Le Bars et al., 2014; Durgadoo et al., 2013] and the ITF, the latitude for OHC calculation ranges from 45°S to 10°N. The OHC variation in the Norhern Indian Ocean is found to be small compared to the Southern Indian Ocean (Levitus et al., 2012; Han et al., 2014). Figure 3.1 shows the results from WOD2013 and ORAS4 data. The zonal anomaly of OHC covers more than 50 longitudinal degrees and lasts more than 5-10 years, for both positive and negative phase. A westwards shifting of the OHC zonal anomaly was found in both data sets, with certain discontinuity and considerable different amplitudes given the different time resolution. The westward shifting of the OHC zonal anomaly has a period of about 30 years, a phase speed of about 1.8—2.5cm/s and takes about 50—70 years to travel from Eastern Pacific to Western Atlantic (Fig 3.1). Although the physical mechanisms for this westward propagation is not clear and still under investigation, the OHC zonal anomaly propagated from the Indian Ocean to the Atlantic Ocean in 1990s, which is about the same time for the basin wide warming of the Atlantic Ocean.

The westward shift of OHC is still evident without detrending of global warming (Fig 3.2b, Fig 3.2c) with the warming located in the Tropical Pacific in

58

1960s and in the Subtropical Pacific and Atlantic Ocean since late 1980s (Fig 3.2a). The detrended zonal OHC anomaly (Fig 3.1b, 3.1c) is two to three times of the magnitude of the zonal mean OHC (Fig 3.2d) in the upper layer. Figure 3.3 shows the westward shift of the decadal warming from the Indian Oceans to Southern Atlantic. The decadal warming in the Indian Ocean span from the late 1970s to early 1990s and located at 50-100°E and 20-40°S, the Southern Subtropical Indian Ocean (SSIO). So the decadal westward shift of OHC in the Indian Ocean located in SSIO.
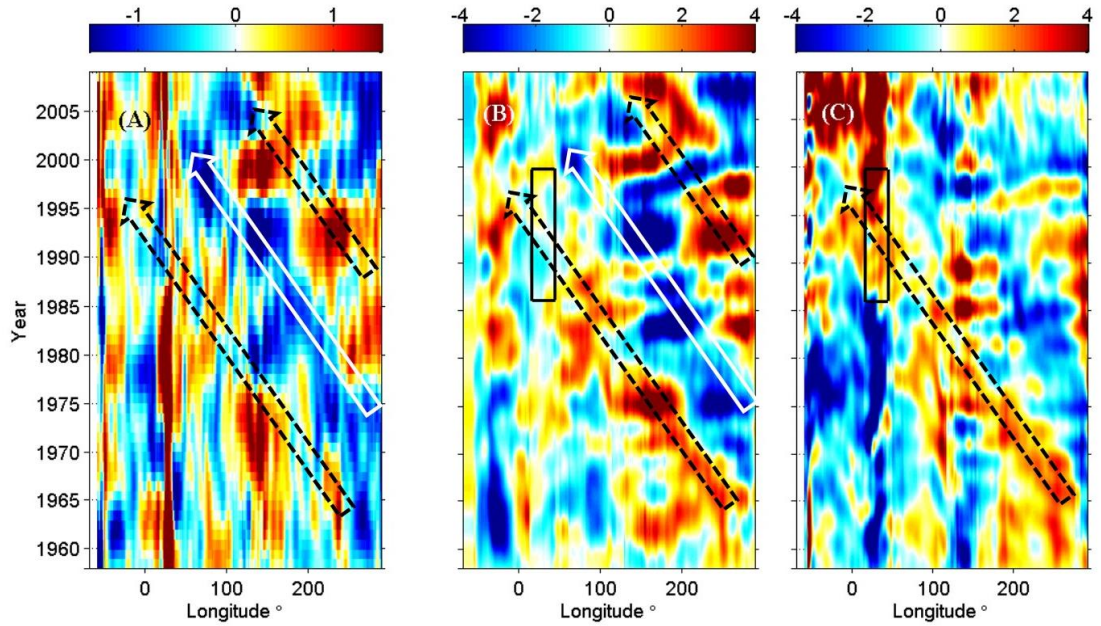
Fig. 3.1 Time evolution of the zonal OHC anomaly 1958—2009, in 10^{18} Joules. For the upper layer (0-300m), derived from (A) WOD 2013 *in situ* data, and (B) ORAS4 model/*in situ* reanalysis data and (C) for the deeper layer (300-700m, ORAS4 model/*in situ* reanalysis data). The ocean heat content was smoothed with a 10-year Hanning low-pass filter and averaged from 45°S to 10°N, and normalized to the zonal mean OHC. The arrows show one of the westward propagation of the warming (Black) and cooling (white) OHC anomalies. Solid rectangle shows the warming of the deeper layer in the Agulhas Current system during 1985-2000.
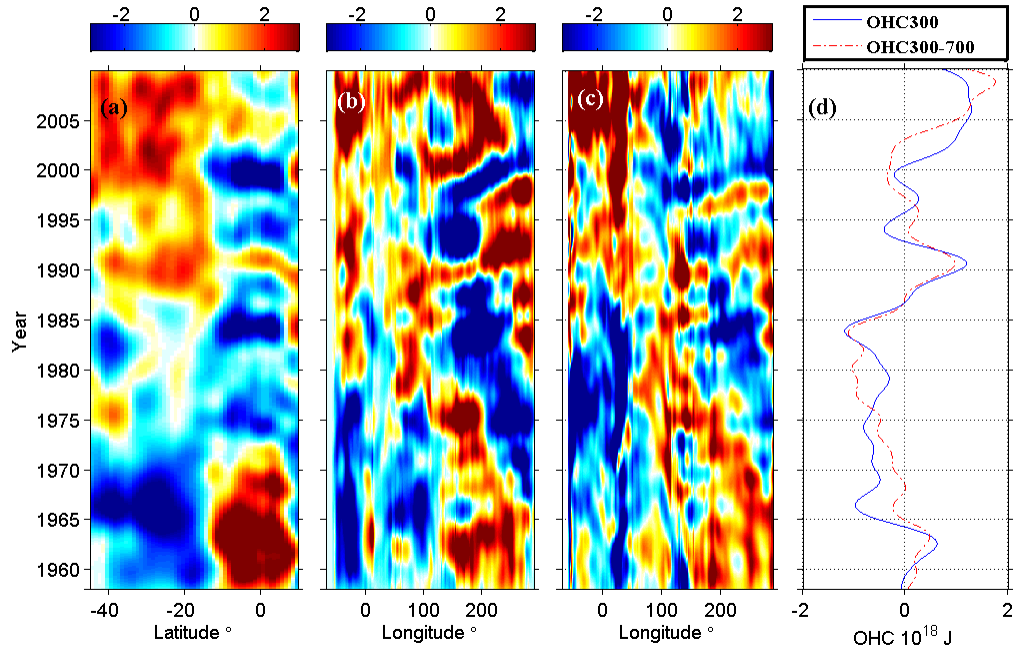
Fig. 3.2 Time evolution of the OHC in the Southern Hemisphere1958—2009, in 10^{18} Joules. For (a) Latitudinal, and (b) Longitudinal evolution of the upper layer (0-300m) OHC, (c) Longitudinal evolution of the deeper layer (300-700m) OHC, and (d) time series of zonal mean OHC. The OHC was smoothed with a 10-year Hanning low-pass filter and averaged from 45 °S to 10 °N.
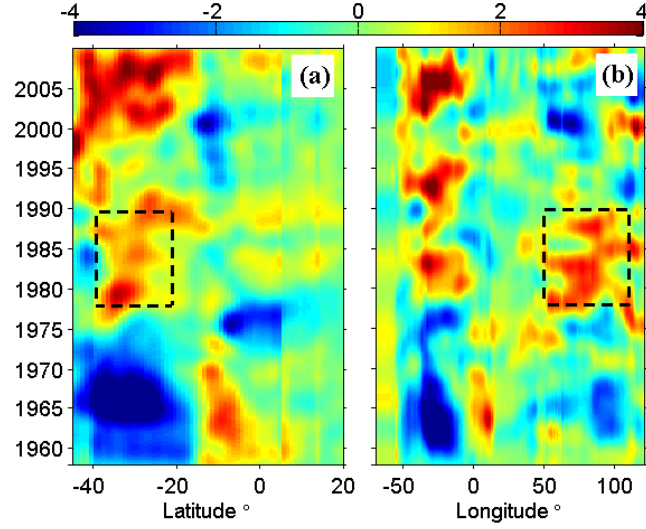
Fig. 3.3 Time evolution of the (a) latitude and (b) longitude of the OHC anomaly 1958—2009, in 10^{18} Joules, for the Southern Atlantic and Indian Oceans. Thick dash boxes indicate the warming OHC in the Southern Subtropical Indian Ocean.

3.4.2 Variation of upper layer OHC in the Southern Subtropical Indian Ocean

The warming in the Tropical Indian Ocean has a complex vertical structure with warming in the surface layer and a multi-decadal cooling in the subsurface since 1960s (Han et al., 2006). This phenomenon significantly exceeded the cross-data (Han et al., 2006; Barnett et al., 2005; Pierce et al., 2006) and cross-model uncertainty (Trenary & Han, 2008). This mainly was caused by the enhanced Ekman pumping velocity, which induced a southward Ekman transport increase of about 0.5 Sv/decade and a strengthened Southern subtropical cell (Trenary & Han, 2008). While the previous research mainly focused on the mechanism for cooling in the tropical subsurface, we focus on the warming in the southern subtropical cell. The southern subtropical cell, the warm pole of this persistent mode of warming with meridional dipole which is sustained by intensified meridional Ekman transport since the 1960s

61

(Schott et al, 2009), supplies sufficient heat to the source area of the Agulhas Current (Fig 3A). Although about two thirds of the volume flux of the Agulhas Current is recirculated from the Southwest Indian Ocean sub-gyre (Lutjeharms, 2006), this part does not contribute much to the heat flux and warming. The major heat source for the Agulhas Current comes from east of Madagascar and Mozambique Channel (Lutjeharms, 2006; Beal et al.,2006; Lutjeharms & Van Ballegooyen, 1988).

The warming pattern in the Southern Subtropical Indian Ocean cell (Fig 3A) shows the warming path from East Madagascar Current to the Agulhas, or via the north end of Madagascar and heading southward through Mozambique Channel, indicating that the warming in the subtropical cell sustains the steady strength and warming of the Agulhas Current in the past century. Warm waters from the Tropical Pacific via Indonesian Throughflow (ITF) coming to the Indian Ocean at 10-15°S (Fig 2B) contributes to the meridional dipole up to the subduction zone (Schott et al., 2009; Song et al., 2004; Le Bars et al., 2013; Sprintall et al., 2014).

The time series of the warming in the upper layer shows that the Indian Ocean warmed up since middle 1960s with strong warming in the Subtropical Cell of the Indian Ocean (STCIO) and the Southern Atlantic Ocean followed up with a time lag of about 10 years (Fig 3.5C, 5E, 5F). Causal analysis (Wu et al, 2012) was carried out to identify the importance of the warming in the STCIO. Fig 2.4A shows the information flow from STCIO to the Atlantic ($T_{STCIO \rightarrow Atlantic}$). The patterns indicate that the STCIO warming contributed to the warming in Southern Subtropical Atlantic, through the pathway of Agulhas Current and Agulhas leakage. The significant pattern in low latitude Atlantic indicates that heat anomaly signal in STCIO will cause the heat variation in the tropical Atlantic. The information flow from Atlantic to the

STCIO ($T_{Atlantic \to STCIO}$) shows major pattern located in the western subtropical Atlantic which is part of the supergyre. This pattern is relatively weak (Fig 3.5B), indicating dominant influence from STCIO to the Atlantic Ocean. The Agulhas current and leakage link the Indian Ocean and the Atlantic Ocean. Its response to a warming climate provides physical explanations to the results of causal analysis. Using ORAS4 data, the Indian Ocean OHC mainly shows flattened surface layer heat content since late 1970s with large inter-annual variation, consistent with the time series from WOD2013 data (Fig 3.4). At deeper depths it varies on the decadal scale with a significant warming occurring as early as 1998 (Fig 3.4), almost at the same time as the beginning of the current global surface warming hiatus. This indicates that the Indian Ocean might have played a more important role in the global surface warming hiatus than expected before.

On a global scale, the change of OHC shows major patterns located in the Tropical Pacific and North Atlantic. The upper layer is dominated by the ENSO inter-annual variability (Fig 3.5a) in the tropical Pacific and by the east cold tongue and west warm pool pattern with strong inter-annual variability and weak decadal variability. The Principle component (PC) of the second mode of the upper layer and the first mode of the middle layer has the same trend: increasing since the early 1960s and maintaining a flat trend after the middle 1980s. The PCs for deep OHC variation has strong decadal variability and weak inter-annual variability (Fig 3.5g, S2h). The analysis from other datasets [Chen & Tung, 2014; Ishii & Kimoto, 2009] also shows strong warming in the Agulhas Current system and the Southern Subtropic Atlantic Ocean in the 300-1500 m layer during current hiatus.

To understand the mechanism underlying this warming, we need to take a closer look at the OHC variation in the Indian Ocean and the South Atlantic Ocean. The same analysis (EOF) was carried out in this area. The dominant patterns for the upper layer and deeper layer in the Indian Ocean and the South Atlantic Ocean (Fig 3.6a, 3.6e) are actually the same as the second EOF mode for global pattern (Fig 3.5b, S2f). At middle and deep layer, the leading modes in the Indian Ocean, South Atlantic and adjacent Southern Ocean (Fig 3.6a, 3.6c, 3.6e), showed a persistent warming trend since middle of 1960s and last until 2010, showing no sign of warming hiatus before 2007 (red and black lines in Fig 3.6g), which is very likely to be related to the global warming from increased greenhouse gases. However, in the upper layer the warming trend has stopped and a meridional dipole mode (Fig 3.6a) has maintained since the late 1970s (blue line in Fig 3.6g), and slightly increased after late 1990s, same as the trend of OHC in the surface layer (Fig 3). The leading EOF mode in the *in-situ* WOD2013 (Fig 3.7) and SODA (Fig 3.8) reanalysis data also showed the meridional dipole in tropical and subtropical Indian Ocean.
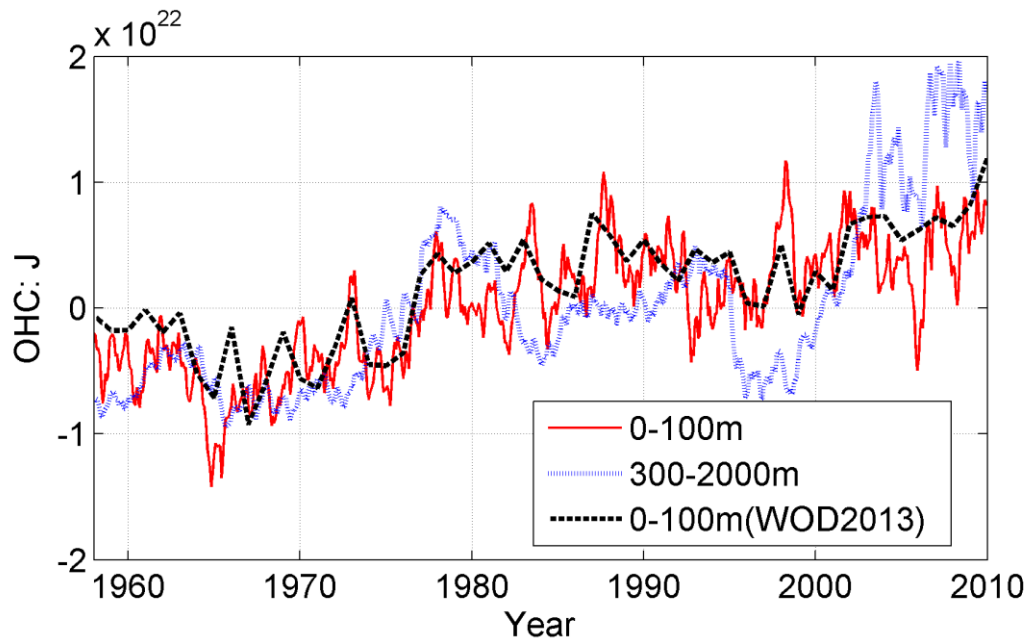
Fig. 3.4 Time series of the Indian Ocean heat content. Surface layers: 0-100 m, and deeper layers: 300-2000 m (red and blue line calculated from ORAS4 data, black dash line from WOD2013 data. The south boundary of the Indian Ocean Basin defined as 50°S, as defined in the WOD2009:
http://www.nodc.noaa.gov/OC5/WOD09/wod_masks.html)
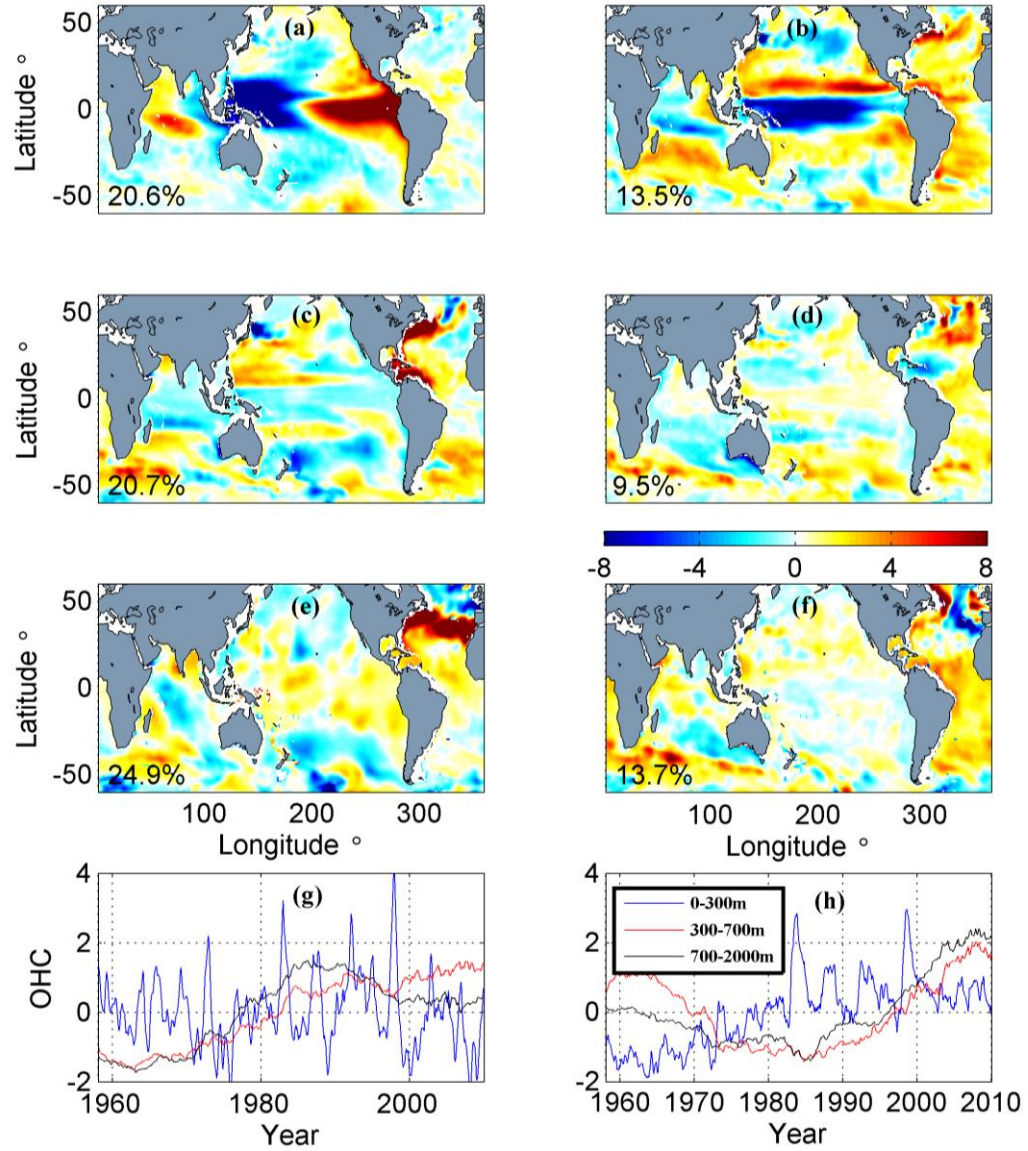
Fig. 3.5 EOF of the global ocean heat content. The first (left column) and second (right column) modes of the OHC in the layers 0-300 m (a, b), 300-700 m (c, d) and 700-2000 m (e, f), respectively, in the same unit of 10^{18} Joules. The Principle component time series associated with each EOF modes (g, h), blue for the upper layer, red for the middle layer and black for the deep layer (see METHODS for detailed mapping information).

The warming in the Tropical Indian Ocean has a complex vertical structure with warming in the surface layer and a multi-decadal cooling in the subsurface since

1960s [Han et al., 2006]. This phenomenon significantly exceeded the cross-data and cross-model uncertainty [Barnett et al., 2005; Han et al., 2006; Pierce et al., 2006, Trenary and Han, 2008]. This mainly was caused by the enhanced Ekman pumping velocity, which induced a southward Ekman transport increase of about 0.5 Sv/decade and a strengthened southern subtropical cell [Trenary and Han, 2008]. While the previous research mainly focused on the mechanism for cooling in the tropical subsurface, we focus on the warming in the SSIO. The southern subtropical cell, the warm pole of this persistent mode of warming with meridional dipole, which is sustained by intensified meridional Ekman transport since the 1960s [Schott et al., 2009], supplies sufficient heat to the source area of the Agulhas Current (Fig 3.6a). The major heat source for the Agulhas Current comes from east of Madagascar and Mozambique Channel [Lutjeharms & Van Ballegooyen 1998; Lutjeharms, 2006; Beal et al., 2006].

The warming pattern in the Southern Subtropical Indian Ocean cell (Fig 3.6a) shows the warming path from East Madagascar Current to the Agulhas, or via the north end of Madagascar and heading southward through Mozambique Channel, indicating that the warming in the subtropical cell sustains the steady strength and warming of the Agulhas Current in the past century. Warm waters from the Tropical Pacific via ITF coming to the Indian Ocean at 10-15°S (Fig 3.5b) contributes to the meridional dipole up to the subduction zone [Schott et al., 2009; Song et al., 2004; Le Bars et al., 2013].
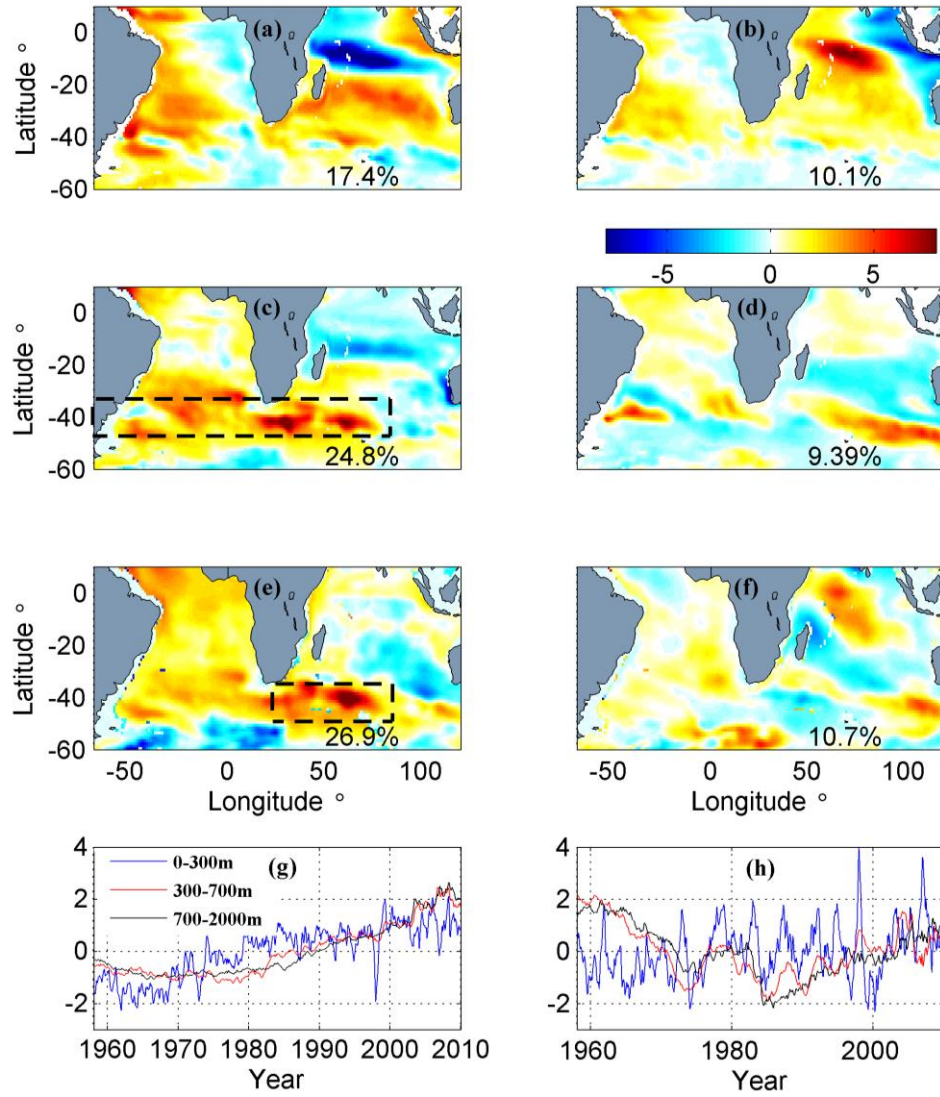
Fig. 3.6 EOF of the ocean heat content for the Indian Ocean and the Southern Atlantic Ocean. The first (left column) and second (right column) modes of the OHC in the layers 0-300 m (a, b), 300-700 m (c, d) and 700-2000 m (e, f), respectively, in the same unit of 10^{18} Joules. The Principle component time series associated with each EOF modes (g, h), blue for the upper layer, red for the middle layer and black for the deep layer (see METHODS for detailed mapping information). The dash box in c and e indicate the location for heat content calculation in Fig 3.7.
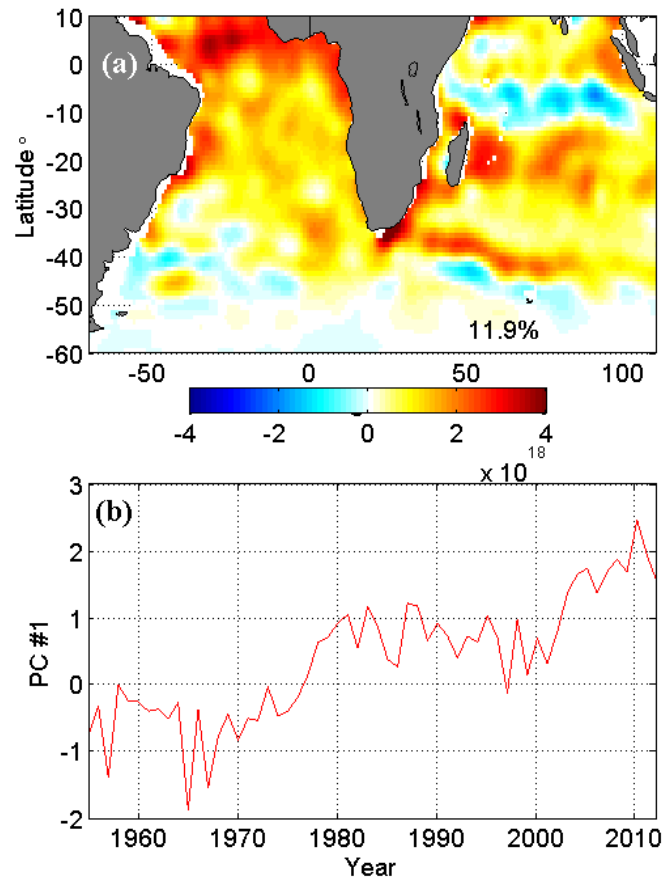
Fig. 3.7 EOF of the ocean heat content. EOF Mode 1 (a) and PC 1 (b) of OHC of 0-300 m in Indian Ocean and the Southern Atlantic from WOD13 data (see METHODS for detailed mapping information). First 4 modes explained 31.2% of the variance.
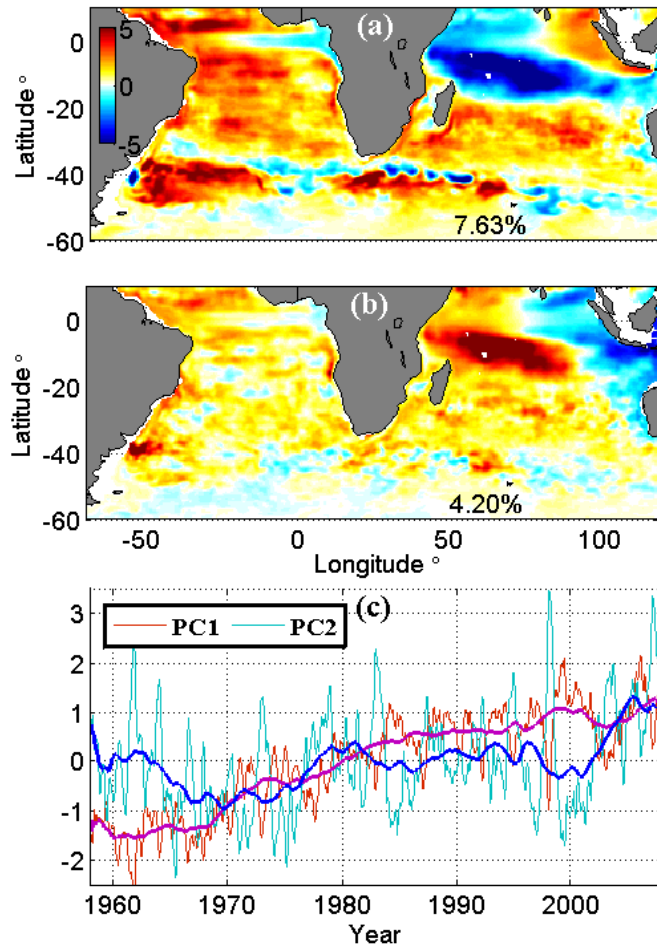
Fig. 3.8 EOF of the upper layer OHC for the Indian Ocean and the Southern Atlantic Ocean. The first (a) and second (b) modes of the OHC in the layers 0-300 m in the same unit of 10^{18} Joules. The Principle component time series associated with each EOF modes (c), red for the first mode, blue for the second mode, thick line denotes a 5-year running mean.

3.4.3 Decadal vertical OHC redistribution to the deeper layer

During the global surface warming hiatus, the redistribution of heat to the deeper layer contributed to the slowdown of the surface warming. Most of the energy from the imbalance at the top of atmosphere went to the Atlantic and the Southern

Oceans [Levitus et al., 2012; Chen & Tung, 2014]. The EOF analysis of the OHC in the global ocean shows significant warming in the Southern ocean at middle and deep layer (Fig 3.5d and Fig 3.5f), located near the Subtropical Fronts. The temporal evolution of the warming in the Southern Ocean is characterized with three 'quasi-steady' processes with two distinct regime shifts in the 1970s and the late 1990s (Fig 3.9a and Fig 3.9b): 1958-1975, the warming is between 50°S-60°S; 1978-1998, the warming is located in the Ross Sea Gyre (60°S -70°S); 1998-2009, the warming is strong and mainly located between 40°S -50°S, where subtropical fronts interacts with western boundary current (WBC) extensions. The warming at middle layer begins around the middle 1960s, and after middle 1990s the enhanced warming was first excited at the Agulhas Current system (Fig 3.9c) and the subsurface temperature anomaly propagated eastward. The longitudinal warming was more evenly distributed, and the subtropical supergyre (70°W -80°E, 50°S -35°S) contributed 40%-60% of the middle layer warming in the Southern Ocean during hiatus period (Fig 3.9a, Fig 3.9e). The strong warming in the deep layer began in middle 1990s and took place mainly in Agulhas Current System (20°E-80°E, 50°S-35°S), which contributed about half (40%-60% for 2000-2009) of the warming in deeper layer (Fig 3.9f). The location of the warming indicates the interaction of WBCs, Subtropical Front and the Subantarctic Front.

In the southern Atlantic Ocean, the OHC in upper layer is characterized with a warming western boundary and extension areas, as well as cooling on the eastern coast (Fig 3.6a). However, in the middle and deep layer, the warming is a basin wide phenomenon, without gap between two ocean basins at the south end of the African continents (Fig 3.6c, 3.6e). The subtropical gyre in the South Atlantic Ocean together

with the Agulhas Current and the Agulhas Retroflection area, which was called the supergyre in the Southern Atlantic and Indian Ocean [Speich et al., 2007], has the same warming trend since the 1960s, with more significant warming since early 1980s (Fig 3.6g, Fig 3.9e). The Indian Ocean warmed up since middle 1960s with strong warming in SSIO and the Southern Atlantic Ocean followed up with a time lag of about 10 years (Fig 3.9c, 3.9e, 3.9f). In the early 1980s, warming in the Agulhas Current was enhanced synchronously with significant warming of the middle and deeper layer in the subtropical supergyre, indicating that the Agulhas leakage has increased since 1980s. This is consistent with previous findings from numerical, historical measurements, and satellite altimetry studies [Rouault et al., 2009; Dong et al., 2011; Biastoch et al., 2009, 2013; Durgadoo et al., 2013].

3.5   Discussion

We detected westward shift of OHC from *in-situ* WOD2013 data and model/*in-situ* ORAS4 reanalysis data (Fig 3.1) with certain discontinuity and considerable difference in amplitudes given the different time resolutions. It has a period of about 30 years, and takes about 60 years to travel from the eastern Pacific to the western Atlantic, almost the same as the period of the GSWH [Meehl et al., 2011]. This result confirms that the western shifting warm water from the Pacific Ocean to Indian Ocean in 1970s to 1980s is similar to that in last decade as reported by Lee *et al.* [2015] and Nieves et al. [2015]. This wave-like OHC propagation suggests the decadal zonal and meridional shift of warming center in the upper ocean, which in return will change the SST in decadal time scale. This may shed light on the physical mechanisms for the multi-decadal climate variability such as AMO and PDO.

The global surface warming hiatus is a global event by definition. Based on the analysis above, we find the missing link in the Indian Ocean for the GSWH. In light of this finding, we note that the global ocean and atmosphere form a positive-feedback loop, consistent with many previous studies that focus ocean basin scale phenomenon (Fig 3.11). Heat from the Pacific and Indian Oceans follow the surface pathways of the thermohaline circulations to the Atlantic Ocean via ITF and Agulhas leakage, and contributed to the enhanced basin wide warming in the Atlantic Ocean [Lee et al., 2011; Rühs et al., 2013]. Previous studies have shown that basin-wide warming in the Atlantic [McGregor et al., 2014] and Indian Oceans [Luo et al., 2012] intensified trade wind and wind-driven circulation since late 1990s, resulting in surface cooling in the eastern Pacific, which is one of the contributor to the current GSWH [Kosaka & Xie, 2013; England et al., 2014], and the rapid sea-level rise in the Western Pacific, which would result in a strengthened ITF [Lee et al., 2015; Feng et al., 2011]. This positive-feedback of ocean and atmosphere interaction might ended in a strengthened trade wind and wind-driven circulation in a warming climate in the long run, other than the already intensified Antarctic Circumpolar Current, as suggested in Toggweiler & Russell [2008].

Indian Ocean heated up consistently and notably since the late 1970s due to a positive feedback mechanism [Roxy et al, 2014], with a strong warming in the southern subtropical cell since middle of 1960s (Fig 3.4c), due to the meridional dipole pattern in the upper layer OHC. The upper layer OHC in Indian Ocean reached a saturated equilibration and has been in "hiatus" since early 1980s. The Agulhas Current system has warmed (Fig 3.4d) and strengthened since early 1980s [Biastoch et

al., 2009; Rouault et al; 2009; Dong et al, 2011; Durgadoo et al., 2013]. Indian Ocean contributed to the GSWH from following two aspects.

On one side, the Indian Ocean is an accelerator to build up heat in the SSIO and supply heat to the Atlantic Ocean and contributed to the onset of basin-wide warming up in the Atlantic [Lee et al., 2011; Rühs et al., 2013], which triggers the global surface warming hiatus [McGregor et al., 2014]. To identify the importance of the warming in the SSIO, causal analysis [Liang, 2014] was carried out between the time series of the OHC in upper layer of SSIO and the Southern Atlantic Ocean. Figure 3.10a shows the information flow from SSIO to the Atlantic ($T_{SSIO \rightarrow Atlantic}$). The patterns indicate that the SSIO warming contributed to the warming in Southern Subtropical Atlantic, through the pathway of Agulhas Current and Agulhas leakage. The significant pattern in low latitude Atlantic indicates that heat anomaly signal in SSIO will cause the heat variation in the tropical Atlantic. The information flow from Atlantic to the SSIO ($T_{Atlantic \rightarrow SSIO}$) shows major pattern located in the western subtropical Atlantic which is part of the supergyre. This pattern is relatively weak (Fig 3.10b), indicating dominant influence from SSIO to the Atlantic Ocean. The results of causal analysis imply that the OHC perturbation travels from Indian Ocean westward to the Southern Atlantic since 1950s, which is in consistent with Lee et al. [2011]. The Agulhas current and leakage link the Indian Ocean and the Atlantic Ocean. Its response to a warming climate provides physical explanations to the results of causal analysis.

On the other side, the increased Agulhas leakage contributed to the salinification in the Southern Atlantic [Biastoch & Böning, 2013], the intensified Southern Hemisphere subtropical supergyre [Beal et al., 2011; Speich et al., 2007] and

distribution of heat to deeper layer. Whether the ocean current system can distribute the extra heat to the deeper ocean or not will be vital for future atmosphere temperature change [Toggweiler & Russell, 2008]. The vertical OHC redistribution during the OHC westwards shifting is very important. Analogous to the dynamics analysis for temperature anomaly in the mixed layer [Frankignoul, 1985] and for upper ocean[Emery, 1976; Moisan & Niiler, 1998], the terms controls the OHC vertical redistribution mainly include anomalies of thermocline depth due to trade wind variation, and other mixing related to this depth variation. Both upper layer and deeper layer show similar patterns for the OHC variation, suggesting the averaged warming depth is larger than 300m, and the depth varies synchronously with the OHC (Fig 3.1b, 3.1c). In the Agulhas Current area during 1985—2000 (black solid rectangle in Fig 3.1b and 3.1c) and Southern Atlantic Ocean after 2000 (top left corner of Fig 3.1c), warming is very significant in the deeper layer while not so significant in the upper layer, suggesting the deeper layer warming and a large amount of heat transported into the middle and the deeper layer during the westwards propagation of the OHC and Agulhas Current system plays very important role in this vertical OHC redistribution. The physical mechanism for this is related to the increased inter-basin heat and salt exchange by Agulhas leakage [Biastoch et al., 2009; Rouault et al; 2009; Dong et al, 2011; Durgadoo et al., 2013] and intensified southern subtropical supergyre [Beal et al., 2011; Speich et al., 2007]. This further induced a large amount of heat sequestration to the middle and deeper layers in the Southern Atlantic Ocean and the Southern Ocean, contributing to the current global surface warming hiatus.

3.6 Summary

The OHC was used as a tracer to study the decadal heat horizontal and vertical redistribution in the global ocean under a warming climate. Decadal westward shift of the OHC in the southern hemisphere ocean was detected using from in-situ WOD2013 data and model/in-situ ORAS4 reanalysis data. It has a period of about 30 years, and takes about 60 years to travel from the eastern Pacific to the western Atlantic, almost the same as the period of the GSWH. The magnitude of the shifting OHC anomaly is two to three time stronger than that of global warming trend in the southern hemisphere ocean. The OHC anomaly shows zonal and meridional shifting on decadal to inter-decadal time scale. This may have strong implication in the multi-decadal climate variability.

The Southern Subtropical Indian Ocean plays very important role in this OHC shifting. The redistribution of the OHC in upper layer follows the surface branch of the Global Ocean Conveyor belt to travel westward from the Pacific to the Atlantic via the Southern Subtropical Indian Ocean. Heat was distributed to deeper layer of subtropical supergyre during the westward shift via the Agulhas Current system, contributing to the global surface warming hiatus.This paper summarizes all the known mechanisms on wind and wind-driven circulation that related to the GSWH, and identifies the previously neglected Indian Ocean as one of the important contributors to the current hiatus through its meridional dipole mode and the Agulhas Current system. With an embedded atmospheric bridge linking the Atlantic SST with the Pacific trade winds, the global ocean and atmosphere forms a closed positive feedback loop. This finding explains not only the occurrence of global warming hiatus, but also sheds light on the understanding of the multi-decadal climate variability.
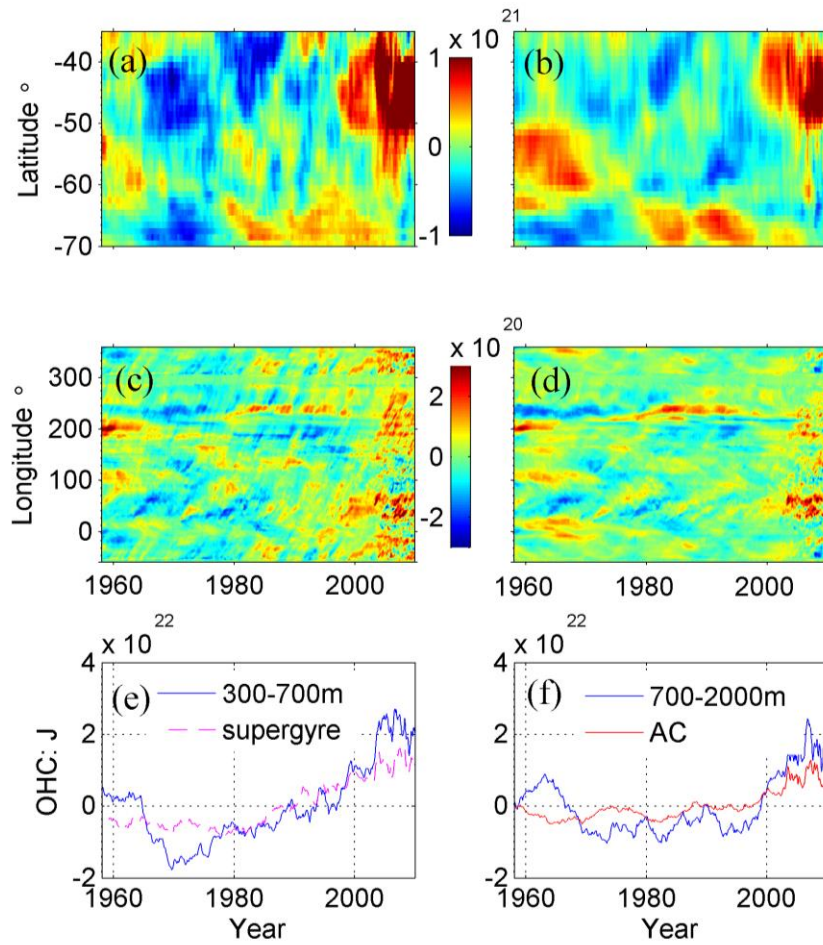
Fig. 3.9 OHC variation in the Southern Ocean. The latitudinal (a,b), longitudinal (c,d) distribution and time series (e, f) of the OHC in the layers 300-700 m (left column) and 700-2000 m (right column), respectively, in the same unit of Joules. In e and f, the blue line shows the OHC in the Southern Ocean (defined as ocean south to 35 ˚S here), the red line shows the OHC of 700-2000 m layer in the Agulhas Current (AC) System (20 ˚E -80 ˚E, 50 ˚S -35 ˚S, as shown the dash box in Fig 3.6e), the magenta dash line shows the time series for OHC of 300-700 m layer in the supergyre connecting the south Atlantic and the Indian Ocean (70 ˚W -80 ˚E, 50 ˚S -35 ˚S, as shown the dash box in Fig 3.6c).
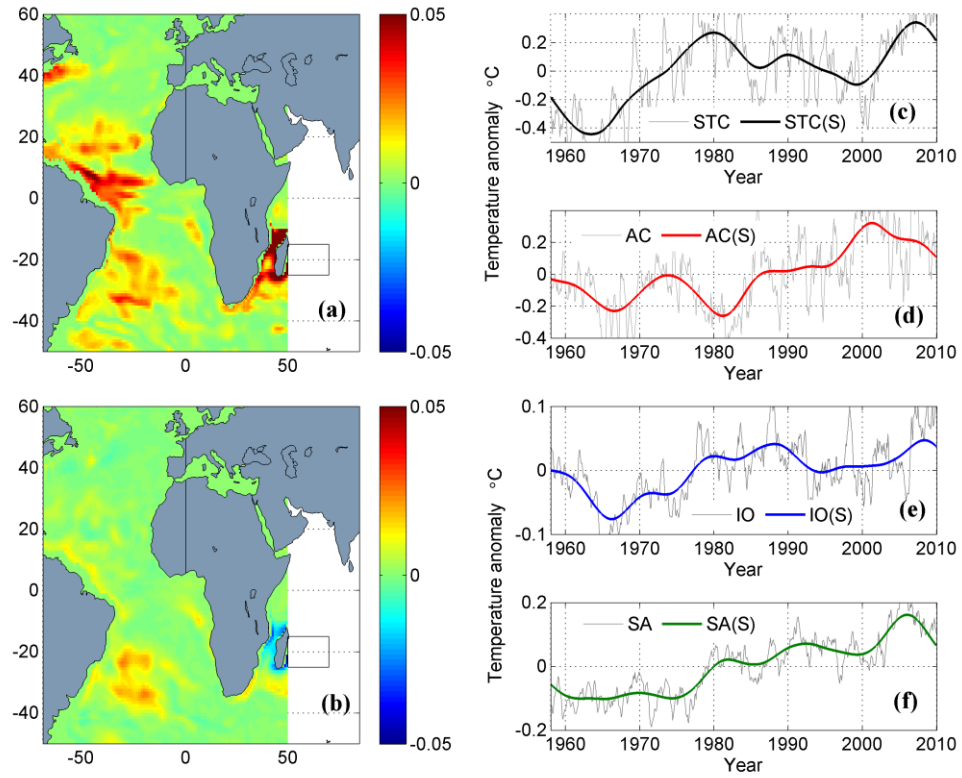
Fig. 3.10 Causal analysis and time series of the warming in the upper layer (0-300m). (a) $T_{STC \to Atlantic}$, Information flow from the averaged OHC of the Southern Subtropical Cell (STC, shown as the black box) in the Indian Ocean to the OHC of the Atlantic Ocean. (b) $T_{Atlantic \to STC}$, Information flow from the Atlantic Ocean to the averaged OHC of STC in the Indian Ocean (see METHODS for detailed mapping information). Time series of the warming OHC in the upper layer of (c) STC (averaged over 50°-70°E and 25°S-15°S); (d) Agulhas Current (AC, averaged over 20°-60°E and 45°S-35°S); (e) Indian Ocean mean (IO, averaged over 20°-110°E and 50°S-20°N); (f) Southern Atlantic mean (SA, averaged over 58°W-20°E and 50°S-10°N).

78
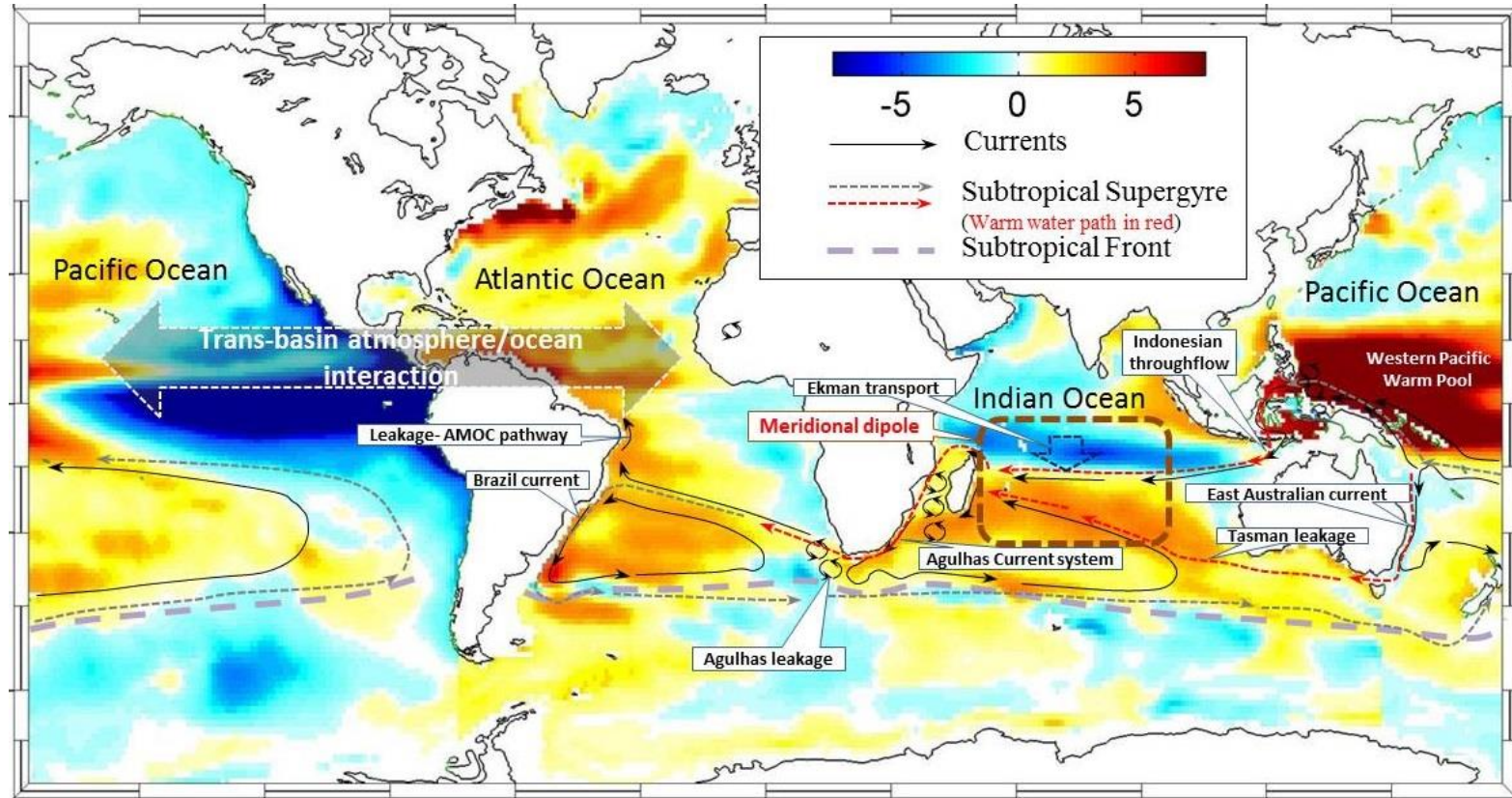
Fig. 3.11 Schematic figure for Indian Ocean as an Accelerator to the Global Surface Warming Hiatus. Background colors show the first mode from the EOF analysis of the upper layer (0-300m) in different basin (Composite from analysis in the Pacific Ocean Basin and the Atlantic-Indian Ocean Basin), in the unit of 10^{18} Joules. The subtropical supergyre is adopted from Beal[16] *et al.* (2011) and Speich *et al.* (2007). Red dash lines and arrows show the path way for warm water (heat content anomaly) from the Western Pacific Warm Pool to the Indian Ocean via ITF and Tasman Leakage, and from the Indian Ocean to the Atlantic Ocean via Agulhas Leakage (see METHODS for detailed mapping information).

Chapter 4

DECADAL VARIATION OF OCEAN HEAT CONTENT IN WESTERN NORTH PACIFIC

4.1 Introduction

The global warming hiatus since the beginning of this century has raised large concerns around the world. There are 2 major groups of point of view for mechanisms for the slowing down of increase of global surface temperature: the external forcing and the internal variation of the climate system. The keep-rising greenhouse gas monitored at Hawaii Island indicates that the energy unbalance at the top of atmosphere is very likely to keep its pace. The energy trapped in the climate system increase steadily. The Pacific plays an important role in global warming hiatus, (Kosaka & Xie, 2013, England et al, 2014) the frequent occurrence of the La Nina and intensified east trade wind helps the development of the cold tongue in the east Tropical Pacific. The hiatus is found to be related to the negative phase of PDO (Trenberth & Fasullo, 2013). On the other hand, the warming of the deep ocean is believed to be one of the mechanisms for the decadal internal variation. During the hiatus period, the heat up-take of the subsurface and deep ocean is much more significant than other decades (Meehl et al, 2011). The wind driven meridional overturning circulation between the tropical and subtropical oceans slowed down from 1970's to 1990's, causing a decrease of 25% of the upwelling the equatorial ocean and hence a rise in the equatorial sea surface temperature (McPhaden and Zhang, 2002). However from 1990's to the beginning of 2010's, the increased subsurface ocean heat

uptake, which was induced by the increased subduction of the shallow overturning cell, slowdowns the warming of the surface layer in tropical Pacific (England et al, 2014).

The redistribution of the heat in the ocean between the surface and subsurface layers has an ENSO like temporal pattern, the changes in the east-west tilting of the equatorial Pacific thermocline is the major reason (Roemmich and Gilson, 2011). In 1990's the surface warming of tropical Indian ocean and Pacific accompanied a strong cooling in the upper thermocline, while during the hiatus period, the surface cooling of east equatorial pacific ocean accompanied by the increased subsurface ocean heat uptake (Han et al, 2006; Trenary and Han, 2008; England et al, 2014). Is this decadal pattern variation of heat redistribution in the Pacific Ocean related to the PDO? And to what depth this redistribution exists? To answer these questions, the OHC to different depth from reanalysis data (ORAS4) and in-situ measurements (WOD) data sets were analyzed in the next section; the results were presented in section 4.3.

4.2   Data and Methods

To analyze the decadal variation of the Ocean Heat Content (OHC) in Pacific Ocean, long time series data is needed. ORAS4 reanalysis data sets [Balmaseda et al., 2013b], a new operational ocean reanalysis system that has been implemented at European Centre for Medium-Range Weather Forecasts (ECMWF) based on Nucleus for European Modeling of the Ocean (NEMO) V3.0, provide monthly data from 1958 to 2009, covering the global warming and hiatus period. Wind field data is the 20th Century Reanalysis V2 data, provided by the NOAA/OAR/ESRL PSD, Boulder, Colorado, USA, from their Web site at http://www.esrl.noaa.gov/psd/. Global surface temperature were from HadCRUT4 [Morice *et al.*, 2012], a collaborative product of the Met Office Hadley Centre and the Climatic Research Unit at the University of East

Anglia, and NOAA Global Surface Temperature (GST) is provided by NOAA National Climatic Data Center [Jones et al., 1999; Smith et al., 2008], and available online via (http://www.ncdc.noaa.gov).

The spatial and temporal variation of dynamic and thermodynamics conditions, including OHC and wind field (see "Data summary" section in Supplementary online material for detailed information), was analyzed by Empirical Orthogonal Function (EOF) analysis. Global surface temperature time series were decomposed using the Ensemble Empirical Mode Decomposition (EEMD) [Wu & Huang, 2009], to find the decadal and multi-decadal variation.

4.3   Decadal OHC Variation

4.3.1   Decadal OHC variation(WOD2013) and connection between subtropical and tropical Pacific

The decadal change of OHC in Pacific is analyzed from WOD2013, annual mean temperature anomaly data. The variation in the western pacific basin dominant the whole basin decadal changes (Fig 1). The warming in the recent decade is mainly took place in the upper 400-500m, located in the tropical and subtropical western Pacific basin, while there is cooling in the eastern Pacific at all latitudes, showing the necessary of focus in western pacific to study the warming of subsurface tropical Pacific.

In the 1980~1990s, the decadal change present the pattern of the warming of upper layer and cooling in the upper thermocline, due to the increased downward surface heat fluxes from increased GHGs and upward Ekman pumping velocity and shoaling of the thermocline due to anomalous winds in the tropics (Han et al, 2006).

82

At 35~45 N, the strong cooling in 1970~1980s and warming in 1980s~1990s indicates the variation of Kuroshio Extensions.
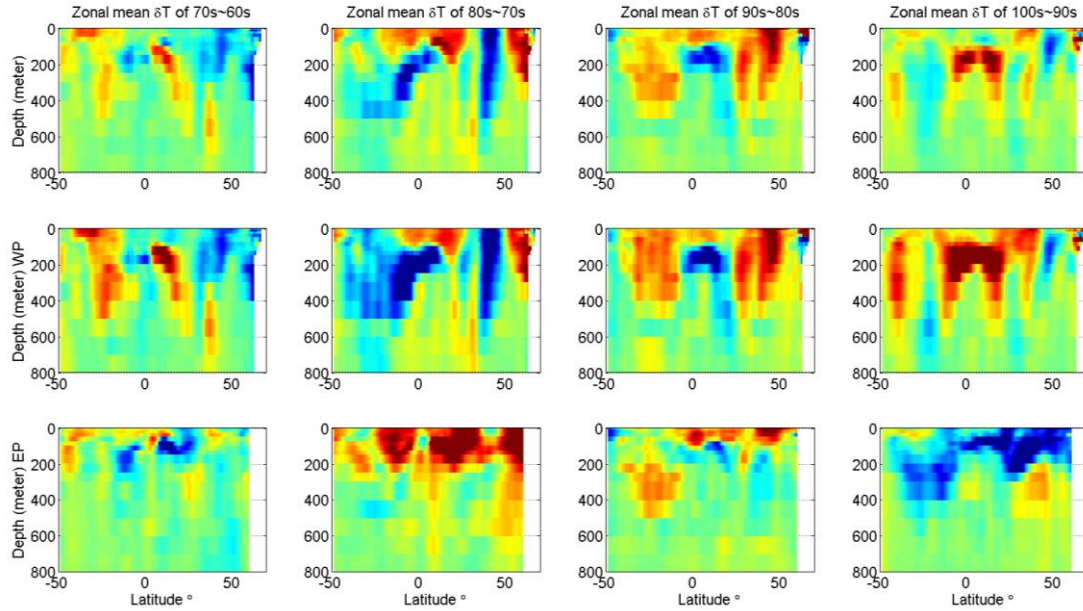
Fig. 4.1 WOD2013 zonal mean decadal temperature trend in the Pacific Ocean. Upper: whole basin; middle, Western Basin (120E~160W); bottom: Eastern Basin (160W~60W).

4.3.2 Inter-Annual variation of heat content in Upper Tropical Pacific

The time series of heat content in Tropical Pacific (Southern ocean not included) from surface to subsurface or deeper were calculated using ORAS4 reanalysis data as 6 layers in the tropical Pacific (20S-30N): 100m, 200m, 300m, 500m, 700m and 2000m. From reanalysis data, the ENSO related heat vertical redistribution is found to have taken place through late 1950's to 2010 (Fig 2a). Argo documented the ENSO related heat redistribution between surface (0-100m) and subsurface (100-500m) before the 2009 La Nina (Roemmich and Gilson, 2011). However，before 2000，the heat content redistribution between surface(0-100m) and

subsurface(100 to 500m) shows different trends and the synchronism of OHC variations are inconsistent, including magnitudes and phase lag and leading of the OHC variation (Fig 2a). This indicates that the exchange of heat on the vertical dimension may have happened at different depth, and 100m might be not the best to represent the boundary between surface and subsurface layer of the tropical ocean.

Results show that the OHC in the 100-200m plays an important role in the annual variation (Fig 2b). In tropical Pacific Ocean (10oS~10oN), the heat content of 0-100 and 200-300 layer shows negative correlated (correlation coefficient r = -0.8044), and OHC between 0-100m and 100-200 (r= 0.1026), or between 100-200m and 200-300m (r=-0.2457) were not well correlated (Fig 2b). Correlation analyses were also carried out to check the rationality to take 300m layer as the boundary. Results showed that the negative correlation with the 0-100m OHC reduce with the increase of depth (r =-0.6764 and -0.6075 for OHC200-500, OHC200-700). The heat content anomaly of 0-100m layer and 200-300m layer cancels each other out, resulting in the OHC of 100-200m layer dominates the upper 300m OHC (correlation coefficient between OHC 100-200m and 0-300m is 0.9481). During the 4 major El Nino events from 1980 to 2000 (positive phase PDO), strong cooling took place in the 100-200m layer, leading to OHC variations were several times larger (even one magnitude larger) than that of the 0-100m, or 200-300m layer(Fig2b,c). The upper ocean (0-300m) loses heat when the surface layer (0-100m) is anomalously warm, shows the same characteristic as that in Argo documented (Roemmich and Gilson, 2011).
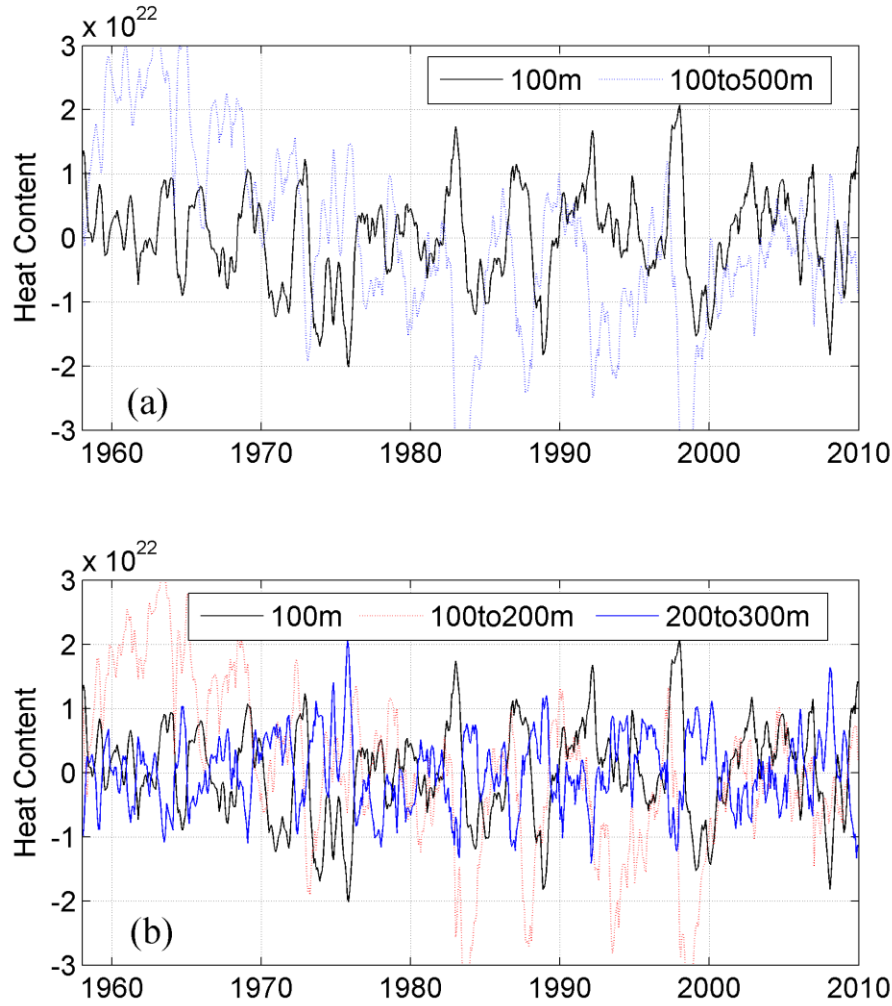
Fig. 4.2 Time series of OHC in the Tropical Pacific Ocean (from 10 ^{o}S to 10 ^{o}N). (a) Surface layer (0-100m) and subsurface layer (100-500m); (b) Time series of OHC the 0~100m, 100~200m, 200-300m in Tropical Pacific (from 10 ^{o}S to 10 ^{o}N)

According to ORAS4 reanalysis data, the redistribution actually happened all the time and in the surface 300m. OHC inter-annual variations in the surface layer of 0-100m and 200-300m layer have opposite trend, related to the east-west tilting of the thermocline in the tropical Pacific (Roemmich and Gilson, 2011). The OHC of the

100-200m has decadal variation besides the inter-annual ENSO related variation; this might be related to the change of shallow overturning cell (England et al, 2014).

4.3.3   Variation of heat content in lower layer in Tropical Pacific

For the lower layer (300-2000m) in tropical pacific, the OHC time series were analyzed using EEMD, to decompose the decadal variation. In contrast, the same analyses were carried out for the OHC time series in the upper layer (0-300) at the meanwhile (Fig 3, 4, 5). In the equatorial Pacific, OHC variation of the upper layer has large magnitude inter-annual change, especially the strong cooling during the 4 El Nino events between 1980 and 2000. The lower layer has the same phase of inter-annual OHC change with the upper layer. However, the decadal change, including imf7, imf8 and the residual trend decomposed from EEMD analysis of the time series of the OHC (will add significance test if necessary), shows the opposite trend for upper and lower layer (Fig 3b). In 1980s -1990s, with warm(Positive) PDO phase, the upper layer lose heat while the surface layer (0-100m) gained heat and the global surface atmosphere temperature underwent strong warming , while the lower layer showed a warming trend and reached its peak in about 1990. In the two decades prior to this period, when PDO is negative, the decadal variation of the OHC of the upper and lower layers showed just the opposite condition. Although the decadal signal might have been limited by the beginning of the time series, an evident decadal vertical redistribution of OHC happed between upper layer and lower layer which also change warming/cooling phase with the PDO.

In tropical Pacific Ocean, the isothermal surface of 12°C is used to derive the upper-ocean layer by many previous studies (Kessler, 1990; Capotondi and Alexander, 2001; Qiu and Chen, 2011). To confirm the vertical heat distribution and the relation

between tilting of the thermocline in the tropical Pacific, the OHC for the upper layer above the 12^oC isotherm and the lower layer to 2000m were analyzed. The decadal variation and pattern shows surprisingly consistent to that using 300 m as the ocean upper layer.

For most of the Tropical Pacific, or even include part of the subtropical ocean, the decadal vertical heat redistribution also happened with a phase lag of about 10 years (Fig4, 5). When the subtropical ocean is included (fig5), the magnitude of cooling of the upper layer is about twice of that warming in the lower layer during Positive PDO, indicating the heat flux to the atmosphere through air-sea interaction.
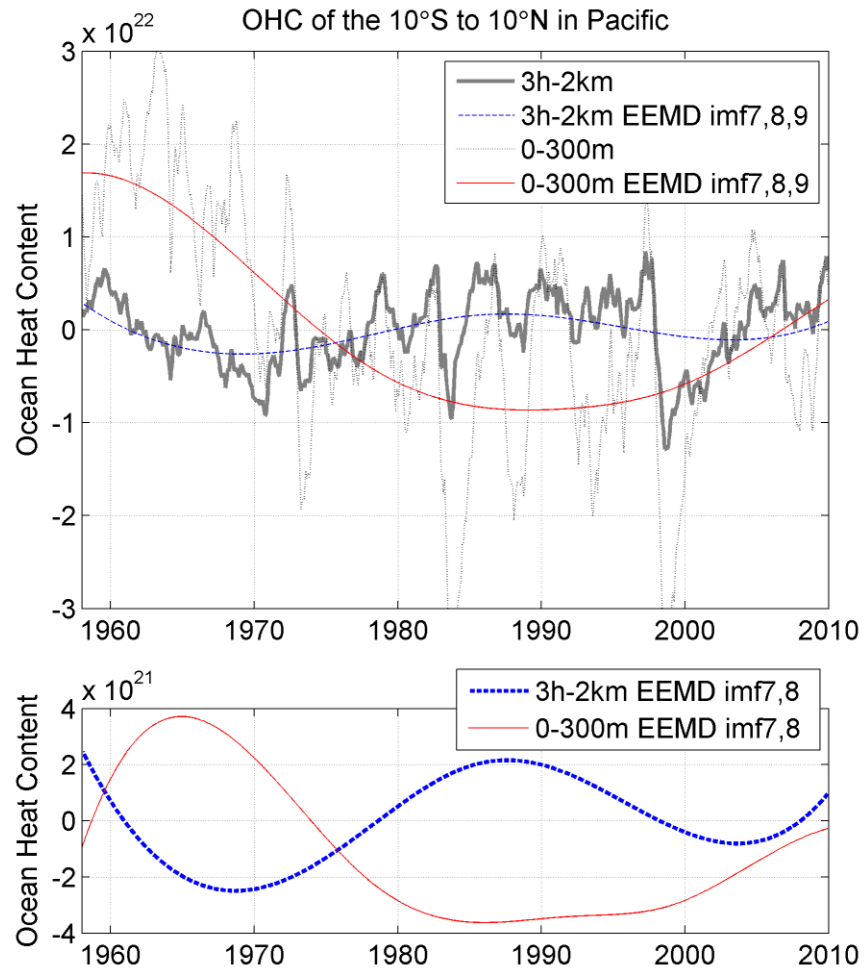
Fig. 4.3 OHC in the Tropical Pacific Ocean (from 10 ^{o}S to 10 ^{o}N): upper layer (0-300m) and lower layer (300-2000m). (a), time series overlaid with EEMD imf7+imf8+residual trend; (b), EEMD imf7+imf8 of the OHC time series.
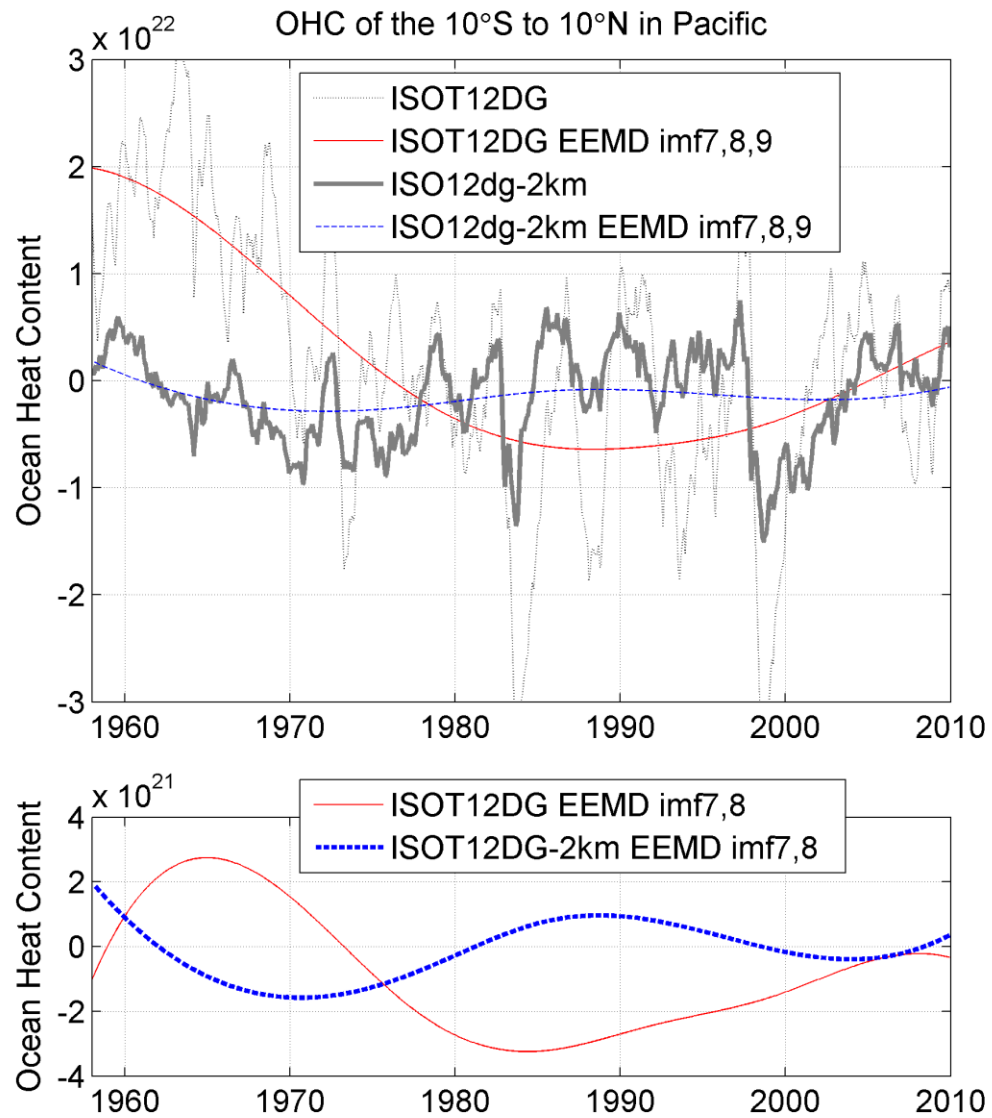
Fig. 4.4 OHC in the Tropical Pacific Ocean (from 10 °S to 10 °N) for upper layer (from surface to isothermal surface of 12°C) and lower layer(from isothermal surface of 12°C to 2000m). a, time series overlaid with EEMD imf7+imf8+residual trend; b, EEMD imf7+imf8 of the OHC time series.

Chapter 5

VARIATION OF RAPID INTENSIFICATION OF MAJOR TROPICAL CYCLONES IN THE WESTERN NORTH PACIFIC: A NEW INDEX AND ITS PRIMARY APPLICATION

Compared to previous tropical cyclone (TC) studies that focus on the frequency of rapid intensification (RI), a new index (RITC) is proposed to measure the RI-level for category 4-5 TCs (Saffir–Simpson scale) in the western North Pacific. RITC is the maximum increase in the sustained-wind-speed per 24-hour during the lifetime of a TC. The results show that the PDO modulation of the interannual ENSO-RI relationship is better represented with the new RITC than with the RI number. The interannual relationship between ENSO and RITC is strong and statistical significant in warm PDO while not significant in cold PDO, mainly attributed to the variation of zonal wind speed. On decadal time scales, the PDO's modulations of ENSO's effects on RITC are mainly attributed to the variations of upper ocean heat content and vertical wind shear. Our results have significant implications for the prediction of RI and long-term projections of major TC activity.

5.1 Introduction

Tropical Cyclones (TCs) are among the most destructive natural disasters in the world [Pielke and Landsea, 2008], especially major TCs [US Department of Commerce, 2006; Lander et al., 2014]. The rapid intensification (RI) of a TC, defined as sustained wind speed increases of at least 30 knots per 24 hours [Kaplan & DeMaria, 2003], is of vital importance to understand TC intensity change and

prediction [Kaplan & DeMaria, 2003; Elsberry et al., 2007; Kaplan et al., 2010; Jiang and Ramirez, 2013]. The intensification of TCs requires proper inner-core structure and interaction with atmosphere and ocean large-scale conditions [Gray, 1979; Price, 1981; Kaplan & DeMaria, 2003; Cione et al., 2013; Lin et al., 2014]. Most major TCs (category 4 and 5 in Saffir–Simpson hurricane wind scale, defined by one-minute maximum sustained wind speed equals of greater than 113 knots, or 58 m/s) experience at least one RI process in their life cycle [Wang & Zhou, 2008]. The necessary environmental conditions for TC intensification and RI have been established to include warmer sea surface temperature (SST), higher low- to mid-troposphere moisture and lower vertical wind shear [Kaplan et al., 2010; Jiang & Ramirez, 2013].

The climatic modulation of the RI, such as the frequency and location of RI occurrences, is important in understanding the variations in major TC activity and in the prediction of TC intensity. The mean number of TC that experienced RI (TCNR) in El Niño years is significantly higher than that in La Niña years [Wang & Zhou, 2008]. The interannual relationship between El Niño/Southern Oscillation (ENSO) and RI Number (RIN) during the warm Pacific Decadal Oscillation (PDO) phase is strong and statistically significant, while there is no significant correlation between ENSO and RIN on the interannual time scale during cold PDO phases [Wang and Liu, 2015].

Ocean thermal control on RI of major TCs has significant implications for seasonal prediction and long-term projections of intense TC activity [Kaplan & DeMaria, 2003; Wang & Zhou, 2008]. The influence of the variations in the upper ocean heat content on the RI of TCs still need further study. Indicators, such as TCNR

and RIN, were adopted to study the frequency of RI. However, there is still minimal research addressing the level of RI and how the level of RI responses to the variation of dynamical and thermodynamic conditions. A new index to measure the level of RI should help add an additional dimension to the research on RI of TCs.

In contrast to previous studies that focus on the frequency or number of RI, a new index for the RI of major TCs (RITC) is proposed. The new RITC is defined as the maximum sustained wind speed (MSWS) increase per 24 hours during the TC lifespan (Fig 5.1a). The study area is the main development region (MDR) of western North Pacific (WNP), which is defined here as 5–26 °N, 122–170 °E. Based on the best track data sets, the frequency distribution of RITC, time-series, and ENSO effects on RI were analyzed in this paper. We also studied change of the ENSO–RITC relationship on the interannual to decadal time scales, and its connection with subsurface warming, atmospheric dynamics, and thermodynamic conditions.

5.2   Data and Method

The 6-hour best track data is from Joint Typhoon Warming Center (JTWC) subset of the International Best Track Archive for Climate Stewardship (IBTrACS) [Knapp et al., 2010], which is available online via: http://www.ncdc.noaa.gov/ibtracs. In this paper, the index for intensify of RI (RITC) is defined as the maximum acceleration of MSWS of major TC during 24 hr period of its lifetime (as shown in Fig 5.1a). The annual mean RITC is obtained from taking average of the RITC for all the major TCs during peak typhoon season (May-November) every year 1958-2013.

The Multivariate ENSO Index (MEI) is proposed by Wolter [1987], Wolter and Timlin [1998] to monitor ENSO based on the six main observed variables over the tropical Pacific, including sea-level pressure, zonal and meridional components of the

surface wind, sea surface temperature, surface air temperature, and total cloudiness fraction of the sky, available online: http://www.esrl.noaa.gov/psd/enso/mei/.

The decadal variation of the Sea Surface Temperature Anomaly (SSTA) and Ocean Heat Content (OHC) in the upper 100m (OHC100) in Pacific Ocean is analyzed using ORAS4 reanalysis data sets [Balmaseda et al., 2013b]. Relative Humidify (RHUM), Vertical Wind Shear (VWS) and zonal components of the surface wind field (UW) is the 20th Century Reanalysis V2 data, provided by the NOAA/OAR/ESRL PSD, Boulder, Colorado, USA, from their Web site at http://www.esrl.noaa.gov/psd/. The spatial and temporal variation of dynamic and thermodynamics conditions, including OHC, RHUM, VWS and wind field, were analyzed by Empirical Orthogonal Function (EOF) analysis.

5.3   Results

5.3.1   Rapid Intensification Index for intense TCs (RITC) and its variations

To demonstrate the physical meaning of RITC, Fig 5.1a shows the evolution of maximum sustained wind speed of 3 selected intense TCs. TC1979#24 (numbered by JWTC, similarly hereinafter) experienced a strong RI and took less than 3 days to achieve the peak intensity of 140kt and the TC1992#17 achieved the peak intensity of category 4 in more than one week without RI. TC1988#23 went through a weaker RI and peaked in about 4 days. The RIN for TC1988#23 and TC1979#24 both were 6 according to Wang and Liu [2015] and Kaplan and DeMaria [2003], employing the intensify change threshold of 30kt/24h for RI. From the perspective of RIN, the intensity change of TCs might not have been fully represented. To better understand the dynamic and thermodynamic conditions that are favorable to the RI of intense TCs,

RITC was proposed here as the maximum wind speed increase per 24 hours during the TC lifetime. As shown in Fig 5.1a, the red bars represent the magnitude of RITC, 70kt, 35kt, and 25 kt for TC1979#24, TC1988#23 and TC1992#17, respectively. RITC better illustrates the intensity change of the TCs. With a high RITC, TC can reach peak intensity in very short time, similar as TC1979#24, leaving little time for people in areas of impacts to response to potential damage.
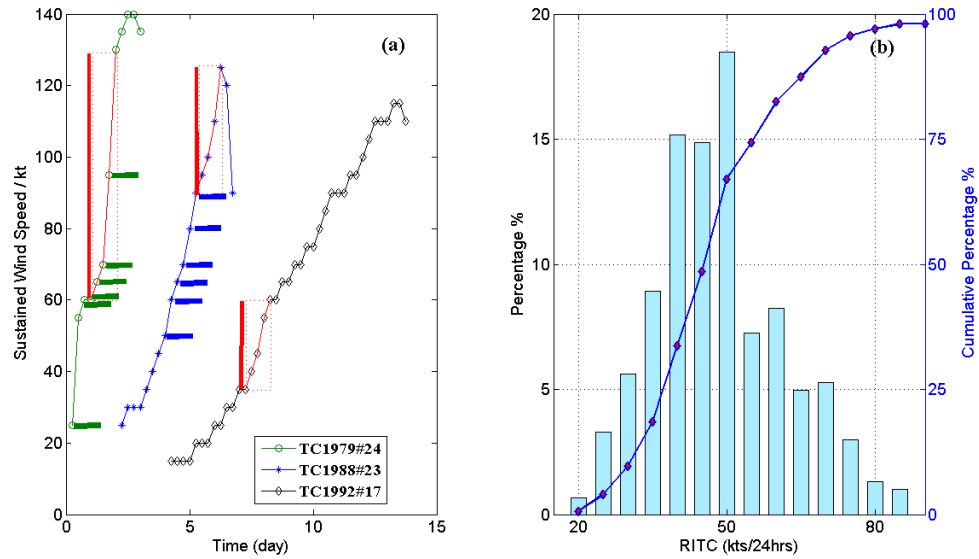
Fig. 5.1 (a) Time evolution of maximum sustained wind speed, RI and RITC for three Cat4&5 TCs, horizontal bars show RI processes, number of horizontal bars is RIN and vertical red bars show the RITC. (b) The frequency distribution of RITC for all the Cat4&5 TCs from May to November during 1958-2013.

The distribution of RITC for all the major TCs is shown in Fig 5.1b. Less than 5% of major TCs in the WNP have RITC of less than 30 kt, which means they do not experience RI during their lifetime. The RITC ranges from 20 to 90 kt, and the percentage increases from less than 1% for 20 kt to about 18% for 50 kt then decreases dramatically to 7%-8% for 60 kt and decreases to about 1% for 85-90 kt.

Approximately half of the major TCs have a RITC between 40-55 kt, and 25% RITC larger than 60 kt.

The time series of the annual mean RITC shows a large interannual variability, especially in early 1970s, middle of 1980s and late 2000s (Fig 5.2a). The 7-year running mean shows a large variance, with a peak in the mid-1960s at 60 kts and a minimim at 40 kts in early 1990s. The TCNR shows large interannual and decadal variation but not a linear trend, which is consistant with Wang and Zhou [2008]. The decadal trend is different from those for RIN (Fig 5.2b), TCNR (Fig 5.2c). Although we use the same intensify change threshold as Wang and Liu [2015], the RIN time series is significantly different from their results (Fig 5.1b in Wang and Liu, 2015) in the late 1980s and early 1990s. Since a TC might experience more than one RI, the RIN should be larger than (no less than, at least) the TCNR, as shown in Fig 5.2b and Fig 5.2c. The time series of RIN in Fig 5.2b is more reasonable, compared to Wang and Liu's [2015] results. The ratio between RITC and the peak intensity (wind speed) ranges from 0.27 to 0.47 and shows the same interannual and decadal trend as the RITC (Fig 5.2d).

The relationship between the annual RITC and the annual RIN, and the annual TCNR is not significant at 90% confidence level (Fig 5.2e and Fig 5.2f). This indicates that the control factor for intensity and frequency of RI is different. It is essential to consider both the variation of intensity and frequency of RI to improve the understanding of RI in a changing climate.
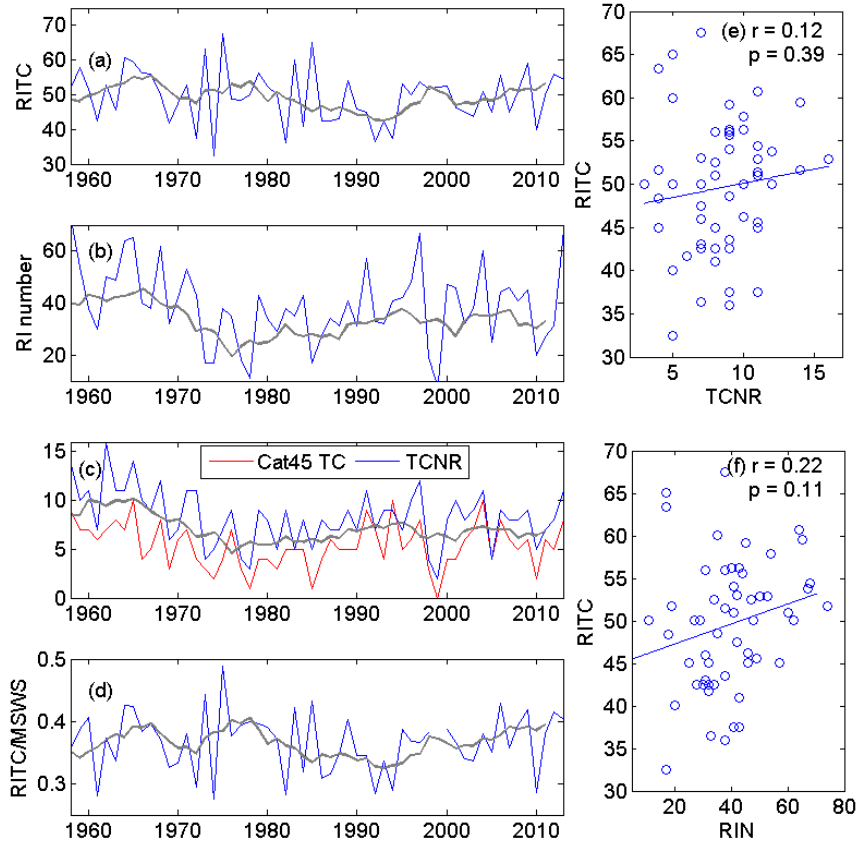
Fig. 5.2 The time series of the annual mean (a) RITC (kt/24hour), (b) RIN, (c) the annual number of category 4 and 5 TC (Cat 45 TC), and the annual number of TC that experience RI process (TCNR), (d) the annual mean of RITC/Max wind speed ratio. The thick gray lines denote five-year running mean. In (c), thick gray line indicates the 7- year running mean of TCNR. Scatter diagrams between the annual averaged RITC and (e) TCNR, (f) annual RIN, the blue line is the linear regression. All data were during the peak TC seasons (May-November) in the WNP MDR for the period of 1958-2013.

5.3.2   ENSO effect on RI and PDO modulation

The annual mean RITC is negatively correlated (r = -0.17) with the May-November-averaged MEI and is not significant at the 90% confidence level (p-value = 0.19). In a similar manner, the correlation between the annual mean RITC and MEI is

calculated (Fig 5.5). The significant (at the 90 % confidence level) negative correlation persists from the early 1970s to early 1990s, and turns into a positive correlation in the 2000s, showing a large decadal variation in the past decades. This could be related to the PDO modulation of the relationship between ENSO and RI.

Three RI indices (RITC, TCNR and RIN) were used to identify the relationship between RI and ENSO, and the PDO-induced modulations of this relationship. In the light of previous study on PDO modulation of the RI variation [Wang and Liu, 2015], the correlation analyses were performed for both phases of the PDO. Fig 5.5 shows the decadal variation of the detrended PDO index. We use 1975-1999 as warm PDO phase period, 1958-1974 and 2000-2013 cold PDO phase period in following part of this paper. Figure 3 shows that an evident PDO modulation of on the interannual ENSO-RI relationship can be identified for all those three indices. The annual RITC in warm PDO phase is significantly negative correlated with the MEI at the 95% confidence level, whereas there is no significant correlation during the cold phase (Fig 5.3a and Fig 5.3b). The RIN and ENSO have a similar pattern of correlation, except the relationship is positive correlation and significant at the 90% confidence level at warm PDO phase (Fig 5.3c and 5.3d). The interannual relationship between ENSO and annual RIN is modulated by the PDO. The ENSO/RIN relationship is strong and significant during the warm phase of the PDO with a correlation significant at the 90% confidence level, while there is no significant correlation between ENSO and RIN during the cold PDO phase. This result agrees with Wang and Liu's [2015] assessment, although the RIN time series has been updated in the current study. For the TCNR, the difference in the relation with MEI for the different PDO phases is relatively small compared to that for RITC and RIN. Among all 3 indices, the RITC has the largest

change in correlation coefficient and the correlation significance level for different PDO phases. This indicates that the PDO modulation of the interannual ENSO-RI relationship is better represented with the new index RITC. It also suggests that during the warm PDO phase, ENSO's influence on the interannual variability of RITC is much stronger than that during cold PDO phase.

To further identify the ENSO-RI relationship on longer (decadal) time scale, correlation analysis was carried out with the 7-year smoothed time series. There is no significant correlation between overall RITC and MEI on decadal time scale ($r = 0.02$, p-value = 0.89). However, Fig 5.3g and Fig 5.3h show the results for different PDO phases. The ENSO-RI relationship is modulated by PDO, with a significant (at the 99% confidence level) negative (positive) correlation during warm (cold) PDO phase. This suggests that influence ENSO exerted on the decadal variation of RITC is strong during different PDO phases, but the influence will change sign for different PDO phases, which might be related to the change of RITC controlling physical mechanisms.
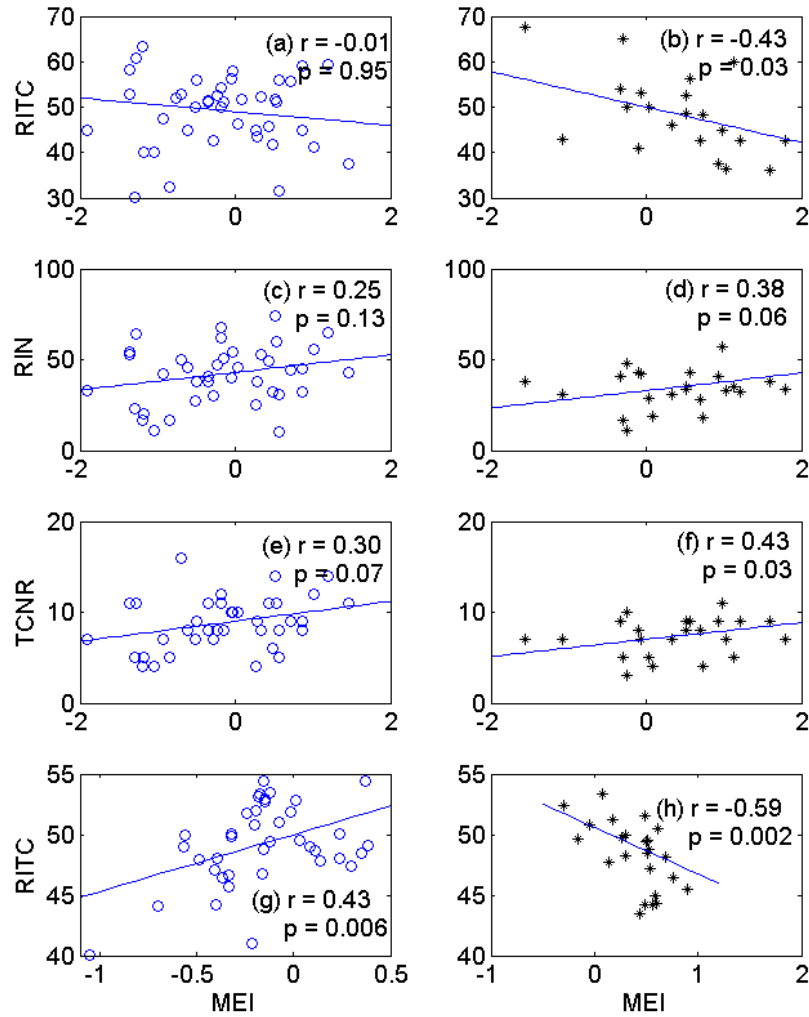
Fig. 5.3 Scatter diagrams between the averaged-May-November MEI and (a, b) annual mean RITC, (c, d) annual TCNR and (e, f) annual RIN, and (g, h) between the 7-year moving smoothed MEI and annual mean RITC for the cool (left panel) and warm (right panel) PDO phase. The blue line is the linear regression. The correlation coefficient and the p-value for significant tests are labeled in subplots.

5.3.3 The effect factors of RITC variation

To address the physical mechanisms responsible for the changes in the interannual and decadal ENSO/RITC relationship, the corresponding oceanic and atmospheric conditions associated with RI were explored using EOF analysis. The first principal component (PC1) time series and EOF1 of the SSTA, OHC100, VWS, RHUM and UW. Their PC1s are highly correlated with the MEI, with correlation coefficient of -0.97, -0.92, 0.91, 0.77 and -0.81 and statistically significant at the 99% confidence level. Their EOF1s account for 42.4, 41.5, 19.0, 16.9 and 23.8% of the total variance. EOF1 of OHC100, RHUM and VWS and time series of their PC1 were shown in Fig 5.6, with patterns consistent with that found by Wang and Liu [2015]. EOF1 of Zonal wind (UW) is characterized by the monopole located in the Western Tropical Pacific and the EOF1 of SSTA reveals a tongue pattern from central Pacific to Eastern Pacific (Fig 5. 7).

To investigate the effects of the oceanic and atmospheric conditions that associated with the ENSO on the RITC for warm and cold phases, the correlation analyses between RITC and PC1 of the SSTA, OHC100, VWS, RHUM and UW in the MDR in WNP were performed for annual and decadal time scales. Fig 5.4 shows the correlation coefficients for those analyses. For the interannual variation, the EOF1 of OHC100 reveals a positive correlation with RITC in both warm and cold phase, but not statistical significant at the 90% confidence level, indicating that OHC100 contributes less to the interannual ENSO-RITC relationship change with the different PDO phase. The EOF1 of SSTA reveals a positive correlation (r = 0.35) with RITC at the 90% confidence level for warm PDO. By contrast, the correlation coefficient (0.17) for RITC and MEI in cold PDO is not statistically significant. Similarly, the correlation between the EOF1s of VWS (0.37), RHUM (0.38), UW(0.40) and annual

mean RITC in warm PDO is statistically significant above the 90% (95% for UW) confidence level, and much higher than that (0.05, 0.04 and 0.03 for VWS, RHUM and UW) in cold PDO phase, which is hardly correlated with RITC. So the atmospheric dynamic (VWS, UW) and thermodynamic (SSTA, RHUM) conditions contributed to the modulating the change of interannual ENSO-RITC relationship in different PDO phases, and the atmospheric dynamic factor (UW) may be dominant.
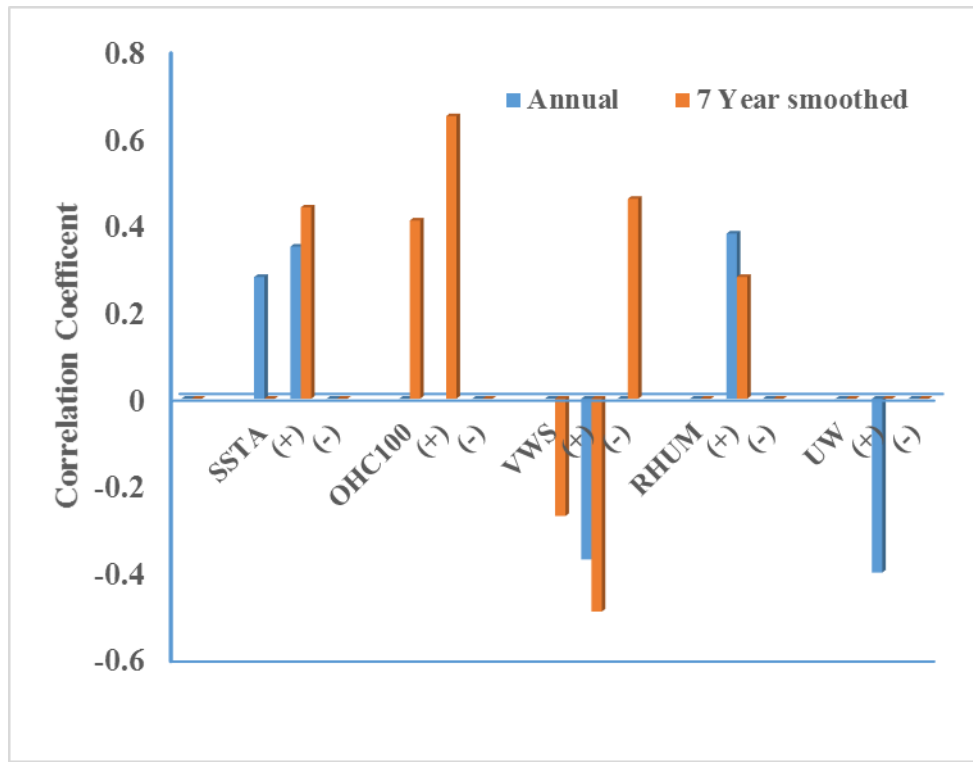
Fig. 5.4 The correlation coefficient between annual mean RITC and averaged-may-November SSTA, OHC100, VWS, RHUM and UW for 1958-2013, and for warm (+ denoted) and cold (- denoted) PDO phases, only show the coefficient for the correlation that is significant at the 90% or higher confidence level.

For the decadal variation, the correlation between the EOF1s of SSTA (0.44) and annual mean RITC in warm PDO is statistically significant above the 95%

confidence level, and is hardly correlated in cold PDO phase. The EOF1 of OHC100 in warm PDO is highly correlated with RITC (r = 0.65, p = 0.001), but has a small correlation in cold phase of PDO. The PC1 of VWS reveals negative (positive) correlation with RITC in warm (cold) PDO phase, significant at the above 99% confidence. During warm PDO phase, OHC100 dominants the decadal variation of RITC, while VWS dominants in cold PDO phase. These comparisons suggest that the thermodynamic factor (OHC100) and the atmospheric dynamic factor (VWS) play important roles in modulating the change of decadal ENSO-RITC relationship in the different PDO phases.

5.4 Discussion

Recent research shows [Kang and Elsner, 2015] a trade-off between intensity and frequency of TCs on a global scale, suggesting the importance of using indicators of frequency, intensity and activity together. For the research on RI of TC, RIN and number of TC that experienced RI have been used as indicators of frequency [Kaplan & DeMaria, 2003; Elsberry et al., 2007; Wang & Zhou, 2008; Kaplan et al., 2010; Jiang and Ramirez, 2013; Wang and Liu, 2015]. The RIN can reflect the RI intensity at certain extent but not complete (Fig 5.1a). A better understanding of the variation of RI and global warming's influence on RI requires new indicator for the level of RI. RITC is the maximum wind speed increases per 24 hours during the TC lifetime and describes the level of RI. Our results show that the RITC is independent from indicators of frequency, especially during the warm PDO phase (Fig 5.8).

Results show that there is no statistically significant interannual relationship between the RITC and TCNR, and RIN (Fig 5.8b and 5.8d) in the warm PDO phase, indicating a different controlling factor for the intensity and frequency of RI. The

enhancement of the interannual RIN relationship in the warm PDO phase is attributed to the change of the environmental vertical wind shear [Wang and Liu, 2015]. On a decadal time scale, the change of vertical wind shear contributed to the ENSO-RITC relationship change. However, for the interannual ENSO-RITC relationship in different PDO phases, the variation of the zonal wind is dominant. This might related to the moving speed of TCs. Fig 5.9 shows the highly correlation of TC moving speed with the zonal wind speed in warm PDO phase. Lin et al. [2014] studied the intensification of super-typhoon Haiyan and concluded that a fast moving speed contributed to the RI of TC more than the warming of the upper ocean. We also noticed that the RITC is significantly related to TCNR (Fig 5. 8a) and RIN (Fig 5.8c) during cool PDO period. This indicates that the control factors for intensity and frequency of RI might be more similar during the cold PDO phase.

The RI requires a large amount of latent heat energy to be efficiently extracted from the ocean upper layer [Wang & Zhou, 2008]. However, the wind stress pumps colder subsurface water to the sea surface, reduces the SST, and induces the cooling effect during TC intensification [Price, 1981, 2009]. The subsurface OHC thus become very important to depress the cooling effect and to the RI process [Holliday and Thompson,1979; Shay et al., 2000; Lin et al., 2008, 2009, 2014, 2015; Price, 2009; Pun et al., 2013;; Jin et al., 2015]. Wang and Zhou [2008] studied the annual TCNR and location of the RI on annual, intraseasonal, and interannual time scales in the WNP, focusing on the atmosphere conditions. Their findings suggest that the ocean heat content in the upper ocean can be a critical factor that determines the RI. The relationship between the RIN and tropical cyclone heat potential (TCHP) is not statistically significant for the interannual time scale [Wang and Liu, 2015]. Our

analysis also suggests that the annual mean RITC is not significantly correlated with the OHC in the upper ocean for the interannual time scale. However, on longer time scales, OHC100 dominates the RITC variation during the warm PDO phase, indicating that RITC can reflect the ocean thermal control of ENSO on RI of TCs, which has significant implications for seasonal prediction and long-term projections of intense TC activity.

5.5 Conclusions

RITC, a new index to measure the level of RI for major TCs, was proposed, Results show that RITC is independent from the indicators for IR frequency, especially during the warm PDO phase. The variations of RITC for strong TCs in WNP were studied using TC best track data from the Joint Typhoon Warning Center.

Based on the new RITC index, the PDO-modulated ENSO effect on RI is studied on interannual and decadal timescales. Compared to the RIN and TCNR, the PDO modulation of the interannual ENSO-RI relationship is better represented with the RITC. The interannual relationship between ENSO and RITC is strong and significant in the warm PDO phase and not significant in the cold PDO phase. However, RITC is negatively (positively) correlated with ENSO in the warm (cold) PDO phase on a decadal time scale and is statistically significant at the above 99% confidence.

The environmental conditions by which the PDO modulates the effects of ENSO on RITC are investigated. A correlation analysis reveals that VWS, UW, thermodynamic SSTA, and RHUM conditions contributed to the modulated changes of interannual ENSO-RITC relationship in different PDO phases. The contribution of upper ocean OHC is limited. The atmospheric dynamic factor UW's dominant role

might exist due to the high correlation between the UW and the moving speed of TCs. On decadal time scales, the upper ocean OHC (VWS) dominates the ENSO-RITC relation in the warm (cold) PDO phase. The thermodynamic factor (OHC100) and atmospheric dynamic factor (VWS) play important roles in modulating the change of decadal ENSO-RITC relationship in the different PDO phases. The specific physical mechanisms for this modulation need further investigation.
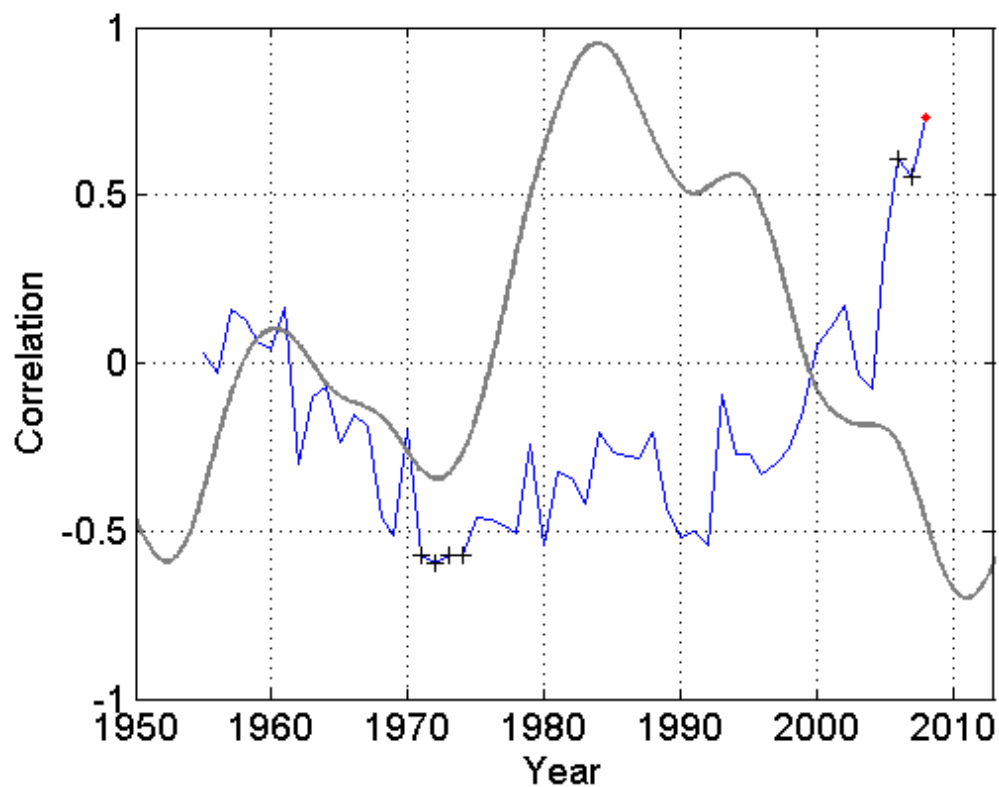
Fig. 5.5 Ten-year sliding correlation between averaged May-November MEI index and the RITC during 1958-2013 (blue line), red dots indicate the correlation is significant at the 95% confidence level, black cross for the 90% confidence level. Thick gray line is the 15 year hanning smooth of the detrended PDO index.
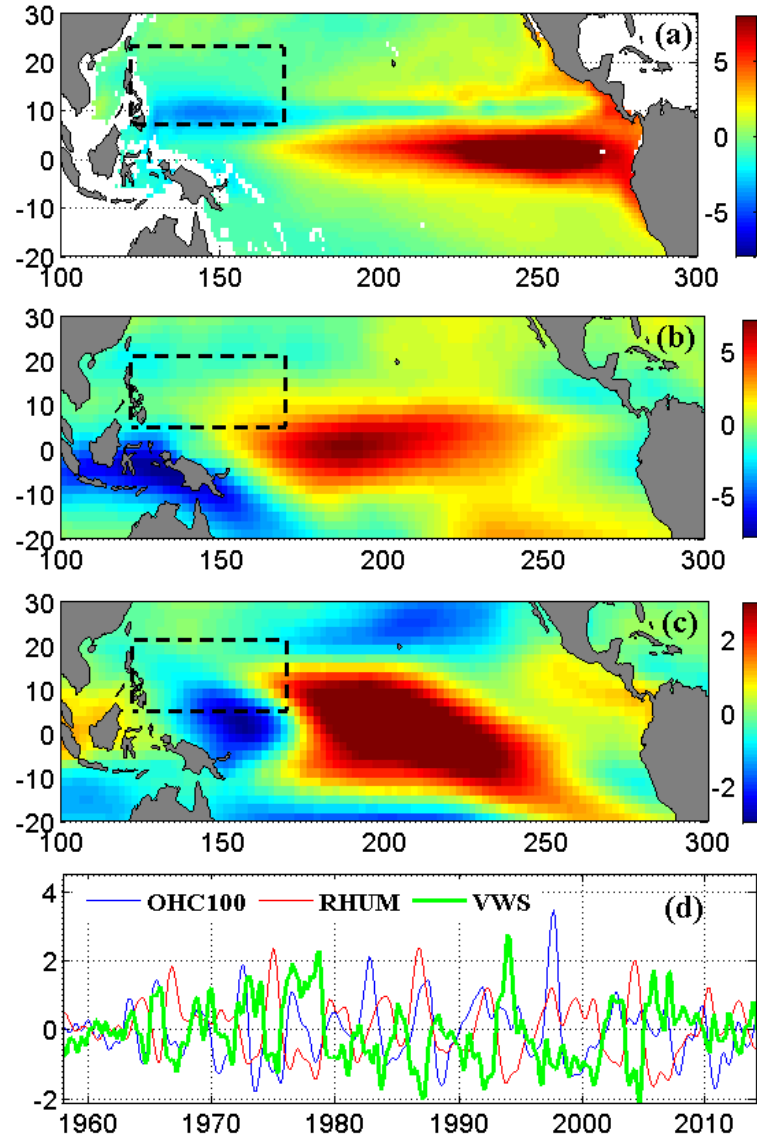
Fig. 5.6 EOF1 of the May-November (a) OHC100, (b) RHUM, and (c) VWS during 1958-2013 in the Tropical Pacific Ocean, and (d) time series of PC1s. The thick dash boxes denote the MDR in WNP.
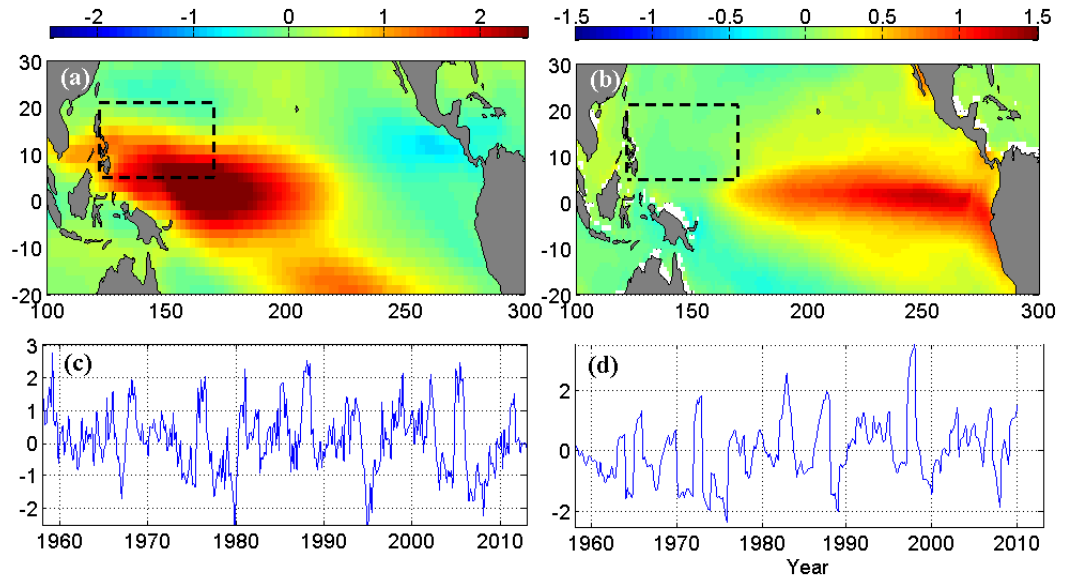
Fig. 5.7 EOF1 of the May-November (a) UW and (b) SSTA during 1958-2013 in the Tropical Pacific Ocean, and (c, d) time series of PC1s. The thick dash boxes denote the MDR in WNP.
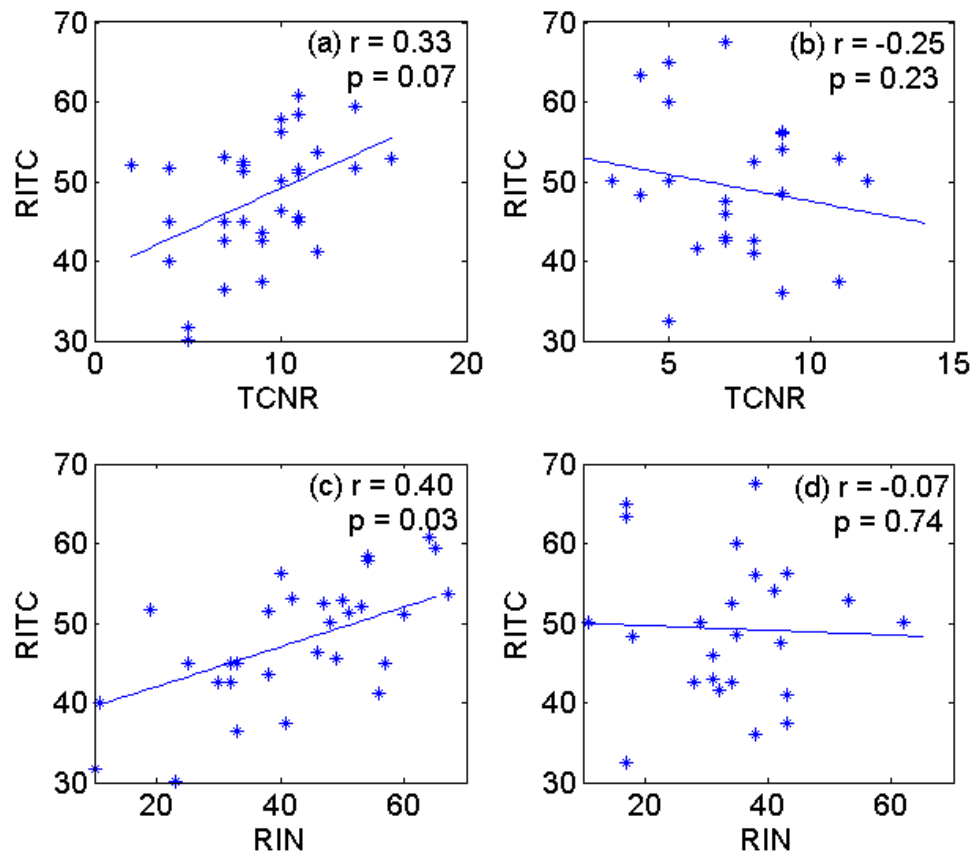
Fig. 5.8 Scatter diagrams between the annual averaged RITC and (a, b) TCNR, (c, d) annual RINs for the cold (right panel) and warm (left panel) PDO phase, the blue line is the linear regression. The correlation coefficient and the p-value for significant tests are labeled in subplots.
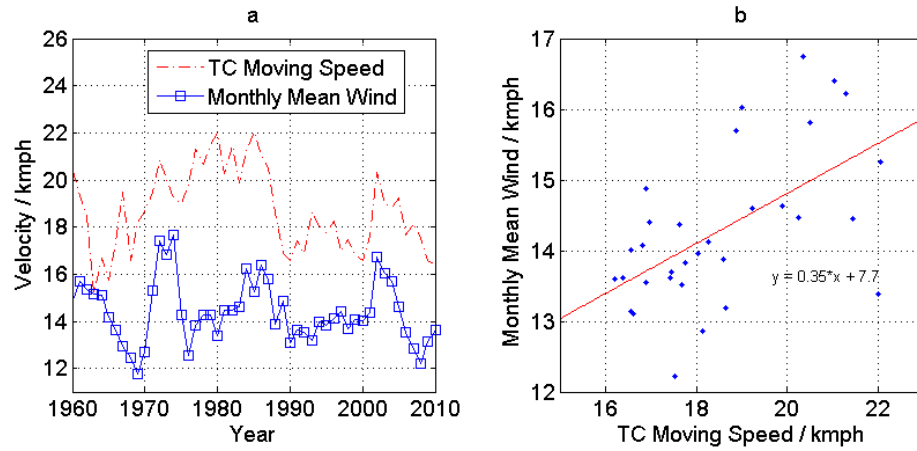
Fig. 5.9 The relationship between TC moving speed and the monthly mean wind speed.
(a), Time series of the annual mean TC moving speed (red) for when the
intensification peaks and the monthly mean wind(blue); (b) scatter plot for TC moving
speed at intensification peak and the monthly mean wind(red line show the linear
relation, correlation coefficient 0.57, p=0.001).

Chapter 6

CONCLUSIONS

The global warming hiatus is a period of slowdown of warming rate and relatively little change in globally averaged surface temperatures and since 1998. Trade wind and wind driven circulation variation and related heat redistribution to subsurface and deep layer in Pacific and Atlantic Ocean is believed to be one of the major mechanisms: internal variability of climate. However, what role has Indian Ocean played in global warming hiatus, since the warming hiatus is for global ocean which means all the global ocean basins should be included? What's the physical mechanisms for multi-decadal variability in global climate modes? How has the regional climate responded to global warming hiatus in western Pacifc Ocean? In this dissertation, we investigated the spatio-temporal variations of the Ocean Heat Content (OHC) to reveal the physical mechanisms of the global warming hiatus and the regional climate response in Western Pacific Ocean.

6.1 Summary of the Main Results

Three questions were addressed in this thesis (chapter 2-4) and the following provides a summary of the results.

Chapter 2: Can ocean remote sensing be extended to subsurface and deeper layer to provide new data for ocean heat content research?

● A Self-Organizing Map Neural Network (SOM) was developed from Argo gridded data sets in order to estimate subsurface temperature anomaly (STA) from remote sensing data, such as SST, SSH, SSS.

● In the Gulf Stream Path areas, the STA estimations from the SOM algorithm show good agreement with in situ measurements taken from the surface down to 700m depth, with a correlation coefficient lager than 0.8.

● Sensitivity of the SOM, when including salinity shows that with SSS anomaly data in the SOM training process, reveal the importance of SSS information, which can improve the estimation of STA in the subtropical ocean by up to 30%. In subpolar basins, the monthly climatology SST and SSH can also help to improve the estimation by as much as 40%.

● STA time series for 1993~2004 in the mid-latitude North Atlantic were estimated from remote sensing SST and altimetry time series using the SOM algorithm.

Chapter 3: What's role of OHC redistribution, both horizontally and vertically, in the mechanisms for global warming hiatus?

● A meridional dipole has dominated the variation of the ocean heat content in the upper layer, and the warming in the upper layer of the Indian Ocean has been in "hiatus" since early 1980s.

● Causal analysis method revealed that the warming in the southern subtropical Indian Ocean contributed to the pre-conditioning and warming in the southern and tropical Atlantic since 1980s.

● The Agulhas system contributed to the heat sequestration at the deeper layer in the Southern Ocean during the global surface warming hiatus period.

● Global ocean and atmosphere form a closed loop, under the "global ocean at play" wind and wind-driven circulation framework, explains the mechanisms and processes for the hiatus to occur under the global warming setting.

Chapter 4: How the oceanic and atmospheric processes response to the global warming and hiatus in western Pacific?

● The decadal variation of vertical OHC distribution in Western North Pacific were studied to reveal regional climate respond to global warming hiatus. An evident decadal vertical redistribution of OHC happened between upper layer and lower layer which also change warming/cooling phase with the PDO.

● A new index for Rapid Intensification of Intense TCs (RITC), defined as the maximum wind speed increase and central pressure drop within 24 hour during TC lifetime, was proposed to study the variations of the TC intensity.

● The PDO modulation of the interannual ENSO-RI relationship is better represented with the new RITC than with the RI number. The interannual relationship between ENSO and RITC is strong and statistical significant in warm PDO while not significant in cold PDO, mainly attributed to the variation of zonal wind speed.

● On decadal time scales, the PDO's modulations of ENSO's effects on RITC are mainly attributed to the variations of upper ocean heat content and vertical wind shear.

6.2 Implications for Present-day Climate and Prospect for Further Research

In this thesis, OHC was used as tracer to study the decadal heat redistribution, horizontal and vertical, in the ocean, and the possible contribution to global warming and hiatus, and to the multi-decadal climate variability. The proposed theory in chapter 3 summarizes all the known mechanisms on wind and wind-driven circulation that related to global surface warming hiatus, and identify the previously neglected Indian Ocean as one of the important contributors to the current hiatus through its meridional dipole mode and the Agulhas Current system. Thus, the global surface warming hiatus involves all the ocean basins. Although this study only partially explains the mechanisms and processes for the current hiatus, well-designed numerical models can provide further validations in the future. Moreover, we acknowledge the uncertainties resulting from data and method limitations, so this theory may not apply to previous hiatus events because of the unprecedented rate of warming due to high concentration of greenhouse gases. We also refrain ourselves from predicting how long the current hiatus will last and how it will end, given the aforementioned limitations and possible social consequences. How the accelerated wind and wind-driven circulations will distribute CO_2 and the resulting extra heat through the ocean interior is still a challenging issue.

The regional atmosphere an ocean interaction and climate response to global warming and hiatus mainly focus on the subsurface warming and cooling, eastern trade wind weaken and intensify, and their impact on rapid intensification of tropical cyclone in western North Pacific. In recent years, TCs in Western North Pacific basin (WNP) have raised many concerns. Supertyphoon Haiyan made landfall with wind speed of 170 kts in November 2013 resulting in catastrophic destruction in Philippines. In July 2014, Rammasun, a category-4 equivalent typhoon, made landfall in its peak

intensity as the most severe typhoons to hit south China Coast in 41 years. It is worth mentioning that 8 out of the 11 typhoons developed in WNP were category-4 equivalent or stronger (5 category-5 equivalent) supertyphoon in 2014 (Joint Typhoon Warning Center, JTWC). Results of chapter 4 explain the recent increase of the intense TCs in the WNP, and the high frequency extreme intensity of intense TC and in 1950s and 1960s during previous GWH. A return period of 60-65 year is proposed based on the analysis of GSAT, and high RITC and more intense TCs are expected in the coming decade, with great potential implications for life and property throughout the WNP coast and islands.

Recent development of intense TCs in WNP shows an unusual sign for seasonality shift of TC in boreal winter and spring. Typhoon Hagupit, of which the maximum 1-minute sustained winds of up to 180mph, formed in December 2014. And an unusually intense early-season tropical cyclone and the most powerful pre-April typhoon on record in the western north Pacific Ocean, Typhoon Maysak formed in later March 2015 and reached an maximum 1-minute sustained wind of 160mph (according to Japan Meteorological Agency. National Institute of Informatics). This seasonality shift might be related to the decadal variation of dynamic and thermodynamic condition in WNP. Further investigation on this issue would improve the understanding of TC activities variation under a warming climate.

REFERENCES

Abraham, J. P., M. Baringer, N. L., Bindoff et al, 2013. A review of global ocean temperature observations: Implications for ocean heat content estimates and climate change. Reviews of Geophysics. DOI: 10.1002/rog.20022

Ali, M.M., D.Swain, and R.A. Weller, 2004: Estimation of ocean subsurface thermal structure from surface parametersL A neural network approach, Geophys. Res. Lett., 31, L20308, doi:10.1029

Andronova, N. G., and M. E. Schlesinger, 2000: Causes of global temperature changes during the 19th and 20th centuries. Geophys. Res. Lett., 27, 2137–2140.

Antonov, J. I., S. Levitus, and T. P. Boyer (2005), Thermosteric sea level rise, 1955-2003,Geophysical Research Letters, vol. 32, L12602, doi: 10.1029/2005GL023112.

Arhan, M., 1987: On the large scale dynamics of the Mediterranean outflow. Deep-Sea Res., 34, 1187–1208.

Arndt, D. S., M. O. Baringer, and M. R. Johnson, Eds., 2010: State of the Climate in 2009. Bull. Amer. Meteor. Soc., 91 (7), S1–S224.

Bala G 2013. Why the hiatus in global warming in the last decade? CURRENT SCIENCE [J], 105: 1031-1032.

Balmaseda, M. A., K. E. Trenberth, and E. Källén (2013a), Distinctive climate signals in reanalysis of global ocean heat content, Geophys. Res. Lett., 40, 1754–1759, doi:10.1002/grl.50382.

Balmaseda, M. A., Mogensen, K. and Weaver, A. T. (2013b), Evaluation of the ECMWF ocean reanalysis system ORAS4. Q.J.R. Meteorol. Soc., 139: 1132–1161. doi: 10.1002/qj.2063.

Barnett, T. P. et al. Penetration of humaninduced warming into the world's oceans. Science, 309, 284–287 (2005).

Beal, L. M., Chereskin, T. K., Lenn, Y. D. & Elipot, S. The sources and mixing characteristics of the Agulhas Current. J. Phys. Oceanogr. 36, 2060–2074 (2006).

Beal, L. et al. On the role of the Agulhas system in ocean circulation and climate. Nature 472, 429–436 (2011).

Bell, G. D. and M. Chelliah (2006), Leading Tropical Modes Associated with Interannual and Multidecadal Fluctuations in North Atlantic Hurricane Activity. J. Climate, 19, 590–612. doi: http://dx.doi.org/10.1175/JCLI3659.1.

Biastoch, A. & Böning, C. Anthropogenic impact on Agulhas leakage. Geophys. Res. Lett. 40, 1138–1143 (2013).

Biastoch, A., Böning, C., Schwarzkopf, F. & Lutjeharms, J. Increase in Agulhas leakage due to poleward shift of Southern Hemisphere westerlies. Nature 462, 495–498 (2009).

Bindoff, N. L., et al., (2007), Observations: oceanic climate change and sea level. In:Solomon, S.; et al., (eds.) Climate change 2007: the physical science basis. Contribution ofWorking Group I. Cambridge, Cambridge University Press, 385-428.

Boening, C., J. K. Willis, F. W. Landerer, R. S. Nerem, and J. Fasullo (2012), The 2011 La Niña: So strong, the oceans fell, Geophysical Research Letters, 39, doi:10.1029/2012GL053055. [online] Available from: http://dx.doi.org/10.1029/2012GL053055

Bouttier F, Courtier P. Data assimilation concepts and methods March 1999[J]. Meteorological training course lecture series. ECMWF, 2002.

Bowden, , K. F.; L. A. Fairbairn, A Determination of the Frictional Forces in a Tidal Current. Proceedings of the Royal Society of London. Series A, Mathematical and Physical Sciences, Vol. 214, No. 1118. (Sep. 23, 1952), pp. 371-392.

Bozec, A., M. S. Lozier, E. P. Chassignet, and G. R. Halliwell, 2011: On the variability of the Mediterranean Outflow Water in the North Atlantic from 1948 to 2006. J. Geophys. Res., 116, C09033.

Chambers, D. P., et al., 1997. Long-period ocean heat storage rates and basin-scale heat fluxes from TOPEX. Journal of Geophysical Research: Oceans 102(C5): 10525-10533.

Chan, J. C. L. (2000), Tropical cyclone activity over the western North Pacific associated with El Nin˜o and La Nin˜ a events. J. Climate, 13, 2960–2972. doi: http://dx.doi.org/10.1175/1520-0442(2000)013<2960:TCAOTW>2.0.CO;2.

Chan, J. C. L. (2008), Decadal variations of intense typhoon occurrence in the western North Pacific. Proc. Roy. Soc. London, 464A, 249–272. DOI: 10.1098/rspa.2007.0183.

Chan, J. C. L. (2009), Thermodynamic control on the climate of intense tropical cyclones. Proc. Roy. Soc. A., 465, 3011-3021, doi: 10.1098/rspa.2009.0114.

Chan, J. C. L. (2010), Global warming and tropical cyclone activity in the western North Pacific from an observational perspective. In Climate Dynamics: Why Does Climate Vary? D.-Z. Sun and F. Bryan (Eds.), Geophysical Monograph 189, American Geophysical Union, 193-205. DOI: 10.1029/2009GM000849.

Chen, X. & K.-K. Tung (2014), Varying planetary heat sink led to global-warming slowdown and acceleration. Science 345, 897–903. DOI: 10.1126/science.1254937.

Chu, P. C., C. Fan, and W. T. Liu, 2000: Determination of vertical thermal structure from sea surface temperature. J. Atmos. Oceanic Technol., 17, 971–979.

Church, J. A., et al., (2011), Revisiting the Earth ¡¯s sea-level and energy budgets from 1961 to2008, Geophysical Research Letters, 38, L18601, doi: 10.1029/2011GL048794.

Chylek, P., J. Klett, G. Lesins, M. K. Dubey, and N. Hengartner, 2014. The Atlantic Multi-decadal Oscillation as a dominant factor of oceanic influence on climate, Geophysical Research Letters, doi:10.1002/2014GL059274. [online] Available from: http://dx.doi.org/10.1002/2014GL059274

Cione, J. J., Evan A. Kalina, Jun A. Zhang, and Eric W. Uhlhorn (2013) Observations of Air–Sea Interaction and Intensity Change in Hurricanes. Mon. Wea. Rev., 141, 2368–2382. doi: http://dx.doi.org/10.1175/MWR-D-12-00070.1.

de Boyer Montégut, C., G. Madec, A. S. Fischer, A. Lazar, and D. Iudicone , 2004: Mixed layer depth over the global ocean: An examination of profile data and a profile-based climatology. J. Geophys. Res., 109, C12003.

Delworth T., Mann M. E., 2000: Observed and simulated multidecadal variability in the Northern Hemisphere. Climate Dyn., 16, 661–76.

Dhomps, A. L., S. Guinehut, P. Y. Le Traon, and G. Larnicol, 2011: A global comparison of Argo and satellite altimetry observations. Ocean Sci., 7, 175-183.

Dima, M., and G. Lohmann, 2007: A Hemispheric Mechanism for the Atlantic Multidecadal Oscillation. J. Climate, 20, 2706–2719.

Domingues, C. M., J. A. Church, N. J. White, P. J. Gleckler, S. E. Wijffels, P. M. Barker, andJ. R. Dunn (2008), Improved estimates of upper-ocean warming and multi-decadal sea-levelrise, Nature, 453, 1090-1093, doi:10.1038/nature07080.

Dong, S. Garzoli, S. & Baringer, M. The Role of Interocean Exchanges on Decadal Variations of the Meridional Heat Transport in the South Atlantic. J. Phys. Oceanogr. 41, 1498–1511 (2011).

Drijfhout, S. S., A. T. Blaker, S. A. Josey, A. J. G. Nurser, B. Sinha, and M. A. Balmaseda (2014), Surface warming hiatus caused by increased heat uptake across multiple ocean basins, Geophys. Res. Lett., 41, 7868–7874, doi:10.1002/2014GL061456.

Durgadoo, J., Loveday, B., Reason, C., Penven, P. & Biastoch, A. Agulhas Leakage Predominantly Responds to the Southern Hemisphere Westerlies. J. Phys. Oceanogr. 43, 2113-2131 (2013).

Easterling, D. R., and M. F. Wehner (2009), Is the climate warming or cooling? Geophys. Res. Lett., 36, L08706, doi:10.1029/2009GL037810.

Elsberry, R. L., Tara D. B. Lambert, and Mark A. Boothe (2007), Accuracy of Atlantic and Eastern North Pacific Tropical Cyclone Intensity Forecast Guidance. Wea. Forecasting, 22, 747–762. doi: http://dx.doi.org/10.1175/WAF1015.1.

Elsner, J. B., J. P. Kossin, and T. H. Jagger (2008), The increasing intensify of the strongest tropical cyclones. Nature, 326, 483-485. doi:10.1038/nature07234.

Emery, W. J. 1976. The Role of Vertical Motion in the Heat Budget of the Upper Northeastern Pacific Ocean. Journal of Physical Oceanography 6(3): 299-305.

Enfield, D. B., A. M. Mestas-Nuñez, and P. J. Trimble, 2001: The Atlantic Multidecadal Oscillation and its relation to rainfall and river flows in the continental U.S., Geophys. Res. Lett., 28, 10, 2077-2080.

England, M. et al. (2014), Recent intensification of wind-driven circulation in the Pacific and the ongoing warming hiatus. Nature Clim. Change 4, 222-227. doi:10.1038/nclimate2106.

Fischer, M., 2000, Multivariate projection of ocean surface data onto subsurface sections, Geophys. Res. Lett., 27, 755-757

Friocourt, Y., Drijfhout, S., Blanke, B. & Speich, S. Water Mass Export from Drake Passage to the Atlantic, Indian, and Pacific Oceans: A Lagrangian Model Analysis. J. Phys. Oceanogr. 35, 1206–1222 (2005).

Gillett, N., Fyfe, J. & Parker, D. Attribution of observed sea level pressure trends to greenhouse gas, aerosol, and ozone changes. Geophys. Res. Lett. 40, (2013).

Gillett, N., Zwiers, F., Weaver, A. & Stott, P. Detection of human influence on sea-level pressure. Nature 422, 292–294 (2003).

Goldenberg, S. B., C. W. Landsea, A. M. Mestas-Nuñez, and W. M. Gray (2001), The recent increase in Atlantic hurricane activity: Causes and implications. Science, 293, 474-479. DOI: 10.1126/science.1060040.

Gray, W. M. (1979), Hurricanes: their formation, structure and likely role in the tropical circulation, in Meteorology Over Tropical Oceans. D.B. Shaw (Ed.), Roy. Meteor. Soc., James Glaisher House, Grenville Place, Bracknell, Berkshire, RG12 1BX, 155-218.

Gray, W. M. (1984), Atlantic seasonal hurricane frequency: Part I: El Niño and 30-mb quasi-bienniel oscillation influences. Mon. Wea. Rev., 112, 1649-1668. doi: http://dx.doi.org/10.1175/1520-0493(1984)112<1649:ASHFPI>2.0.CO;2.

Gregory, J. M. et al. A model intercomparison of changes in the Atlantic thermohaline circulation in response to increasing atmospheric CO2 concentration. Geophys. Res. Lett. 32, L12703 (2005).

Guinehut, S., P. Y. Le Traon, G. Larnicol and S. Philipps, 2004. Combining Argo and remote-sensing data to estimate the ocean three-dimensional temperature fields—a first approach based on simulated observations. Journal of Marine Systems, 46 (1–4), pp. 85-98, doi:10.1016/j.jmarsys.2003.11.022

Han, W., Meehl, G.A. & Hu, A. Interpretation of tropical thermocline cooling in the Indian and Pacific oceans during recent decades. Geophys. Res. Lett. 33, L23615 (2006)

Hanna, E., Navarro, F. J., Pattyn, F., Domingues, C. M., Fettweis, X., Ivins, E. R., Nicholls,R. J., Ritz, C., Smith, B., Tulaczyk, S., Whitehouse, P. L., Zwally, H. J., (2013), Ice-sheet mass balance and climate change. Nature, 498,51-59, doi: 10.1038/nature12238.

HELD I M 2013. Climate science: The cause of the pause. Nature [J], 501: 318-319.

Høyer, , Jacob L,Detlef Quadfasel, , Ole B Andersen, , Deep ocean currents detected with satellite altimetry, Canadian Journal of Remote Sensing, 2002, 28, 4, 556

Huntley,D. A. ; J. M. Huthnance; M. B. Collins; C.-L. Liu; R. J. Nicholls; C. Hewitson; M. O. Green; K. R. Dyer; C. F. Jago Philosophical Transactions: Physical Sciences and Engineering, Vol. 343, No. 1669, Understanding the North Sea System. (Jun. 15, 1993), pp. 461-474.

Huntley, D. A,, Nicholls, R. J.,Liu, C.-L. & Dyer, K. R. 1993 Measurements of the semi-diurnal drag coefficient over sand waves. Continental Shelf Res.

IPCC Summary for Policymakers. In: Climate Change 2013: The Physical Science Basis (eds Stocker, T.F. et al.). 29 (Cambridge University Press, 2013)

IPCC, 2013: Climate Change 2013: The Physical Science Basis. Contribution of Working Group I to the Fifth Assessment Report of the Intergovernmental Panel on Climate Change [Stocker, T.F., D. Qin, G.-K. Plattner, M. Tignor, S.K. Allen, J. Boschung, A. Nauels, Y. Xia, V. Bex and P.M. Midgley (eds.)]. Cambridge University Press, Cambridge, United Kingdom and New York, NY, USA, 1535 pp.

Ishii, M., and M. Kimoto (2009), Reevaluation of historical ocean heat content variationswith time-varying XBT and MBT depth bias corrections, Journal of Oceanography, 65, 287-299, doi: 10.1007/s10872-009-0027-7.

Ivchenko, V. O., D. Sidorenko, S. Danilov, M. Losch, and J. Schröter, 2011: Can sea surface height be used to estimate oceanic transport variability?. Geophys. Res. Lett., 38, L11601.

Jiang H. and E. M. Ramirez (2013), Necessary Conditions for Tropical Cyclone Rapid Intensification as Derived from 11 Years of TRMM Data. J. Climate, 26, 6459–6470. doi: http://dx.doi.org/10.1175/JCLI-D-12-00432.1.

Jones, P. D., M. New, D.E. Parker, S. Martin, and I.G. Rigor (1999), Surface Air Temperature and its Changes Over the Past 150 Years, Rev. Geophys., 37(2), 173-199. DOI: 10.1029/1999RG900002.

Kaplan J. & M. DeMaria (2003), Large-Scale Characteristics of Rapidly Intensifying Tropical Cyclones in the North Atlantic Basin. Wea. Forecasting, 18, 1093–1108. doi: http://dx.doi.org/10.1175/1520-0434(2003)018<1093:LCORIT>2.0.CO;2.

Kaplan J., M. DeMaria, and J. A. Knaff (2010), A Revised Tropical Cyclone Rapid Intensification Index for the Atlantic and Eastern North Pacific Basins. Wea. Forecasting, 25, 220–241. doi: http://dx.doi.org/10.1175/2009WAF2222280.1.

Katsman C A, van Oldenborgh G J. 2011. Tracing the upper ocean's "missing heat". Geophys. Res. Lett., 38: L14610.

Kaufmann, R. K., H. Kauppi, M. L. Mann and J. H. Stock, 2011. Reconciling anthropogenic climate change with observed temperature 1998-2008. Proceedings of the National Academy of Sciences of the United States of America, 108 (29), pp. 11790-11793, doi: 10.1073/pnas.1102467108/-/DCSupplemental

Keeling, C. D., S. C. Piper, R. B. Bacastow, M. Wahlen, T. P. Whorf, M. Heimann, and H. A. Meijer, 2001. Exchanges of atmospheric CO_2 and $13CO_2$ with the terrestrial biosphere and oceans from 1978 to 2000. I. Global aspects, SIO Reference Series, No. 01-06, Scripps Institution of Oceanography, San Diego, 88 pages.

Keenlyside, N. S., M. Latif, J. Jungclaus, L. Kornblueh, and E. Roeckner, 2008: Advancing decadal-scale climate prediction in the North Atlantic sector. Nature, 453(7191), 84–88.

Khedouri, E., C. Szczechowski, and R.E. Cheney, 1983: Potential oceanographic applications of satellite altimetery for inferring subsurface thermal structure, Oceans, 15, 274-280.

Kidwell, A., Jo, Y.-H. & Yan, X.-H. A closer look at the central Pacific El Niño and warm pool migration events from 1982 to 2011, J. Geophys. Res. Oceans 119, 165-172 (2014).

Klemas, Victor, Xiao-Hai Yan, 2014. Subsurface and deeper ocean remote sensing from satellites: An overview and new results, Progress in Oceanography, Volume 122, March 2014, Pages 1-9, ISSN 0079-6611, http://dx.doi.org/10.1016/j.pocean.2013.11.010.

Knight, J. R., R. J. Allan, C. K. Folland, M. Vellinga, and M. E. Mann, 2005: A signature of persistent natural thermohaline circulation cycles in observed climate. Geophys. Res. Lett., 32, L20708.

Knutson, T. R. et al (2010a), Tropical cyclones and climate change. Nature Geoscience 3, 157–163. doi:10.1038/ngeo779.

Knutson, T.R., C. Landsea, K. Emauel (2010b), Tropical Cyclones and Climate Change: A Review. In, Chan, J. C. L. and J. Kepert (Editors), 2010: Global Perspectives on Tropical Cyclones – From Science to Mitigation. World Scientific Press. 243-284

Kohonen, T., 1982: Self-organized formation of topologically correct feature maps. Biol. Cybern., 43, 59-69.

Kohonen, T., 2001: Self-Organizing Maps. Springer-Verlag, Berlin, 3rd edition, 501pp.

Kosaka, Y., Xie, S. P., 2013. Recent global-warming hiatus tied to equatorial Pacific surface cooling. Nature [J], 501: 403-407.

Kraus, E. B., and J. S. Turner, 1967: A one-dimensional model of the seasonal thermocline. II.The general theory and its consequences. Tellus, 19, 98-105.

Krauss, W., and R. H. Käse (1998), Eddy formation in the Denmark Strait overflow, J. Geophys. Res., 103(C8), 15525–15538, doi:10.1029/98JC00785.

Lazier, R., Hendry, R., Clarke, A., Yashayaev, I., Rhines, P., 2002: Convection and restratification in the Labrador Sea, 1990–2000. Deep-Sea Res., Part I, 49, 10, 1819-1835

Le Bars, D., Dijkstra, H. A., & De Ruijter, W. P. M. Impact of the Indonesian Throughflow on Agulhas leakage. Ocean Sci., 9, 773–785, (2013).

Le Treut H, Cubasch U, Allen M. Historical Overview of Climate Change Science[J].

Leonard, D. A., B. Caputo, R. L. Johnson, and F. E. Hoge, 1977: Experimental remote sensing of subsurface temperature in natural ocean water. Geophys. Res. Lett., 4, 7, 279–281.

Levitus, S., et al. 2000. Warming of the World Ocean. Science 287(5461): 2225-2229.

Levitus, S., et al. 2005. Warming of the world ocean, 1955–2003. Geophysical Research Letters 32(2): L02604.

Levitus, S., et al., 2009. Global ocean heat content 1955-2008 in light of recently revealedinstrumentation problems, Geophysical Research Letters, 36, L07608, doi:10.1029/2008GL037155.

Levitus, S., et al., 2012. World ocean heat content and thermosteric sea level change (0 ̇C2000 m) 1955 ̇C2010, Geophysical Research Letters, 39, L10603, doi:10.1029/2012GL051106.

Liang, X. S. Unraveling the cause-effect relation between time series. Phys. Rev. E 90, 052150 (2014).

Lin, I. I., C. C. Wu, I. F. Pun, and D. S. Ko (2008), Upper-ocean thermal structure and the western North Pacific category 5 typhoons. Part I: Ocean features and the category 5 typhoons' intensification, Mon. Weather Rev., 136, 3288–3306. doi: http://dx.doi.org/10.1175/2008MWR2277.1.

Lin, I. I., I. F. Pun, and C. C. Lien (2014), "Category-6" supertyphoon Haiyan in global warming hiatus: Contribution from subsurface ocean warming, Geophys. Res. Lett., 41, 8547–8553 doi:10.1002/2014GL061281.

Lin, I. I., I. F. Pun, and C. C. Wu (2009), Upper ocean thermal structure and the western North Pacific category-5 typhoons. Part II: Dependence on translation speed, Mon. Weather Rev., 137, 3744–3757, doi: http://dx.doi.org/10.1175/2009MWR2713.1.

Liu, Chunzhen.1999.On Some Issues in Studying Climate Change Impact and Adaptation[J].Climatic and Environmental Research(in Chinese),4(2):129-134,doi:10.3878/j.issn.1006-9585.1999.02.01.

Liu, K. S. & C. L. Chan (2013), Inactive Period of Western North Pacific Tropical Cyclone Activity in 1998–2011, J. Climate, 26, 2614–2630, doi: http://dx.doi.org/10.1175/JCLI-D-12-00053.1

Liu, Y., and R. H. Weisberg, 2011: A Review of Self-Organizing Map Applications in Meteorology and Oceanography. Self Organizing Maps - Applications and Novel Algorithm Design, J. I. Mwasiagi, Ed., InTech, Available from: http://www.intechopen.com/articles/show/title/a-review-of-self-organizing-map-applications-in-meteorology-and-oceanography

Liu, Y., and R. H. Weisberg, 2011: A Review of Self-Organizing Map Applications in Meteorology and Oceanography. Self Organizing Maps - Applications and Novel Algorithm Design, J. I. Mwasiagi, Ed., InTech, Available from: http://www.intechopen.com/articles/show/title/a-review-of-self-organizing-map-applications-in-meteorology-and-oceanography

Liu, Y., R. H. Weisberg, and C. N. K. Mooers, 2006: Performance evaluation of the self-organizing map for feature extraction. J. Geophys. Res., 111, C05018.

Liu, Y., R. H. Weisberg, and C. N. K. Mooers, 2006: Performance evaluation of the self-organizing map for feature extraction. J. Geophys. Res., 111, C05018.

Luo, J.-J., Sasaki, W. & Masumoto, Y. Indian Ocean warming modulates Pacific climate change. Proc. Natl Acad. Sci. USA 109, 18701–18706 (2012).

Lutjeharms, J. R. E. & Van Ballegooyen, R. C. The Retroflection of the Agulhas Current. J. Phys. Oceanogr. 18, 1570–1583 (1988).

Lutjeharms, J. R. E. The Agulhas Current (Springer, 2006).

Marshall, J., F. Dobson, K. Moore, P. Rhines, M. Visbeck, E. d'Asaro, K. Bumke, S. Chang, R. Davis, K. Fischer, R. Garwood, P. Guest, R. Harcourt, C. Herbaut, T. Holt, J. Lazier, S. Legg, J. McWilliams, R. Pickart, M. Prater, I. Renfiew, F. Schott, U. Send, and W. Smethie, 1998: The Labrador Sea deep convection experiment. Bull. Amer. Meteor. Soc., 79, 10, 2033-2058.

McCarthy, G., E. et al. Observed interannual variability of the Atlantic meridional overturning circulation at 26.5 ̊N. Geophys. Res. Lett., 39, L19609 (2012).

McClain, C., Signorini, S., Christian, J., 2004: Subtropical gyre variability observed by ocean-color satellites. Deep-Sea Res., Part II, 51,1–3, 281-301

McDougall, T. J., 1987: Thermobaricity, cabbelling, and water-mass conversion. J. Geophys. Res., 92, C5, 5448-5464.

McGregor, S. et al. (2014), Recent Walker circulation strengthening and Pacific cooling amplified by Atlantic warming. Nature Climate Change 4, 888–892. doi:10.1038/nclimate2330.

McGregor, S. et al. Recent Walker circulation strengthening and Pacific cooling amplified by Atlantic warming. Nature Climate Change 4, 888–892 (2014).

Meehl, G. A., J. M. Arblaster, J. T. Fasullo, A. Hu and K. E. Trenberth, 2011. Model-based evidence of deep-ocean heat uptake during surface-temperature hiatus periods. Nature Change, 1 (7), pp. 360-364, doi: 10.1038/NCLIMATE1229

Meehl, G. A., J. M. Arblaster, J. T. Fasullo, A. Hu, and K. E. Trenberth, 2011: Model-based evidence of deep-ocean heat uptake during surface-temperature hiatus periods. Nat. Clim. Change, 1, 360-364.

Meehl, G., Arblaster, J., Fasullo, J., Hu, A. & Trenberth, K. Model-based evidence of deep-ocean heat uptake during surface-temperature hiatus periods. Nature Clim. Change 1, 360-364 (2011).

Meehl, G., J. Arblaster, J. Fasullo, A. Hu, & K. Trenberth, (2011), Model-based evidence of deep-ocean heat uptake during surface-temperature hiatus periods. Nature Clim. Change 1, 360-364, doi:10.1038/nclimate1229.

Meehl, Gerald A. , Julie M. Arblaster, John T. Fasullo, Aixue Hu, Kevin E. Trenberth. Model-based evidence of deep-ocean heat uptake during surface-temperature hiatus periods. Nature Climate Change, 2011; DOI: 10.1038/nclimate1229

Moisan, J. R. and P. P. Niiler 1998. The Seasonal Heat Budget of the North Pacific: Net Heat Flux and Heat Storage Rates (1950–1990). Journal of Physical Oceanography 28(3): 401-421.

Morice, C. P., J. J. Kennedy, N. A. Rayner, and P. D. Jones, (2012), Quantifying uncertainties in global and regional temperature change using an ensemble of observational estimates: The HadCRUT4 dataset, J. Geophys. Res., 117, D08101, doi:10.1029/2011JD017187.

Nguyen L. T. and John Molinari (2012), Rapid Intensification of a Sheared, Fast-Moving Hurricane over the Gulf Stream. Mon. Wea. Rev., 140, 3361–3378. doi: http://dx.doi.org/10.1175/MWR-D-11-00293.1.

Oke, Peter R. , G B B, David A. Griffin, Andreas Schiller (2008) . The Bluelink ocean data assimilation system (BODAS) [J]. Ocean Modelling, 2008. 21: 46-70.

Palmer M D, McNeall D J, Dunstone N J, et al. 2011. Importance of the deep ocean for estimating decadal changes in Earth's radiation balance .Geophys. Res. Lett., 38 (13): L13707, doi:10.1029/2011GL047835.

Pierce, D. W. et al. Anthropogenic warming of the oceans: Observations and model results. J. Clim., 19, 1873–1900 (2006).

Price, J. F. (1981), Upper Ocean Response to a Hurricane. J. Phys. Oceanogr., 11, 153–175. doi: http://dx.doi.org/10.1175/1520-0485(1981)011<0153:UORTAH>2.0.CO;2.

Price, J. F., T. B. Sanford, and G. Z. Forristall (1994), Forced Stage Response to a Moving Hurricane. J. Phys. Oceanogr., 24, 233–260. doi: http://dx.doi.org/10.1175/1520-0485(1994)024<0233:FSRTAM>2.0.CO;2.

Price, J. F. (2009), Metrics of hurricane-ocean interaction: vertically-integrated or vertically-averaged ocean temperature?, Ocean Sci., 5, 351-368, doi:10.5194/os-5-351-2009.

Prince, J. F., T. K. McKee, J. R. Valdes, P. L. Richardson, and L. Armi, 1986: SOFAR float Mediterranean outflow experiment, 1984–1985. Woods Hole Oceanographic Institution Tech.Rep.WHOI-86-31, 199 pp.

Pun, I.-F., I.-I. Lin, and M.-H. Lo (2013), Recent increase in high tropical cyclone heat potential area in the Western North Pacific Ocean, Geophys. Res. Lett., 40, 4680–4684, doi:10.1002/grl.50548.

Rahmstorf, S., 1998: Influence of Mediterranean Outflow on climate. Eos Trans., 79, 24, 281.

Reid, J. L., 1979: On the contribution of the Mediterranean Sea outflow to the Norwegian-Greenland Sea. Deep-Sea Res., 26A, 1199–1223.

Robinson, A., and P. Lermusiaux (2000), Overview of data assimilation, [online] Available from: http://vigor.wustl.edu/Capita/CapitaReports/071124_DataAssimilation/

Roemmich, D., and J. Gilson (2011), The global ocean imprint of ENSO,Geophysical Research Letters, 38, doi:10.1029/2011GL047992. [online] Available from: http://dx.doi.org/10.1029/2011GL047992

Rouault, M., Penven, P. & Pohl, B. Warming in the Agulhas Current system since the 1980's. Geophys. Res. Lett. 36, L12602 (2009).

Roxy, M., Ritika, K., Terray, P. & Masson, S. The Curious Case of Indian Ocean Warming. J. Clim. 27, 8501-8509 (2014).

Rühs, S., Durgadoo, J., Behrens, E. & Biastoch, A. Advective timescales and pathways of Agulhas leakage. Geophys. Res. Lett. 40, 3997–4000 (2013).

Saunders, M. A. and A. S. Lea (2008), Large contribution of sea surface warming to recent increase in Atlantic hurricane activity, Nature, 451, 557-560, doi:10.1038/nature06422.

Schott, F. A., Xie S. -P., McCreary J. P. Indian Ocean circulation and climate variability. Rev. Geophys. 47, RG1002 (2009).

Schreck III, C. J., K. R. Knapp, and J. P. Kossin (2014), The Impact of best track discrepancies on global tropical cyclone climatologies using IBTrACS. Monthly Weather Review, 142(10), 3881-3899, doi: http://dx.doi.org/10.1175/MWR-D-14-00021.1.

Schultz, C. 2013, Past decade saw unprecedented warming in the deep ocean. Eos, Transactions American Geophysical Union [J], 94: 288-288.

Shay, L K., G. J. Goni, and P. G. Black (2000), Effects of a Warm Oceanic Feature on Hurricane Opal. Mon. Wea. Rev., 128, 1366–1383. doi: http://dx.doi.org/10.1175/1520-0493(2000)128<1366:EOAWOF>2.0.CO;2.

Shindell, D. & Schmidt, G. Southern Hemisphere climate response to ozone changes and greenhouse gas increases. Geophys. Res. Lett. 31, (2004).

SLOYAN B M, WIJFFELS S E, TILBROOK B, et al. 2013. Deep Ocean Changes near the Western Boundary of the South Pacific Ocean. Journal of Physical Oceanography [J], 43: 2132-2141.

Smith, D. M., S. Cusack, A. W. Colman, C. K. Folland, G. R. Harris, and J. M. Murphy, 2007: Improved surface temperature prediction for the coming decade from a global climate model. Science, 317(5839), 796–799.

Smith, T. M., et al. (2008), Improvements to NOAA's Historical Merged Land-Ocean Surface Temperature Analysis (1880-2006), J. Climate, 21, 2283-2293, doi: http://dx.doi.org/10.1175/2007JCLI2100.1.

Solomon, S. et al, 2010. Contributions of stratospheric water vapor to decadal changes in the rate of global warming. Science 327, 1219–1223.

Song, J.-J., Y. Wang, and L. Wu (2010), Trend discrepancies among three best track data sets of western North Pacific tropical cyclones, J. Geophys. Res., 115, D12128, doi:10.1029/2009JD013058.

Song, Q., Gordon, A. L. & Visbeck, M. Spreading of the Indonesian Throughflow in the Indian Ocean. J. Phys. Oceanogr. 34, 772–792 (2004).

Song, Y. T., and F. Colberg (2011), Deep ocean warming assessed from altimeters, Gravity Recovery and Climate Experiment, in situ measurements, and a non-Boussinesq ocean general circulation model, J. Geophys. Res., 116, C02020, doi:10.1029/2010JC006601.

Speich, S., Blanke, B. & Cai, W. Atlantic meridional overturning circulation and the Southern Hemisphere supergyre. Geophys. Res. Lett. 34, L23614 (2007).

Sprintall J, et al. The Indonesian seas and their role in the coupled ocean–climate system. Nature Geosci. 7, 487-492 (2014)

Stammer, D. Response of the global ocean to Greenland and Antarctic ice melting. J. Geophys. Res. 113, C06022 (2008).

Steinman, B A., M E. Mann, and S K. Miller (2015), Atlantic and Pacific multidecadal oscillations and Northern Hemisphere temperatures, Science, 347 (6225), 988-991, DOI:10.1126/science.1257856.

Su, H., X. Wu, X.-H. Yan, A. Kidwell (2015), Estimation of subsurface temperature anomaly in the Indian Ocean during recent global surface warming hiatus from satellite measurements: A support vector machine approach. Remote Sensing of Environment, 160: 63-71. DOI: 10.1016/j.rse.2015.01.001.

Takano, A., H. Yamazaki, T. Nagai, O. Honda, 2009: A Method to Estimate Three-Dimensional Thermal Structure from Satellite Altimetry Data. J. Atmos. Oceanic Technol., 26, 2655–2664.

Takano, A., H. Yamazaki, T. Nagai, O. Honda, 2009: A Method to Estimate Three-Dimensional Thermal Structure from Satellite Altimetry Data. J. Atmos. Oceanic Technol., 26, 2655–2664.

Tang, Q., and Chan, Z., Thermohaline structures across the Luzon Strait from seismic reflection data, Dynamics of Atmospheres and Oceans, Volume 51, Issue 3, April 2011, Pages 94-108, ISSN 0377-0265, 10.1016/j.dynatmoce.2011.02.001.

Telszewski, M., A. Chazottes, U. Schuster, A. J. Watson, C. Moulin, D. C. E. Bakker, M. González-Dávila, T. Johannessen, A. Körtzinger, H. Lüger, A. Olsen, A. Omar, X. A. Padin, A. F. Rós, T. Steinhoff, M. Santana-Casiano, D. W. R. Wallace, and R. Wanninkhof, 2009: Estimating the monthly pCO2 distribution in the North Atlantic using a self-organizing neural network. Biogeosci., 6, 1405-1421.

Thacker, W. C., Lee S K, and Halliwell G R (2004). Assimilating 20 years of Atlantic XBT data into HYCOM: a first look [J]. Ocean Modelling, 2004, 7: 183-210.

Toggweiler, J. & Russell, J. Ocean circulation in a warming climate. Nature, 451, 286–288 (2008).

Tory，K. & W.M. Frank, 2010. Tropical Cyclone Formation. In, Chan, J. C. L. and J. Kepert (Editors), 2010: Global Perspectives on Tropical Cyclones – From Science to Mitigation. World Scientific Press. 55-84.

Trenary, L. & Han, W. Causes of decadal subsurface cooling in the tropical Indian Ocean during 1961–2000. Geophys. Res. Lett. 35, (2008).

Trenberth, K. E. and Fasullo, J. T. (2013), An apparent hiatus in global warming?. Earth's Future, 1: 19–32. doi: 10.1002/2013EF000165

Vesanto, J., J. Himberg, E. Alhoniemi, and J. Parhankangas, 2000: SOM Toolbox for Matlab 5. Technical Report A57, Helsinki University of Technology, Neural Networks Research Centre, 60 pp.

von Schuckmann, K., and P.-Y. Le Traon (2011), How well can we derive global oceanindicators from Argo data?, Ocean Science, 7, 783–791, doi:10.5194/osd-8-999-2011.

Wake, B. 2013. Oceanography: Warming seas. Nature Clim. Change [J], 3: 442-442.

Wang, B. and J. C. L. Chan (2002), How Strong ENSO Events Affect Tropical Storm Activity over the Western North Pacific. J. Climate, 15, 1643–1658. doi: http://dx.doi.org/10.1175/1520-0442(2002)015<1643:HSEEAT>2.0.CO;2

Wang, B., & X. Zhou (2008), Climate variation and prediction of rapid intensification in tropical cyclones in the western North Pacific. Meteorol. Atmos. Phys., 99, 1-16, DOI: 10.1007/s00703-006-0238-z.

Watanabe, M., Y. Kamae, M. Yoshimori, A. Oka, M. Sato, M. Ishii, T. Mochizuki and M. Kimoto, 2013. Strengthening of ocean heat uptake efficiency associated with the recent climate hiatus. Geophysical Research Letters, 40 (12), pp. 3175-3179, doi: 10.1002/grl.50541

Webster, P. J., G. J. Holland, J. A. Curry, H.-R. Chang (2005), Changes in tropical cyclone number, duration, and intensity in a warming environment. Science, 309, 1844-1846, DOI: 10.1126/science.1116448.

Williams, J. J., MacDonald, N. J., O'Connor,B. A., Pan, S., 2000. Offshore sand bank dynamics. Journal of Marine Systems, Volume 24, Issues 1-2:153-173

Williams, Jon J.,1995. Drag and Sediment Dispersion Over Sand Waves, Estuarine, Coastal and Shelf Science, Volume 41: 659-687

Willis, J. K., D. Roemmich, and B. Cornuelle, 2003: Combining altimetric height with broadscale profile data to estimate steric height, heat storage, subsurface temperature, and sea-surface temperature variability. J. Geophys. Res., 108, C9, 3292.

Wu, L. et al. Enhanced warming over the global subtropical western boundary currents. Nature Clim. Change 2, 161-166 (2012).

Wu, Z., et al. (2007). "On the trend, detrending, and variability of nonlinear and nonstationary time series." Proceedings of the National Academy of Sciences 104(38): 14889-14894.

Wu, Z. H, N. E. Huang, (2009) Ensemble empirical mode decomposition: a noise-assisted data analysis method. Adv. Adapt. Data Anal. 1, 1–41, DOI: 10.1142/S1793536909000047.

Wu, Z. H., N. E. Huang, J. M. Wallace, B. V. Smoliak, X. Y. Chen (2011), On the time-varying trend in global-mean surface temperature. Climate Dynamics. 37(3-4), 759-773, 10.1007/s00382-011-1128-8.

Xie, F., Li, J., Tian, W., Li, Y. & Feng, J. Indo-Pacific Warm Pool Area Expansion, Modoki Activity, and Tropical Cold-Point Tropopause Temperature Variations. Sci. Rep. 4, 4552; DOI:10.1038/srep04552 (2014).

Yan, X.-H, Ho, C. R., Zheng, Q & Klemas, V. Using satellite IR in studies of the variabilities of the western Pacific warm pool. Science. 262,440-441(1993).

Yan, X.-H., A. Okubo, J.R. Shubel, and D.W. Pritchard, 1991a: An analytical model for remote sensing determination of the mixed layer depth. Deep Sea Res., 38, 3, 267-287.

Yan, X.-H., and A. Okubo, 1992: Three-dimensional analytical model for the mixed layer depth. J. Geophys. Res, 97, C12, 20201-20226.

Yan, X.-H., Ho, C. R., Zheng, Q. & Klemas, V. Temperature and size variabilities of the Western pacific warm pool. Science, 258, 1643-5 (1992).

Yan, X.-H., J.R. Schubel, and D.W. Pritchard, 1990: Oceanic upper mixed layer depth determination by the use of satellite data. Remote Sens. Environ., 32, 55-74.

Yan, X.-H., P.P. Niiler and R.H. Stewart, 1991b: Construction and accuracy analysis of images of the daily-mean mixed layer depth. Int. J. Remote Sens., 12, 2573-2584.

Yan, X. H., et al. 1995. Seasonal heat storage in the North Pacific: 1976–1989. Journal of Geophysical Research: Oceans 100(C4): 6899-6926.

Yan, X.-H., Y. Jo, W. T. Liu, and M. He, 2006: A new study of the Mediterranean outflow, air-sea interactions, and Meddies using multisensor data. J. Physical Oceanogr., 36, 4, 691-710.

Yan, X-H., Jo, Y-H., Liu,W.T., and He, M-X., 2006. A new study of the Mediterranean outflow, air-sea interactions, and meddies using multisensory data. J. Phy. Oceanography, 36,691-710.

Yang, X., Anthony Rosati,* Shaoqing Zhang,* Thomas L. Delworth,* Rich G. Gudgel,* Rong Zhang,* Gabriel Vecchi,* Whit Anderson,* You-Soon Chang,* Timothy DelSole,#Keith Dixon,* Rym Msadek,* William F. Stern,* Andrew Wittenberg,* and Fanrong Zeng, 2013: A predictable AMO-like pattern in GFDL's coupled initialization and decadal forecasting system. Journal of Climate, 26, 650–661.

Ying, M., W. Zhang, H. Yu, X. Lu, J. Feng, Y. Fan, Y. Zhu, and D. Chen (2014), An overview of the China Meteorological Administration tropical cyclone database, J. Atmos. Oceanic Technol., 31, 287-301, doi: 10.1175/JTECH-D-12-00119.1

Yu, H, & H. J. Kwon (2005), Effect of TC-trough interaction on the intensity changes of two typhoons. Wea. Forecasting, 20, 199-211. doi: http://dx.doi.org/10.1175/WAF836.1.

Yu, K., et al. (2012), High-precision U-series ages of transported coral blocks on Heron Reef (southern Great Barrier Reef) and storm activity during the past century. Palaeogeogr. Palaeoclimatol. Palaeoecol. 337-338, 23-36, doi:10.1016/j.palaeo.2012.03.023.

Yu, K.-F. J.-X. Zhao, Q. Shi, Q.-S. Meng (2009), Reconstruction of storm/tsunami records over the last 4000 years using transported coral blocks and lagoon sediments in the southern South China Sea, Quaternary International, 195, 128-137, http://dx.doi.org/10.1016/j.quaint.2008.05.004.

Zhang, R. and T. L. Delworth, 2006: Impact of atlantic multidecadal oscillations on India/Sahel rainfall and Atlantic hurricanes. Geophys. Res. Lett., 33, L17712.

Zinke, J., Loveday, B.R., Reason, C.J.C., Dullo, W.-C. & Kroon, D. Madagascar corals track sea surface temperature variability in the Agulhas Current core region over the past 334 years. Sci. Rep. 4, 4393; DOI:10.1038/srep04393 (2014).

Appendix A

PUBLICATIONS

The following publications resulted from or related to the work presented in this thesis. They are classified below according to the chapters they adhere to the most.

Chapter 2

Wu, Xiangbai, Xiao-Hai Yan, Young-Heon Jo, W. Timothy Liu, 2012: Estimation of Subsurface Temperature Anomaly in the North Atlantic Using a Self-Organizing Map Neural Network. J. Atmos. Oceanic Technol., 29, 1675–1688. doi: http://dx.doi.org/10.1175/JTECH-D-12-00013.1

Su, Hua, **Wu, Xiangbai**, Yan, Xiao-Hai, Kidwell, Autumn, 2015. Estimation of subsurface temperature anomaly in the Indian Ocean from satellite remote sensing measurements: A support vector machine approach. Remote sensing of Environment, 160: 63-71, doi:10.1016/j.rse.2015.01.001.

Chapter 3

Wu, Xiangbai, Yan Li, Salvienty Makarim, Weiwei Zhang, Xiao-Hai Yan, 2015. Decadal Variation of Upper Layer Ocean Heat Content in the Indian Ocean. JGR-Oceans, under review.

Su, Hua, Wenfang Lu, **Xiangbai Wu**, Weiwei Zhang, Xiao-Hai Yan, 2015. Contribution of global subsurface and deeper ocean warming to recent global surface warming hiatus, Scientific Report, major revision.

Makarim, Salvienty, Xiao-Hai Yan, **Xiangbai Wu**, WeiDong Yu, Iskhaq Iskandar, 2015. Warming and Hiatus in Indian Ocean imprint with Climatic Modes and Subducted Waters, in prep.

Chapter 4

Wu, Xiangbai, Yan Li, Xiao-Hai Yan, et al. 2015. Rapid Intensification of Intense Tropical Cyclone in Western North Tropical Pacific related to Global Warming and Hiatus. in prep.

Wu, **Xiangbai,** Autumn Kidwell, Yan Li, Hua Su, Guoqiang Qiu, Xiao-Hai Yan*, 2015. Variation of Rapid Intensification of Major Tropical Cyclones in Western North Pacific: A New Index and Its Primary Application. *Geophysical Research Letters*, under review.

(Status: 26 August 2015)

Appendix B

NOTATION

e	internal energy
$Q,\ Q_\downarrow,\ Q_{SW},\ Q_{LW}$ $Q_L,\ Q_S$	Heat flux, influx at the sea surface, solar shortwave irradiance, net longwave radiation, latent heat flux and sensible heat flux
W	mechanical work
C_v	heat capacity
$T,\ \bar{T},\ T'$	temperature, climatology and anomaly
$H,\ H_{Alt}$	ocean heat content, OHC estimated from altimeter data
k_T	thermal conductivity of the fluid
$\rho,\ \sigma$	Density, volume per mass
u, v, w	Current velocity 3 dimensional component
$\kappa_T = \dfrac{k_T}{\rho C_v}$	heat kinematic diffusivity
$\vec{V},\ \vec{v}$	three dimensional velocity, horizontal velocity
$\blacksquare_a$	Subscription a denotes vertically averaged terms
$\blacksquare_h$	Subscription h denotes terms at the isotherm $h = f(x,y,t)$
$\blacksquare_D$	Subscription D denotes terms at fixed depth of D
$\hat{\blacksquare}$	Hat denotes deviation from the vertically averaged term
$\blacksquare_+$	Subscription $plus$ denotes terms at bottom of mixed layer
$\bar{\blacksquare}$	overbar denotes climatology terms
$\blacksquare'$	Prime denotes anomaly terms
w_e	Ekman pumping velocity
α_T	thermal expansion coefficient
η'_{Alt}	the sea surface height anomaly (SSHA) from satellite altimetry
$\eta'_{thermal},\ \eta'_{salinity}$	sea level change due to thermal expansion, salinity change

$\eta'_{wind}, \eta'_{wave}$ sea level change due to wind, wave effect